

# Prediction of In-Plane and Out-of-Plane Defects in Steered Prepreg Tape during Automated Fiber Placement: Experimental and Analytical Modeling

Meisam Kheradpisheh

A Thesis

in

The Department

of

Mechanical Industrial and Aerospace Engineering

Presented in Partial Fulfillment of the Requirements

for the Degree of

Doctor of Philosophy (Mechanical Engineering) at

Concordia University

Montréal, Québec, Canada

March 2025

© Meisam Kheradpisheh, 2025

CONCORDIA UNIVERSITY

School of Graduate Studies

This is to certify that the thesis prepared

By: **Mr. Meisam Kheradpisheh**

Entitled: **Prediction of In-Plane and Out-of-Plane Defects in Steered  
Prepreg Tape during Automated Fiber Placement: Experi-  
mental and Analytical Modeling**

and submitted in partial fulfillment of the requirements for the degree of

**Doctor of Philosophy (Mechanical Engineering)**

complies with the regulations of this University and meets the accepted standards with respect to originality and quality.

Signed by the Final Examining Committee:

\_\_\_\_\_ Chair  
*Dr. Luiz Lopes*

\_\_\_\_\_ External Examiner  
*Dr. Gangadhara Prusty*

\_\_\_\_\_ External to program  
*Dr. Emre Erkmen*

\_\_\_\_\_ Examiner  
*Dr. Suong Van Hoa*

\_\_\_\_\_ Examiner  
*Dr. Farjad Shadmehri*

\_\_\_\_\_ Supervisor  
*Dr. Mehdi Hojjati*

Approved by \_\_\_\_\_  
Muthukumaran Packirisamy, Chair Department of Mechani-  
cal Industrial and Aerospace Engineering

\_\_\_\_\_ 2025 \_\_\_\_\_  
Mourad Debbabi, Dean Faculty of Engineer-  
ing and Computer Science

# Abstract

## **Prediction of In-Plane and Out-of-Plane Defects in Steered Prepreg Tape during Automated Fiber Placement: Experimental and Analytical Modeling**

**Meisam Kheradpisheh, Ph.D.**

**Concordia University, 2025**

Automated Fiber Placement (AFP) is a promising technology for manufacturing high-quality, large-scale structural components with complex geometries. However, a major challenge with AFP is the formation of manufacturing-induced defects, such as wrinkles, waviness, and tape folding, that occur during the steering process. These defects arise from the mismatch in length between the inner and outer edges of the prepreg tape when it is placed along a curved path. Such defects can degrade the mechanical properties of the part, leading to a reduction in its quality. Therefore, minimizing or eliminating these defects is crucial to improve the final product's overall quality. This thesis aims to analytically predict the in-plane and out-of-plane defects occurring at a steered tape in the AFP process, and the ultimate goal is to propose some solutions for reducing and eliminating the steering-induced defects.

A thorough experimental investigation was conducted using a variety of process parameters and steering radii to enhance our understanding of the defect formation during the steering of thermoset prepreg tows. Based on the experimental observations, two micro and macro models were presented to predict planar and non-planar deformations at steered tapes. According to the analytical results, it was then shown that interlayer bonding plays a significant role in the generation of defects in the AFP process. Consequently, a systematic series of experiments and finite element analysis was performed to enhance the interlaminar bondings at the AFP process. At the end according to all experimental and analytical

analysis, a novel compaction roller is designed and manufactured to provide variable pressure distributions and contact length based on the geometry of the part, unlike traditional rollers, to reduce and minimize the defect formation during steering.

# Acknowledgments

I am profoundly grateful to my esteemed supervisor, Dr. Mehdi Hojjati for his continuous guidance, unwavering support, and his advice throughout this entire journey. His encouragement and patience have been the foundation of all the progress I have made, and the completion of this PhD work would not have been possible without his mentorship. I owe a great debt of gratitude to Professor Suong Van Hoa, who established the Concordia Centre for Composites (CONCOM) for his tireless efforts and guidance.

I would like to express my gratitude to Bombardier Aerospace for providing the advanced materials, and to the Natural Sciences and Engineering Research Council of Canada (NSERC) for offering the research facilities. Without their support, completing my studies would not have been possible. I am especially grateful for the technical expertise and assistance of Dr. Daniel Rosca and Dr. Heng Wang. I also want to acknowledge the support of my colleagues and friends— Sepanta, Ehsan, Zohreh, Marjan, Farshad, and AmirHafez—who have been by my side throughout this journey.

Finally, I want to express my heartfelt gratitude to my parents and sisters. It's been four years since I moved abroad, and your unwavering belief in me has been the driving force behind every step forward. Words can't capture how much I love you and how fortunate I am to be your son and brother. My motivation to keep striving comes from the desire to make our family proud. Everything I have accomplished is because of your unconditional love and support.

# List of publications

## Journal papers

- (1) Kheradpisheh, Meisam, and Mehdi Hojjati. "Wrinkle formation and initial defect sensitivity of steered tow in automated fiber placement." *Journal of Composites Science* 5.11 (2021): 295.
- (2) Kheradpisheh, Meisam, and Mehdi Hojjati. "In-plane and out-of-plane deformations in automated fiber placement employing micromechanics method." *Composites Part A: Applied Science and Manufacturing* 170 (2023): 107543.
- (3) Kheradpisheh, Meisam, and Mehdi Hojjati. "Exact three-dimensional elasticity analysis for buckling of composite laminated plates resting on viscoelastic foundation." *Thin-Walled Structures* (2024): 112060.
- (4) Kheradpisheh, Meisam, Amir Hafez Yas, and Mehdi Hojjati. "The effect of automated fiber placement process parameters on interlaminar shear strength of uncured prepreg bonded samples." *Journal of Composite Materials* (2025): 00219983241313280.
- (5) Kheradpisheh, Meisam, and Mehdi Hojjati. "A novel compaction roller with variable pressure distribution and contact time for automated fiber placement: Experimental and numerical analysis." *Composites Part A: Applied Science and Manufacturing* 190 (2025): 108684.

## Conference Papers

- (1) Kheradpisheh, Meisam, and Mehdi Hojjati. "The effect of Automated fiber placement (AFP) process parameters on shear behavior of uncured bonded prepreg tapes" *The Sixth International Symposium on Automated Composites Manufacturing (ACM6)*. South Carolina, SC, USA. 4-8 March 2024.
- (2) Kheradpisheh, Meisam, and Mehdi Hojjati. "Non-planar defects formation using different compaction rollers during automated fiber placement." *SAMPE 2023*, Seattle, WA, April 17-20.

# Contents

<b>List of Figures</b>	<b>xi</b>
<b>List of Tables</b>	<b>xvii</b>
<b>1 Introduction and Motivations</b>	<b>1</b>
1.1 AFP technology and defect formation mechanism during the process . . . . .	2
1.2 Research Motivation . . . . .	3
1.3 Research Objectives . . . . .	4
1.4 Thesis Layout . . . . .	5
<b>2 Literature Review</b>	<b>7</b>
2.1 The thermoset AFP process . . . . .	7
2.1.1 AFP equipment used in this thesis . . . . .	8
2.2 Thermoset prepreg material . . . . .	9
2.3 Steering process and defects mechanics during steering . . . . .	10
2.3.1 The effect of AFP defects on mechanical properties . . . . .	11
2.4 Experimental and analytical approaches to investigate steering . . . . .	12
2.5 Conclusion Remarks . . . . .	16
<b>3 Wrinkle formation and initial defect sensitivity of steered tow in auto-</b>	
<b>    mated fiber placement</b>	<b>18</b>
3.1 Abstract . . . . .	18
3.2 Introduction . . . . .	19

3.3	Experiments . . . . .	22
3.4	Formulation . . . . .	26
3.4.1	Buckling model . . . . .	26
3.4.2	Initial Defect . . . . .	28
3.4.3	Solution Procedure . . . . .	29
3.4.4	Relation between Critical Steering Radius and Critical Load . . . . .	34
3.5	Result and Discussion . . . . .	36
3.5.1	Numerical Results Obtained from Wrinkle Model . . . . .	36
3.5.2	Drawing a Comparison between Wrinkle Wavelengths Obtained from the Theoretical Model and Experimental Work . . . . .	39
3.6	Conclusions . . . . .	40
<b>4</b>	<b>Exact three-dimensional elasticity analysis for buckling of composite lam- inated plates resting on viscoelastic foundation</b>	<b>41</b>
4.1	Abstract . . . . .	41
4.2	Introduction . . . . .	42
4.3	Analytical procedure . . . . .	45
4.3.1	Maxwell model for describing the viscoelastic foundation . . . . .	50
4.3.2	Coupled influence of viscoelastic foundation and exact solution . . . . .	51
4.4	Analytical results and discussion . . . . .	54
4.4.1	Validation of the proposed method . . . . .	54
4.4.2	The effect of the spring constants of the foundation and aspect ratio on the buckling load . . . . .	55
4.4.3	The effect of time parameter at normal and shear viscoelastic modulus $K(t)$ on the transient buckling response . . . . .	56
4.5	Numerical simulation and results . . . . .	58
4.5.1	Description of finite element model (FEM) . . . . .	59
4.5.2	Numerical results . . . . .	59
4.5.3	Thickness and Lay-up sequence effect . . . . .	59

4.6	Conclusion . . . . .	62
<b>5</b>	<b>In-plane and out-of-plane deformations in automated fiber placement employing micromechanics method</b>	<b>65</b>
5.1	Abstract . . . . .	65
5.2	Introduction . . . . .	66
5.2.1	Related work . . . . .	67
5.2.2	Contributions . . . . .	71
5.3	Experimental work (Part 1) . . . . .	72
5.3.1	AFP machine . . . . .	72
5.3.2	Observation of defects during the AFP process . . . . .	72
5.4	Analytical procedure . . . . .	75
5.4.1	Viscoelastic model of the stickiness of the prepreg . . . . .	76
5.4.2	The micro fiber-buckling model . . . . .	77
5.5	Experimental work (Part 2) . . . . .	80
5.5.1	<i>Identification of material characterization</i> . . . . .	80
5.6	Numerical results and discussion . . . . .	84
5.6.1	Transient response of fiber buckling in y and z directions . . . . .	85
5.6.2	Prediction of wavelength changes in-width direction in a steered tow	88
5.6.3	The effect of relaxation modulus of the prepreg and length of the fiber on critical load . . . . .	90
5.6.4	The effect of mixed mode in in-plane waviness . . . . .	91
5.7	Conclusion . . . . .	92
<b>6</b>	<b>The effect of automated fiber placement process parameters on interlaminar shear strength of uncured prepreg bonded samples</b>	<b>94</b>
6.1	Abstract . . . . .	94
6.2	Introduction . . . . .	95
6.3	Materials and manufacturing procedure . . . . .	100
6.3.1	Sample preparation . . . . .	100

6.4	Experimental results and discussion . . . . .	102
6.4.1	Pressure effect . . . . .	103
6.4.2	Feed rate and dwell time effects . . . . .	104
6.4.3	Temperature effect . . . . .	106
6.5	Geometric and microscopic analysis . . . . .	108
6.6	Numerical simulation and results . . . . .	109
6.6.1	Description of the FE model . . . . .	109
6.6.2	Simulation results . . . . .	113
6.7	Conclusion . . . . .	116
<b>7</b>	<b>A Novel Compaction Roller with Variable Pressure Distribution and Contact Time for Automated Fiber Placement: Experimental and Numerical Analysis</b>	<b>119</b>
7.1	Abstract . . . . .	120
7.2	Introduction . . . . .	120
7.3	Out-of-plane defects in AFP process . . . . .	125
7.4	Design and manufacturing procedure of new roller . . . . .	127
7.4.1	Finite element analysis for identifying unknown parameters . . . . .	129
7.4.2	Manufacturing of the new compaction roller . . . . .	134
7.5	Results and discussion . . . . .	135
7.5.1	Verification of the pressure distribution of the manufactured compaction rollers . . . . .	135
7.5.2	AFP Experimental validation of new compaction roller Performance	137
7.6	Conclusion . . . . .	139
<b>8</b>	<b>Conclusion and future work</b>	<b>141</b>
8.1	Future work . . . . .	142
	<b>Appendix A</b>	<b>144</b>
	<b>Bibliography</b>	<b>145</b>

# List of Figures

Figure 1.1 Automated fiber placement head and the key components Hörmann (2015) . . . . .	3
Figure 2.1 Thermoset automated fiber placement head and the key components	9
Figure 2.2 Prepreg slit-tape spool . . . . .	10
Figure 2.3 Steered tape manufactured by thermoset automated fiber placement .	10
Figure 2.4 Overview of different types of defects at a steered prepreg tape Hörmann (2015) . . . . .	11
Figure 2.5 The model presented for wrinkle formation by Beakou, Cano, Le Cam, and Verney (2011) . . . . .	14
Figure 3.1 Automated fiber placement machine: (a) fiber placement with a six-axis robot arm, (b) the head and the roller-tape contact, (c) the guidance system. . . . .	23
Figure 3.2 The tow's path made by AFP machine's software. . . . .	24
Figure 3.3 Steered prepreg on aluminum tool and wrinkle formation generated in tows. . . . .	24
Figure 3.4 Schematic of a section of tape resting on elastic foundation under combined axial compression and bending. . . . .	25
Figure 3.5 Elastic foundation: (a) free body diagram adhesive joint, (b) Pasternak elastic foundation model. . . . .	26
Figure 3.6 The stress distribution for different values of $\eta$ . . . . .	28
Figure 3.7 Staggered grid and nodes in the y-direction. . . . .	32

Figure 3.8	A schematic diagram of a steered tow under the bending load generated by the roller. . . . .	35
Figure 3.9	The variations of critical load versus different plate aspect ratios for various initial defect coefficients. . . . .	37
Figure 3.10	The variations of critical radius versus different plate aspect ratios and initial defect coefficients. . . . .	37
Figure 3.11	Critical radius steering variations with respect to tack stiffness parameter for different initial defect coefficients. . . . .	38
Figure 3.12	Critical buckling load variations with respect to tack stiffness parameter for different initial defect coefficients. . . . .	39
Figure 3.13	Wrinkle wavelength of the tape versus different steering radius. . . . .	40
Figure 4.1	Schematic of a laminated plate resting on Maxwell viscoelastic foundation. . . . .	46
Figure 4.2	The generalized Maxwell model. . . . .	50
Figure 4.3	Schematic of stress components in an element of the viscoelastic shear layer. . . . .	51
Figure 4.4	The values of buckling load as a function of the aspect ratio and Spring constant of the foundation. . . . .	56
Figure 4.5	A schematic of automated fiber placement. . . . .	57
Figure 4.6	The response of the buckling load versus aspect ratio changes with considering the time effect on the viscoelastic foundation. . . . .	58
Figure 5.1	Automated Fiber Placement process. . . . .	73
Figure 5.2	Steered tows: a) Steered tows on aluminum substrate b) Out-of-plane buckling (wrinkle) and in-plane buckling (waviness) at steered tow c) The top view Out-of-plane buckling d) The top view of In-plane buckling e) Microscopic photo of in-plane buckling. . . . .	74
Figure 5.3	Steered tow and load distribution in width direction due to steering. . . . .	75
Figure 5.4	a) The model of fiber embedded in matrix b) The model of fiber buckling on a viscoelastic foundation. . . . .	76

Figure 5.5	The generalized Maxwell model. . . . .	77
Figure 5.6	MCR-502 rheometer and prepreg sample placed on the lower fixture for relaxation test. . . . .	81
Figure 5.7	Illustration of a relaxation modulus test in the z-direction step by step performed with a rheometer. . . . .	82
Figure 5.8	Three repeated tests and the mean value curve for the tensile relax- ation test. . . . .	83
Figure 5.9	Fitting generalized Maxwell model on the relaxation modulus data in the out-of-plane direction. . . . .	84
Figure 5.10	Three repeated tests and the mean value curve for the shear relaxation test. . . . .	85
Figure 5.11	Fitting generalized Maxwell model on the relaxation modulus data in in-plane direction. . . . .	86
Figure 5.12	Upper and lower critical buckling load and radius for out-of-plane buckling and in-plane buckling. . . . .	86
Figure 5.13	Critical buckling load and radius for the three different mode shapes of in-plane buckling (waviness). . . . .	88
Figure 5.14	Top view of wrinkle shape with neutral axis position and wavelength changes. . . . .	89
Figure 5.15	The values of critical load over the length of the fiber before buckling and relaxation modulus. . . . .	90
Figure 5.16	Normalized two successive buckling loads versus the relaxation mod- ulus for in-plane buckling (waviness). . . . .	92
Figure 6.1	A schematic of prepreg tape model as a composite plate on Pasternak foundation. . . . .	97
Figure 6.2	Schematic of single-lap joint unidirectional prepreg specimen with dimensions . . . . .	100
Figure 6.3	The manufacturing procedure of the Single lap joint specimen . . . .	100

Figure 6.4	Two different compaction rollers and the values of four different levels of pressure were used in the preparation of SLJ samples. . . . .	103
Figure 6.5	Comparison of load-displacement curves for uncured prepreg tapes bonded (SLJ) samples under different loads. . . . .	104
Figure 6.6	Comparison of load-displacement curves for SLJ specimens fabricated at 25°C and 225N under three different feed rates and compacted by: (a) SSR and (b) PUR. . . . .	105
Figure 6.7	Comparison of load-displacement curves for SLJ specimens fabricated with the feed rate of 14 mm/s under different levels of pressures and temperatures: (a) 45 °C and (b) 25 °C. . . . .	107
Figure 6.8	Comparison of experimentally obtained failure load of uncured prepreg SLJ samples created under different process conditions. . . . .	107
Figure 6.9	Captured Micrographs of SLJ Samples Created with PUR under Varied Conditions: (i) 35 mm/s Feed Rate and 25°C and 225 N, (ii) 15 mm/s Feed Rate and 25°C and 225 N, (iii) 15 mm/s Feed Rate and 45°C and 225 N, (iv) 15 mm/s Feed Rate and 25°C and 289 N. . . . .	110
Figure 6.10	Captured Micrographs of the cross-section of SLJ specimens in the bonding area before the tensile test fabricated with PUR under Varied Conditions: (i) 35 mm/s Feed Rate and 25°C and 225 N, (ii) 15 mm/s Feed Rate and 25°C and 225 N, (iii) 15 mm/s Feed Rate and 45°C and 225 N, (iv) 15 mm/s Feed Rate and 25°C and 289 N. . . . .	111
Figure 6.11	FE model of the single lap joint: (a) configuration, and boundary conditions, (b) mesh details. . . . .	113
Figure 6.12	Verification and total energy dissipated by damage based on the FE model: (a) Comparison between the experimental and numerical load-displacement results. (b) Total energy dissipated by damage in each specimen.	114
Figure 6.13	Adhesive shear and peel stress distribution for uncured prepreg SLJ samples: (a) Adhesive shear distribution, (b) Peel stress distribution at the overlap area. . . . .	115

Figure 6.14	The results of the SLJ FE model: (a) Stress concentration in SLJ samples before failure, (b) Damage initiation in cohesive elements. . . . .	116
Figure 7.1	AFP head and a schematic diagram detailing the components of the AFP head. . . . .	121
Figure 7.2	The effect of natural axis position on load distribution. $E_i$ represent the stiffness for the area between the natural axis and inner edge (a) a steered tape under the linearly distributed load (b) a steered tape with some defects at the inner edge (c) a steered tape without any defects at the inner edge. .	126
Figure 7.3	Schematic of the new concave compaction roller, illustrating the roller parameters: $X$ , the horizontal distance from the roller's edge, and $R$ , the concave radius. . . . .	128
Figure 7.4	Finite element model of the concave roller (a) mesh details, (b) the simulation results. . . . .	131
Figure 7.5	The simulation results for the concave roller with the different values of $X$ and $R$ , P(Max, Min) shows the maximum and minimum pressure for each roller in MPa. . . . .	132
Figure 7.6	(a)-(c) Pressure distribution along the midline of the concave compaction rollers for various values of $R$ and $X$ . (d) Pressure distribution along the midline of the flat compaction roller. (e)-(g) Contact length spanning from one end of the concave roller to the other for various values of $R$ and $X$ . (h) Contact length spanning from one end to the other of the flat roller.	133
Figure 7.7	A flowchart illustrating the various stages in the design of the compaction roller. . . . .	134
Figure 7.8	Details of three-part mold and new compaction roller. . . . .	135
Figure 7.9	Comparison of pressure distribution results for concave and flat rollers: (a) Sensitive-pressure film measurements for both roller types, (b-c) Segmented processed images of the sensitive-pressure film data, (d) FE simulation of concave roller. . . . .	136

Figure 7.10 Comparison wrinkle length at steered tow placed by: (a) Concave roller and (b) standard roller. . . . .	138
Figure 7.11 Pressure distribution under the flat and concave roller (a) sensitive-pressure film (b) segmented processed image. . . . .	139

# List of Tables

Table 3.1	Process conditions. . . . .	23
Table 3.2	Measurement results (the number of wrinkles and the average length of wrinkles in each radi-us). . . . .	25
Table 4.1	Material properties of graphite composite material. . . . .	54
Table 4.2	The comparison of the buckling loads determined on the basis of the presented method and classical laminate theory . . . . .	55
Table 4.3	Comparing the buckling loads calculated using the presented method with those from the FE method. . . . .	60
Table 4.4	The effect of length-to-thickness ratio on buckling response. . . . .	61
Table 4.5	The effect of lay-up sequence on buckling response. . . . .	63
Table 5.1	AFP process conditions used during the steering. . . . .	72
Table 5.2	wavelength changes of wrinkles in the width direction. . . . .	89
Table 6.1	Process parameters' levels for fabrication of single-lap joint samples .	102
Table 6.2	Effect of process parameters on the geometry of the prepreg tape and SLJ overlap section. . . . .	108
Table 6.3	Mechanical properties of prepreg tape as an adherend for the SLJ simulation Belhaj and Hojjati (2018). . . . .	112
Table 7.1	PLA filament properties and 3D printer setting parameters. . . . .	134
Table 7.2	Freeman 2040 polyurethane elastomer physical properties. . . . .	135
Table 7.3	AFP process parameters utilized to assess the performance of the new roller during the steering process. . . . .	138

# Chapter 1

## Introduction and Motivations

Manufacturing and the manufacturing industry are regarded as the backbone of every economy. Nations that prioritize innovation in manufacturing are better prepared to mitigate the impacts of economic downturns, facilitating a quicker return to economic equilibrium. Economists commonly highlight the manufacturing sector's comparatively low but dependable return on investment. According to data from 2021 provided by the National Association of Manufacturers, manufacturing stands out with the highest multiplier effect of any economic sector. For every US dollar invested in manufacturing, an additional \$2.60 is generated in the economy which highlights the importance of manufacturing [Harik and Wuest \(2019\)](#); [NAM \(2021\)](#).

In the aerospace and automotive industries, carbon fiber-reinforced polymer (CFRP) materials have gained significant traction thanks to their high strength-to-weight ratio, and excellent specific mechanical and chemical resistance. To address the rising demand for composite parts, automated manufacturing processes such as automated fiber placement (AFP) are being developed to facilitate the production of more complex and intricate designs, such as tow steering, which were challenging to create with conventional methods. However, the formation of manufacture-induced defects is a major disadvantage of composite automated manufacturing. As composite materials play a pivotal role in the future of transportation, it is crucial to continue optimizing AFP technology. As a result, further research is needed to minimize manufacturing-induced defects, improve overall efficiency,

and enhance the quality of composite structures.

## 1.1 AFP technology and defect formation mechanism during the process

AFP is a state-of-the-art manufacturing process that significantly advances the production of both thermoset and thermoplastic composite materials. Its efficiency in creating lightweight, high-strength components with minimal waste has made it a preferred choice in industries such as aerospace, automotive, and wind energy. This method involves the automated placement of continuous fiber tows, often pre-impregnated with resin, onto a surface or mold to form intricate shapes and structures. AFP technology utilizes robotic systems equipped with six degrees of freedom (DOF) to enhance the precision and flexibility of the manufacturing process. These advanced robots are designed to move in multiple directions, allowing for complex motions and orientations that are essential for accurately placing continuous fiber tows onto molds or surfaces [Brasington, Sacco, Halbritter, Wehbe, and Harik \(2021\)](#); [Dirk, Ward, and Potter \(2012\)](#). Detailed descriptions of AFP technology will be provided in Chapter 2 of this thesis.

Despite the many advantages of AFP technology, the occurrence of various defects during the AFP process continues to pose a major challenge in the manufacturing industry, particularly during the steering process. As steering is a critical step in producing parts with complex geometries, these defects present a serious obstacle to achieving optimal quality. Steering-induced defects in the AFP process frequently occur when prepreg tapes are laid along a non-geodesic path over complex, potentially doubly-curved surfaces, or when they follow a steered trajectory on a flat surface. This results in a mismatch length between the inner and outer edges of the tape. This mismatch creates distinct stress states: compressive stresses on the inner radius and tensile stresses on the outer radius. The tensile and compressive loads are the primary contributors to defect formation in the steered tape. These defects can be generally categorized into three types: (1) out-of-plane deformations,

referred to as wrinkle defects, which occur on the inner edge due to compression; (2) in-plane deformations, referred to as waviness, which also arise from compressive stress on the inner edge; and (3) tape pull-off or tape folding, which happens on the outer edge due to tensile stress. Fig. 1.1 demonstrates the steering-induced defects during the steering in the AFP process.

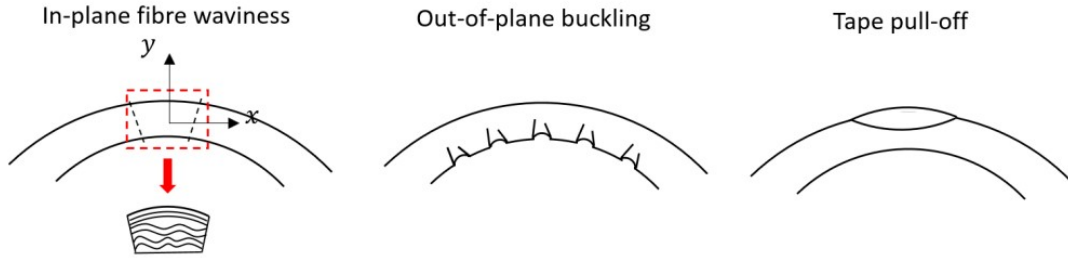


Figure 1.1: Automated fiber placement heat and the key components [Hörmann \(2015\)](#)

## 1.2 Research Motivation

As previously mentioned, AFP offers precise control over fiber placement, enabling the creation of tailored materials with exceptional mechanical properties. Given that AFP machines are primarily used to manufacture large, complex structures, steering the tow to ensure acceptable part quality is essential. However, steering prepreg tows along curved paths can introduce defects that may weaken the structural integrity of the finished product. Therefore, further research is needed to gain a deeper understanding of defect formation during the steering process in AFP. This requires a combination of experimental and analytical approaches to predict and mitigate defects during steering effectively.

This research aims to address the critical issue of steering-induced defects in the AFP process, with a specific focus on the thermoset AFP process. By developing accurate analytical models to predict defect formation, we can gain a deeper understanding of the underlying mechanisms and implement targeted strategies to mitigate their occurrence. Additionally, this research will explore the design and implementation of innovative compaction rollers to enhance the tow steering process and improve prepreg adhesion.

The overarching goal of this PhD thesis is to contribute to the advancement of composite manufacturing by providing a comprehensive framework for understanding and addressing steering-induced defects in AFP process. Through a combination of theoretical analysis, experimental validation, and innovative design, this research will enable manufacturers to optimize their AFP processes, produce higher-quality composite structures, and reduce costs.

### 1.3 Research Objectives

The objective of this PhD thesis is to develop analytical models that predict accurately both planar and non-planar deformations occurring during the steering process in AFP. The model aims to identify key parameters and analyze their influence on the formation of defects. By understanding these parameters, practical solutions will be proposed to reduce defects and enhance the quality of the AFP process.

To achieve this, the thesis employs macro- and micro-mechanical approaches to investigate the deformation behavior of steered prepreg slit tapes. Two plate buckling models are introduced to predict out-of-plane defects and define the critical steering radius based on AFP and material specifications. Additionally, recognizing the occurrence of in-plane defects, a micro-mechanical model is developed to predict both planar and non-planar deformations. This model treats the fibers as elastic materials and the resin matrix as a viscoelastic foundation, enabling the prediction of fiber buckling and associated defects.

Analytical modeling of the defects highlights the critical role of prepreg tack in defect formation. To further investigate this, a series of single-lap joint (SLJ) experiments are conducted to examine the interlaminar bonding behavior under various process conditions. Finally, based on the insights gained from these experiments and the defect modeling, a novel compaction roller is designed to optimize the steering process and reduce defect formation.

Through a combination of theoretical analysis, experimental validation, and innovative design, this thesis seeks to optimize AFP processes, leading to higher-quality composite

structures and more cost-effective manufacturing.

## 1.4 Thesis Layout

This thesis follows the Concordia manuscript-based thesis guideline and is divided into chapters as below:

**Chapter 2:** This chapter presents the background of the research and reviews previous studies on manufacturing defects in AFP.

**Chapter 3:** Focuses on studying wrinkle formation in prepreg tows with considering the initial imperfections during the AFP. A theoretical model is developed and experimentally validated, demonstrating that increased initial imperfections lead to an increased occurrence of defects in steered tows.

**Chapter 4:** In this chapter, a novel analytical method is developed using three-dimensional elasticity to predict out-of-plane deformation in composites. This method is effectively able to incorporate interlaminar imperfections in its predictions of out-of-plane deformation.

**Chapter 5:** explores the in-plane and out-of-plane deformations of thermoset tow prepreps during the steering process, utilizing a viscoelastic micro-mechanics approach to model the resultant waviness and wrinkle defects. The chapter presents a fiber-buckling model to analyze the deformation behavior, derive critical radii for both deformation types, and establish the relationship between relaxation modulus values and mixed-mode planar buckling.

**Chapter 6:** This chapter details a series of single-lap joint experiments to evaluate the interlaminar bonding strength between prepreg tapes under varying AFP process conditions. The objective is to identify the optimal process parameters that result in the strongest bond. The goal is to determine the ideal process parameters that maximize interlaminar bonding strength.

**Chapter 7:** This chapter introduces a novel compaction roller designed to reduce out-of-plane defects in AFP manufacturing. By applying variable pressure and contact length

based on part geometry, the new roller significantly decreases wrinkle formation, demonstrating a 24% reduction in wrinkle length compared to standard rollers.

**Chapter 8:** Lastly, the conclusions of this research are presented, along with a discussion of possible directions for future work.

## Chapter 2

# Literature Review

In this chapter, we provide a comprehensive review of the literature related to the automated fiber placement (AFP) process, with a particular focus on defect formation. This chapter begins with an in-depth exploration of the thermoset AFP process, outlining the key components, mechanisms, and equipment used to achieve precision in composite manufacturing. Following this, we examine the properties and preparation of thermoset prepreg materials, which play a critical role in AFP applications. Furthermore, the challenges posed by steering defects, including their impact on mechanical properties and laminate performance, are discussed. To address these challenges, we delve into both experimental and analytical approaches.

### 2.1 The thermoset AFP process

As stated in the introduction, thermoset AFP is a cutting-edge technology that utilizes a six-degree-of-freedom robot, allowing for the fully automated production of CFRP components with consistently high quality throughout the manufacturing process. The AFP systems are composed of several key components, including the placement head, roller, heating mechanism, and mandrel. Each plays a vital role in ensuring precision and efficiency in the fiber placement process [Harik and Wuest \(2019\)](#); [MAHAPATRA \(2023\)](#):

**Placement head:** The placement head is the core component of the AFP machine,

responsible for precisely laying down fiber tows onto the tool. It controls key process parameters such as compaction force, tow tension, cutting, and heating, using a combination of rollers, tensioners, and heating elements to ensure accurate deposition.

**Compaction roller:** The compaction roller is responsible for compressing the deposited fiber tow and ensuring proper resin penetration, leading to improved material integrity and adhesion.

**Heating system:** To ensure proper curing and adhesion of the resin matrix, AFP machines employ a heating system. This system can utilize various methods, such as infrared (IR) heating, hot air, or laser heating, to apply the necessary temperature to the uncured prepreg tapes.

**Automation and control system:** The AFP machine's movements are precisely programmed by a computer numeric control system, ensuring that the placement head accurately follows the programmed trajectory and deposits fiber tows as intended. The entire process is typically automated and controlled by a computer system, allowing for precise parameter programming, real-time monitoring, and seamless integration with other manufacturing systems.

**Mandrel:** The mandrel provides support for the tool on which the material is deposited. It can be flat or cylindrical, depending on the component being manufactured, such as complex panels or cylindrical structures.

### 2.1.1 AFP equipment used in this thesis

A commercial thermoset AFP machine from Automated Dynamics Inc., located at the Concordia Center for Composite (CONCOM), has been utilized in this thesis to deposit the prepreg tow onto the aluminum substrate. This 6-axis articulated robot can apply up to four prepreg tows on the tool per course, allowing for arbitrary lengths of tow cuts exceeding 3 inches, with the capability to restart at any point during the lay-up process. To ensure compaction pressure is effectively applied to the incoming tapes, the AFP machine features a perforated polyurethane roller with an outer diameter of 38 mm, consistent with standard roller dimensions, a hardness rating of 60 durometer, and height deviations from

the mean line of the roller measuring  $0.244 \mu\text{m}$ . Additionally, a nitrogen hot gas torch is employed for heating during the process, facilitating optimal adhesion and curing of the prepreg materials. This setup enables precise control over the lay-up process, enhancing the quality and performance of the composite parts produced. Fig. 2.1 shows the thermoset automated fiber placement head and its key components used in this thesis.

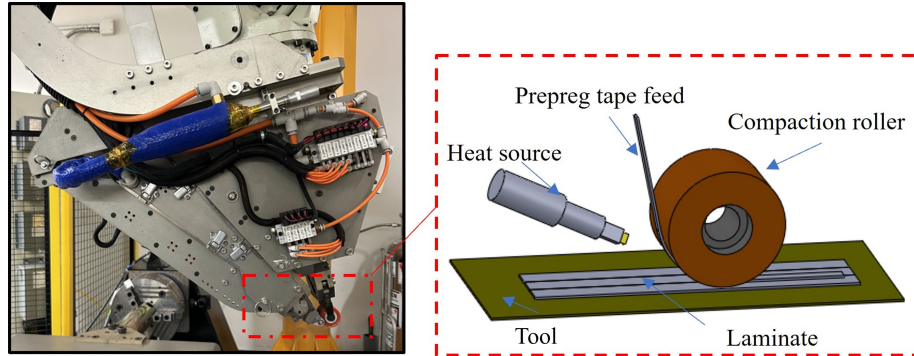


Figure 2.1: Thermoset automated fiber placement head and the key components

## 2.2 Thermoset prepreg material

Thermoset prepreps used in the thermoset AFP manufacturing process are composite materials consisting of unidirectional or woven carbon fibers impregnated with a partially cured thermosetting resin. To prevent premature curing, prepreps are typically stored in refrigerated conditions at  $-18^{\circ}\text{C}$ . These materials must be slit to the required width depending on the AFP machine configuration, e.g.  $1/8''$  (3.175 mm),  $1/4''$  (6.35 mm), or  $1/2''$  (12.7 mm). In the process of producing prepreg tape, the parent tape is passed through a slitter set to the desired width and then wound onto cardboard spools along with a backing film that prevents the slit tape from adhering to the material underneath during spooling [Heller \(2022\)](#); [Peters \(2013\)](#). The thermoset prepreg material used in this work is a 6.35 mm wide CYCOM 977-2 unidirectional carbon fiber thermoset prepreg tape supplied by Bombardier Inc., Canada. The prepreg fiber content is 60% by volume with a thickness of 0.17 mm [Kheradpisheh and Hojjati \(2023\)](#). Fig. 2.2 shows the prepreg tape spool used in this research.

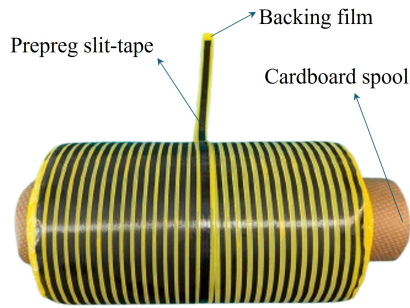


Figure 2.2: Prepreg slit-tape spool

## 2.3 Steering process and defects mechanics during steering

AFP allows for innovative laminate design by placing uncured thermoset prepreg slit-tapes along non-geodesic paths within a ply, a technique known as steering. Fig. 2.3 shows placing the tow on curvilinear paths.

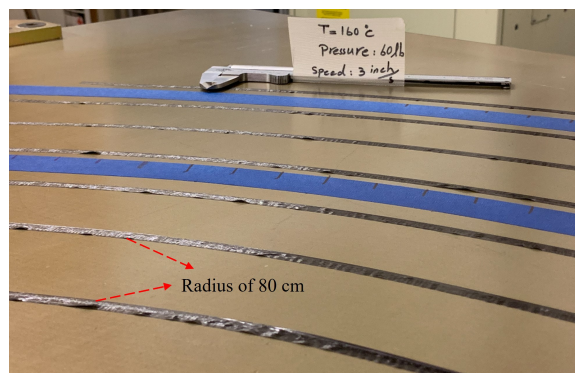


Figure 2.3: Steered tape manufactured by thermoset automated fiber placement

During the steering process, each slit-tape is flexed in the plane of the surface, which induces compression in the fibers along the inner edge and tension along the outer edge of the slit-tape. Employing unidirectional slit-tapes enables precise fiber alignment with primary load directions, optimizing stiffness in the composite laminate by varying the fiber orientation angle [Dirk et al. \(2012\)](#); [Hörmann \(2015\)](#).

As highlighted in Chapter 1, steering the prepreg tape during the layup process can lead to defects, which in turn reduce the mechanical properties and negatively affect the overall quality of the final product. Compression at the inner edge of the steered tape can cause

in-plane fiber waviness and out-of-plane wrinkles, while tension at the outer edge may lead to tape-folding if the adhesion between the prepreg and the substrate is insufficient. This adhesion between the prepreg and the substrate is commonly referred to as prepreg tack in the literature. Fig. 2.4 shows the different types of defects during the steering process.

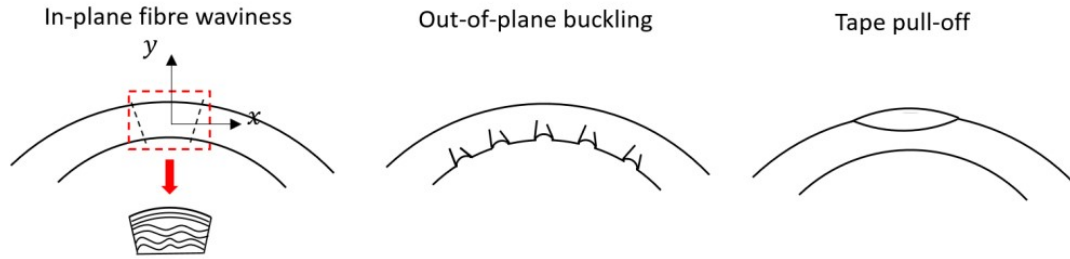


Figure 2.4: Overview of different types of defects at a steered prepreg tape [Hörmann \(2015\)](#)

### 2.3.1 The effect of AFP defects on mechanical properties

A substantial body of research has investigated the impact of various defects on the structural performance of cured laminates. Numerous studies have focused on gaps and overlaps, which can be introduced manually or through the AFP process [Adams and Hyer \(1996\)](#); [Adams and Hyert \(1994\)](#); [Lan, Cartié, Davies, and Baley \(2015, 2016\)](#); [Mukhopadhyay, Jones, and Hallett \(2015b\)](#); [Woigk et al. \(2018\)](#). In this context, Croft et al. [Croft et al. \(2011\)](#) conducted a comprehensive study on the effects of defects from the AFP process on the mechanical performance of composite materials, focusing on four types of defects: gap, overlap, half gap/overlap, and twisted tow. Experiments were performed to evaluate tensile, compressive, in-plane shear, open-hole tension (OHT), and open-hole compression (OHC) at both the lamina (individual layer) and laminate (layered structure) levels. Their results showed that isolated defects had minimal impact on strength at the lamina level, with about a 5% reduction, while at the laminate level, strength reductions were up to 13%. The work in [Hörmann \(2015\)](#) studied the effect of steered defects on the mechanical properties of specimens fabricated by the AFP process. Their findings revealed that in-plane fiber waviness resulting from steering significantly diminishes the mechanical performance of steered laminates, causing reductions of up to 14% in ultimate laminate

compressive strength and 16% in failure strain. They showed that steering the tow along a curvature of 60 cm negatively impacted laminate performance, significantly decreasing the average Young's modulus in the fiber direction as waviness increased. In contrast, laminates produced with tows having a curvature of 80 cm showed a lesser effect, which was more related to test result variations than to the influence of fiber waviness. Mukhopadhyay et al. [Mukhopadhyay, Jones, and Hallett \(2015a\)](#); [Mukhopadhyay et al. \(2015b\)](#) investigated the impact of wrinkles embedded in laminate on tensile and compressive resistance of composites specimens. Their results showed a reduction in tensile and compressive strength ranging from 25% to 36%. Based on the aforementioned studies, it can be concluded that these defects are widely recognized for their detrimental effects on composite integrity, as emphasized in the literature review.

## **2.4 Experimental and analytical approaches to investigate steering**

Reducing and eliminating defects has become a key focus for both researchers and industry professionals, as they aim to improve the reliability and performance of composite structures produced using AFP. As mentioned, one of the most significant defects occurring during steering in the AFP process is out-of-plane deformations, commonly known as wrinkle defects [Rajan et al. \(2019\)](#). These defects are particularly problematic because they remain even after autoclave processing, impacting the quality of the final part. Due to the necessity of steering in the manufacturing of large structures, extensive research has been dedicated to experimentally and analytically investigating defects in the steering process. The related works can be classified into two main categories: experimental studies examining in-plane and out-of-plane defects during the steering process, and publications that focus on finite element and analytical models of in-plane and out-of-plane buckling.

### Experimental works:

Rajan et al. [Rajan et al. \(2019\)](#) conducted a thorough experimental study examining the formation of defects when the prepreg tape is steered along a curved path. Their study showed that decreasing the path curvature increases the number of wrinkles, which is attributed to the rising in-plane load in the prepreg tape. The work in [Bakhshi and Hojjati \(2018\)](#) presented an extensive series of AFP experiments to investigate the defect formation in the steering process. They carried out trial and error experiments to find the optimum process parameters to avoid defects during the AFP manufacturing process. The authors of [Fischer, Horn, Bartelt, and Blöchl \(2015\)](#) conducted experimental investigations on structures with complex geometry in the AFP process, and proposed a path placement method to enhance the mechanical properties of steered tapes during manufacturing. The authors in [R. Wehbe, Sacco, Radwan, Albazzan, and Harik \(2020\)](#) investigated the impact of various process parameters, namely temperature, head speed, and compaction force, on the quality of steered tow on a cylindrical mold. Their findings revealed that course curvature is the most critical factor in defect formation, whereas layup speed had minimal impact. Additionally, a negative correlation between temperature and defect rates was observed, indicating that higher temperatures help reduce defects. The work in [Tang, Wang, Wang, Li, and Ke \(2022\)](#) focused on evaluating the occurrence of wrinkles and waviness in specimens fabricated by AFP machine, which resulted in a reduction of about 12% in the bending properties of the specimens. Additionally, [H. Hu, Cao, Cao, and Li \(2021\)](#) examined the effect of non-planar wrinkle defects on the failure behavior of an L-shaped composite laminate. They demonstrated that wrinkles led to delamination and changed the failure propagation process, causing a notable decrease of around 30–40% in the loading capacity of L-shaped laminates. In [Mizukami, Mizutani, Todoroki, and Suzuki \(2016\)](#), a novel experimental approach for detecting in-plane and out-of-plane defects in unidirectional carbon fiber-reinforced plastics was proposed. The approach utilized an eddy current probe, which is engineered to yield a zero output in intact areas, thus providing signals exclusively in the presence of waviness, significantly enhancing its sensitivity. Hormann

Hörmann (2015) investigated the effects of fiber waviness on the mechanical properties of cured thermoset prepreg through mechanical testing, which included tensile, compression, and bending experiments. Their findings indicated that the compressive properties were the most significantly impacted by the degree of waviness defects in the laminate.

**Analytical works:**

To better understand defect formation during the AFP steering process, theoretical modeling has been developed alongside experimental work. Beakou et al. (2011) were the first to present an analytical buckling model to predict wrinkle defects during steering. In their model, the prepreg tape was treated as a plate supported by an elastic foundation of normal springs to represent the tackiness between the prepreg and substrate. Their model is presented in Fig. 2.5.

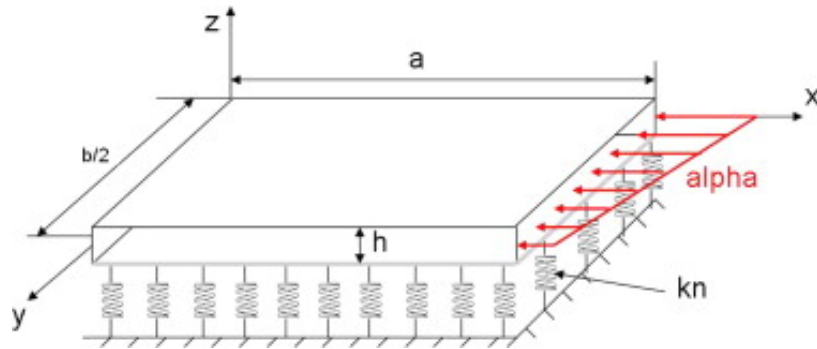


Figure 2.5: The model presented for wrinkle formation by Beakou et al. (2011)

Matveev et al. (2016) improved the analytical model for wrinkle defect formation in steered prepreg tape by mathematically predicting a critical steering radius beyond which defects do not occur. Their study highlighted the crucial influence of the tackiness between the prepreg and substrate (elastic foundation) on the formation of defects. Moreover, Belhaj et al. (2018) studied the influence of the shear parameter on wrinkle formation. They incorporated the shear parameter into their analytical model and used a new formula to model the prepreg tack (Pasternak elastic foundation). Their proposed approach enhanced the precision of predictions related to defect occurrence. Additionally, Rajan et al. (2020) incorporated the effect

of shear in a finite element model, utilizing a cohesive zone model that accounts for both normal and shear parameters to represent the prepreg's tackiness to the substrate during wrinkle formation.

The study by [Bakhshi and Hojjati \(2019\)](#) explored the viscoelastic properties of prepreg tack and their impact on wrinkle defects. In their research, they substituted the elastic foundation model with a viscoelastic model to examine the time-dependent behavior of these defects.

Analytical and experimental studies indicate that the stickiness of prepreg tape to the substrate, referred to as prepreg tack, significantly influences defect formation during the AFP process. Various process parameters—including pressure, temperature, feed rate, and contact time—as well as environmental factors such as aging and humidity, affect prepreg tack. Consequently, understanding the relationship between prepreg tack and these variables is crucial for optimizing the AFP process and reducing defects [Belhaj, Dodangeh, and Hojjati \(2021\)](#); [Budermann, Detampel, Schmidt, and Meiners \(2019\)](#); [Budermann, Schmidt, and Meiners \(2020\)](#); [Wohl et al. \(2017\)](#).

Research by [Heller, Böckl, Ebel, and Drechsler \(2018\)](#) demonstrated that material aging negatively impacts steering behavior in the AFP process, resulting in defects such as fiber waviness and buckling. Additionally, [Belhaj et al. \(2021\)](#) examined the influence of AFP process parameters on prepreg tack through peel-off tests, measuring adhesion under varying conditions. [Buderman et al. \(2019\)](#); [Budermann, Schmidt, and Meiners \(2021\)](#) employed a rheometer to assess prepreg stickiness using a probe tack test, revealing how variations in pressure and temperature affect tack.

To better simulate AFP conditions, [R. Crossley, Schubel, and Warrior \(2012\)](#); [R. J. Crossley, Schubel, and De Focatiis \(2013\)](#) developed a peel test apparatus that measures prepreg tack at a normal angle (90 degrees), allowing for an analysis of how pressure and feed rate impact peel resistance. The effects of process parameters on the shear and thermal properties of carbon fiber-reinforced thermoplastic (CFRTP) composites produced via AFP were investigated by [Venkatesan, Zulkifli, and Silva \(2023\)](#), who optimized these parameters to improve interlaminar shear strength. The study in [Endruweit et al. \(2018\)](#) explored prepreg

tack across various substrate materials and process parameters.

Several studies have specifically addressed the effect of pressure on prepreg tack, particularly with thermoset prepreg tapes, focusing on pressure distribution and the role of compaction rollers during the AFP process. For example, [Etchegaray Bello, Engelhardt, Bublitz, and Drechsler \(2022\)](#); [Vogl, Knott, Sommacal, Compston, and Drechsler \(2024\)](#) examined the influence of compaction and curing states on the mechanical properties and void content of AFP-manufactured laminates through various mechanical tests and micro-CT analysis. Research by [Bakhshi and Hojjati \(2020\)](#) analyzed the pressure distribution from compaction rollers with varying stiffness, indicating that stiffer rollers produce higher-quality laminates.

The study by [Lu, Evans, and Turner \(2023\)](#) developed and validated a finite element model to analyze the compaction pressure exerted by rollers in Automated Dry Fibre Placement, investigating how roller material, tool curvature, and substrate thickness affect pressure distribution and prepreg tack. Furthermore, [He, Jiang, Qu, and Ke \(2022\)](#) modeled and experimentally validated the effects of segmented compaction rollers on pressure distribution on complex surfaces, demonstrating how these rollers improve pressure uniformity and prepreg tack, thus enhancing part quality. Lastly, [Ammar and Shirinzadeh \(2021\)](#) examined the impact of different compaction rollers on laminate quality using image processing methods to assess defects, finding that laminates produced with steel rollers had superior quality compared to those made with polyurethane and perforated rollers.

## 2.5 Conclusion Remarks

This literature review highlights the intricate relationships between the AFP process, prepreg materials, and the challenges of defect formation. The studies discussed underscore the importance of addressing these defects to improve the mechanical performance and reliability of composite parts manufacturing using the AFP.

According to the literature review, it is shown that despite the research progress in modeling the defect formation within the AFP process, there remains significant scope for

improvement. For instance, current models often overlook the impact of initial imperfections, such as the initial deformation of the prepreg spool, deformations that occur as the tape passes through the guidance system, and any minor defects present on the substrate that can contribute to defect formation. Additionally, since prepreg materials are composites made up of fibers and resin, it may be beneficial to propose a micromechanics model to effectively capture both in-plane and out-of-plane deformations during the steering process.

Furthermore, the literature indicates that most studies recommend a critical radius for steering to minimize defects. However, additional strategies to mitigate defect formation during steering, such as the introduction of innovative compaction rollers and the optimization of process parameters, deserve further investigation. These adjustments could play a pivotal role in refining the AFP process, thereby enhancing the quality and performance of composite structures.

## Chapter 3

# Wrinkle formation and initial defect sensitivity of steered tow in automated fiber placement

This work has been published in:

Kheradpisheh, Meisam, and Mehdi Hojjati. "Wrinkle formation and initial defect sensitivity of steered tow in automated fiber placement." *Journal of Composites Science* 5.11 (2021): 295.

### 3.1 Abstract

This paper aims to study the wrinkle formation of a prepreg with initial defect during steering in automated fiber placement (AFP). Wrinkle formation has a detrimental effect on the mechanical properties of the final product, limiting the AFP applications. A theoretical model for wrinkle formation has been developed in which a Pasternak foundation and a Koiter imperfection model are adapted to model viscoelastic characteristics of the prepreg tack and initial defect of the prepreg, respectively. The initial defect is defined as a slight deviation of the tow's mid-plane from a horizontal shape. The initial defect is generated

in the tow by moving the tow through the guidance system and the pressure of the roller. Galerkin method, along with the finite difference method (FDM), are employed to solve the wrinkle problem equation. The proposed method is able to satisfy the different boundary conditions for the wrinkle problem completely. The numerical results show that increasing the initial defect leads to a decrease in critical load and an increase in critical steering radius. To validate the theoretical model, experimental results are presented and compared with model-predicted results. It is shown that the model is well able to capture the trends and values of wrinkle formation wavelengths obtained from the experiment.

## 3.2 Introduction

An increase in demand and operating conditions has resulted in the need for composite structures. To meet the increasing demand, automated fiber placement (AFP) offers excellent benefits that reduce costs and increase the production rate. Therefore, the AFP is becoming increasingly important for many applications in various industries. During the AFP process, the pre-impregnated tapes are placed on the tool, utilizing the AFP head. One of the significant advantages of AFP is that one manages to control the speed of each tow, and this advantage contributes to tow steering and the design and manufacturing of structures with complex geometries [Croft et al. \(2011\)](#); [Heinecke and Willberg \(2019\)](#).

A primary concern during steering using automated fiber placement is the prepreg out-of-plane buckling, which significantly lowers the mechanical properties of the products [Beakou et al. \(2011\)](#). Indeed, the steering curvature causes the inner edge of the tape to be under compression and the outer edge to be under tension. The values of compressive load and bending load applied to tow are controlled by the value of steering radius. A decrease in steering curvature is associated with increasing the compressive load. This compressive load causes out-of-plane wrinkle formation in the inner edge [Beakou et al. \(2011\)](#); [Belhaj and Hojjati \(2018\)](#).

Although a considerable amount of literature has been published on buckling of laminate composite, the number of papers focusing on the buckling during the steering in automated

fiber placement is not significant. Given the significance of control of different types of defects such as wrinkle formation in the AFP and manufacturing process, efforts have been made to study and understand these subjects. Panday and Sun [Panday and Sun \(1999\)](#) studied wrinkle formation of the composite laminate by two different methods. In the first approach, they modeled the interface bonding by a set of shear and normal springs and calculated the buckling load for a composite laminate. The second approach employed a large deflection theory to obtain the governing equation for predicting wrinkle behavior. Ma et al. [X. Ma, Butterworth, and Clifton \(2007\)](#) studied the unilateral contact Local buckling of multilayered composite resting on elastic foundation. They employed the transfer function method to solve the buckling model and investigate the effect of elastic foundation parameters on buckling load. Beakou et al. [Beakou et al. \(2011\)](#) studied out-of-plate buckling of tape during the automated fiber placement process. They presented a simply supported buckling model of the plate under linearly varying in-plane load for the wrinkle formation of tow. Their experimental data showed that predicting the wrinkle formation can be improved by considering tack's temperature and dynamic behavior. Lightfoot et al. [Lightfoot, Wisnom, and Potter \(2013\)](#) investigated a new mechanism for the wrinkles formed in the prepreg composites due to thermal shear force. They showed that removing the release film decreases the possibility of wrinkle formation, which supported their proposed mechanism. The effect of steering curvature on wrinkle formation was performed by Matveev et al. [Matveev et al. \(2016\)](#). They defined wrinkle formation as a buckling model for a plate resting on an elastic foundation and used experimental findings to predict the parameters of wrinkle formation. The effect of in-plane shear modulus on wrinkle formation was investigated [Belhaj and Hojjati \(2018\)](#). They measured in-plane shear modulus of prepreg using the  $\pm 45^\circ$  tensile test. Their results show that the shear modulus in the wrinkle equation leads to a better agreement with the experimental results. Bakhshi and Hojjati [Bakhshi and Hojjati \(2019\)](#) performed a theoretical and experimental study on wrinkle formation of steered slit tow. The authors used the Rayleigh-Ritz and Laplace method to solve the problem of wrinkle formation. Besides, they presented a time-dependent elastic foundation model for modeling the tack properties. Rajan et al. [Rajan et al. \(2019\)](#) experimentally

investigated the wrinkle formation in prepreg slit tape. They employed a Stereo DIC technology to measure the displacement and strains during and after experiments. They found the amplitude of wrinkles was related to the time and temperature and doubled after the placement process because of the time-dependent viscoelastic properties of the tape. Wehbe et al. [R. Wehbe, Tatting, et al. \(2020\)](#) investigated the tow wrinkle on an arbitrary surface mathematically in the AFP process. They presented a mathematical model using the geodesic path and curvature definition that estimated the wrinkle amplitude. The effect of different parameters such as head speed and compaction force on steered tow on a cylindrical tool was studied by [R. Wehbe, Sacco, et al. \(2020\)](#). They evaluated the quality of the product based on the different combinations of these parameters and determined the importance of the parameters using the RReiliefF algorithm.

Imperfection in the composite laminate can be divided into two categories: imperfect interface and initial defect. In the former case, imperfection is defined as a weak bonding between layers [Bakhtiari and Kheradpisheh \(2020\)](#); [Cheng, Kennedy, and Williams \(1996\)](#). This imperfection can be modeled as a thin interface joining two adjacent layers by distributed springs [Chen, Cai, and Ye \(2003\)](#). In the latter case, the initial defect is defined as a slight deviation of the midplane from the horizontal shape. During the AFP process, the initial defect may be caused in tow by the contact pressure of the roller and moving the tow through the guidance system. In recent years, researchers set out to study the effect of the initial defect (imperfection) in buckling problems. Shariat et al. [Samsam Shariat and Eslami \(2005\)](#) studied buckling load of simply supported functionally graded plates with an initial defect under uniform in-plane edge load. They employed the Galerkin method to simultaneously solve the buckling and compatibility equations to calculate the buckling load of the imperfect plate. Thermoelastic buckling of the imperfect orthotropic and isotropic plates under different thermal loading was investigated by [Mossavarali, Saheli, and Eslami \(2000\)](#). Kiani et al. [Kiani, Bagherizadeh, and Eslami \(2012\)](#) presented an approximate close-form solution along with the Galerkin method to solve critical thermal buckling load for a sandwich FGM plate resting on Pasternak elastic foundation.

There is a growing need for detailed research on induced defects by automated fiber

placement processes. As discussed above, there seems to be no detailed study on the wrinkle formation during the steering process considering the initial defect effect of the tape on the wrinkle. In this work, a theoretical model is presented for the wrinkle formation of the tape with an initial defect resting on the Pasternak foundation. Galerkin method in conjunction with the finite difference method are employed to analyze buckling load and critical steering radius of tape and give an interpretation of how a slight initial defect affects these parameters. The method proposed in this study can be employed to solve wrinkle equations for different boundary conditions just by changing the finite difference coefficients. The model predictions for the values of buckling wavelengths are validated with experimental results.

### 3.3 Experiments

An AFP machine provided by Automated Dynamic Inc. was employed to fabricate the experimental samples on the surface, as shown in Figure 1a. This machine has a robot arm with six degrees of freedom, able to lay up both thermoset and thermoplastic composites. The number of tows used for adding lay-up by the head of the machine varies from one to four per each course. The tows can be cut in arbitrary lengths over the 3 inches and restarted during the lay-up process at any time. The AFP machine is equipped with a compaction roller and a hot gas as a heat source that provides pressure contact and a necessary temperature for bonding the tows on the tool, respectively. The compression force applied and controlled by the roller plays a vital role in the mechanical properties of tack and wrinkle formation. The compaction pressure distribution generated by roller on prepreg was investigated in [Bakhshi and Hojjati \(2020\)](#); [Jiang, He, and Ke \(2019\)](#), respectively. Besides, the compression force between the roller and tape and the guidance system leads to an initial defect in tape that affects the wrinkle formation. Figure 3.1b,c demonstrates the roller-tape contact and guiding system.

The tows used in this experiment were carbon/epoxy unidirectional prepreg (CYCOM 977-2/HTS-145 ) with an individual tow width of 6.35 mm, thickness of 0.2 mm, and a 60%

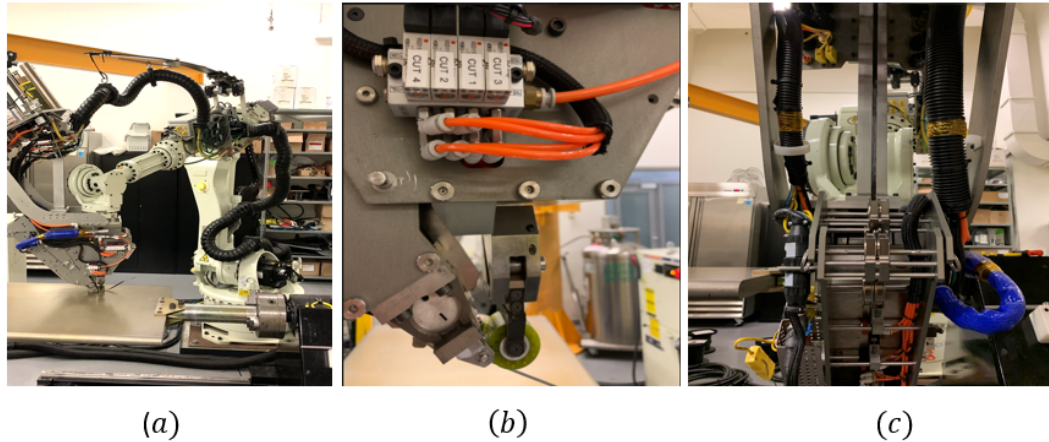


Figure 3.1: Automated fiber placement machine: (a) fiber placement with a six-axis robot arm, (b) the head and the roller-tape contact, (c) the guidance system.

Table 3.1: Process conditions.

Head Speed	Hot Gas Temperature (Heat Source)	Flow Rate (Heat Source)	Roller Force	Tool Temperature
77 mm/s	160 °C	85 (L/min)	250 N	23 °C

fiber volume. The prepregs were made of 12K carbon fibers (HTS-145), which were pre-impregnated with CYCOM 977-2 epoxy resin system and cured using an autoclave or press molding. To get experimental results, firstly, the thermoset prepregs were left to rest for 30 min at room temperature. A sketch was made by AFP machine’s software for determining the tow’s path on an aluminum tool. The dimensions of this path are shown in Figure 3.2.

Then, the thermoset prepregs were left to rest for 30 min at room temperature. After that, the tows were stored on the lay-up head and directly delivered from the spools to the roller to be steered on the rigid aluminum tool. The aluminum tool was cleaned with acetone before each experiment to reduce the shear force created by friction between the tool and prepreg. Finally, prepreg tows were deposited on an aluminum tool with different steering radii of 55, 60, 65, 67, 70, and 75 cm, according to Figure 3.2. The process of steering the tape was proceeded for this experiment by adjusting the AFP software according to Table 3.1.

The steering radius is created by rotating the head. The head rotation generates a lin-early varying load in prepreg, which in turn can lead to tow buckling. The experimental

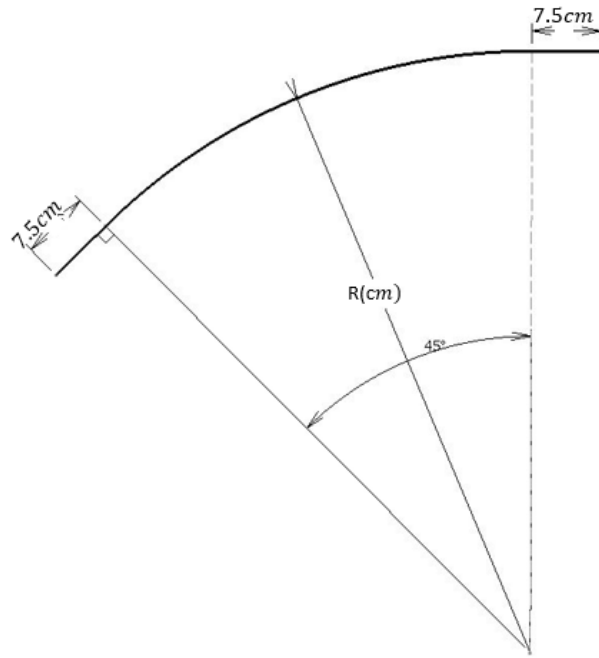


Figure 3.2: The tow's path made by AFP machine's software.

work observed that the wrinkle is formed when the tapes are placed on the surface with a radius of less than a specific value (critical radius). Figure 3.3 demonstrates the steered tow and wrinkle formation (out-of-plane buckling) in the tow.

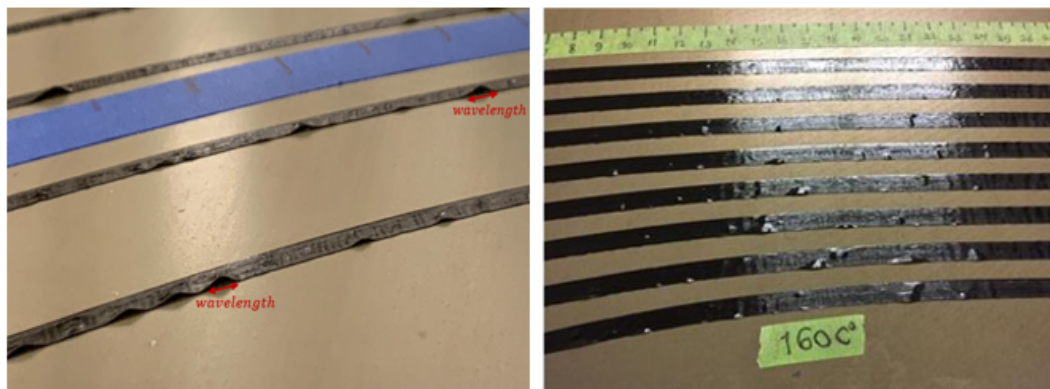


Figure 3.3: Steered prepreg on aluminum tool and wrinkle formation generated in tows.

One of the critical parameters in the process of steering the tows is the wavelength of the wrinkle, defined as the length of an opening separation of an individual wrinkle (see Figures 3.3 and 3.4).

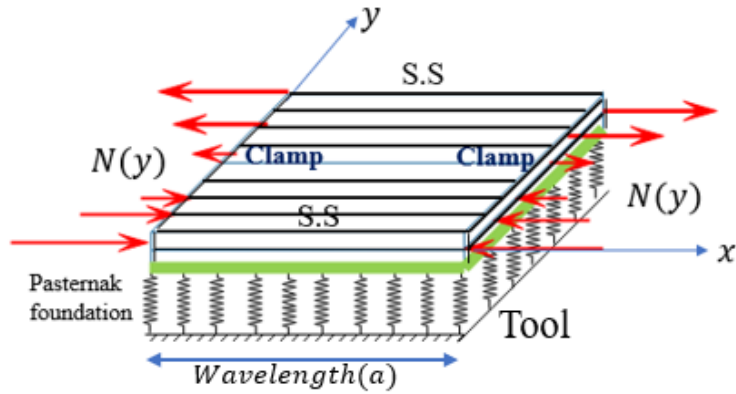


Figure 3.4: Schematic of a section of tape resting on elastic foundation under combined axial compression and bending.

Table 3.2: Measurement results (the number of wrinkles and the average length of wrinkles in each radi-us).

Steering Radius (cm)	Number of Wrinkles	Average of Wavelength (mm)
55	16	6.2
60	15	6.6
65	14	7
67	14	7.4
70	9	8
75	6	9

The length of the wrinkles (wavelength) is measured using a caliper manually in each tow. The average of the wrinkle's lengths in each steered tow is considered the wrinkles' wavelength in that certain radius. Table 3.2 represents the number of wavelengths and the average length of wrinkles in each steering radius.

In the following, based on the experiments, the authors aim to present a developed buckling formulation to model the wrinkle formation in tows. To validate the proposed model, the wavelengths of wrinkles measured manually in experiments are compared with the model predictions.

## 3.4 Formulation

### 3.4.1 Buckling model

Out-of-plane wrinkle formation of steered tows during the automated fiber placement process can be modeled as a buckling problem of a rectangular plate resting on a Pasternak elastic foundation, which is under non-uniform load. The load is applied by a roller to two clamped edges, and the other two edges are considered as a simply support (S.S) condition in accordance with the geometry of the problem. Figure 4 shows the theoretical model of wrinkle formation during steering.

### Pasternak Elastic Foundation

In this paper, a Pasternak foundation representation is adopted to model the mechanical properties of the tool and prepreg tack [Kerr \(1965\)](#); [Thai and Choi \(2011\)](#). Figure 3.5 shows the free body diagram of adhesive joint and elastic modeling based on the Pasternak model. This model replaces the elastic foundation as a combination of the shear layer and normal linear spring. As a result, the pressure of the elastic foundation surface can be mathematically written as:

$$p = K_f w - G \nabla^2 w \quad (1)$$

where  $p$  is pressure,  $\nabla^2$  is Laplace operator, and  $K_f$  and  $G$  are spring and shear constants of the Pasternak model, respectively.

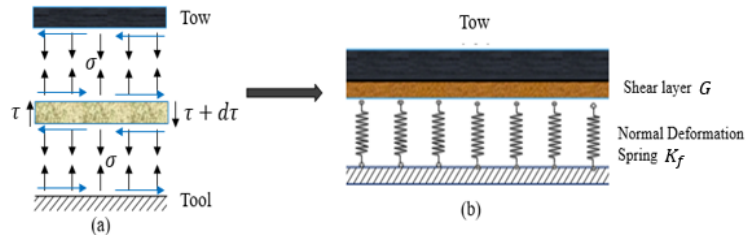


Figure 3.5: Elastic foundation: (a) free body diagram adhesive joint, (b) Pasternak elastic foundation model.

## Governing Equation

Assuming that the thickness is constant through the  $z$ -direction and using classical lamination plate theory CLPT theory, the equilibrium equations for a general thin composite plate can be expressed as [J. N. Reddy \(2003\)](#):

$$\begin{aligned} \frac{\partial N_{xx}}{\partial x} + \frac{\partial N_{xy}}{\partial y} &= 0 \\ \frac{\partial N_{xy}}{\partial x} + \frac{\partial N_{yy}}{\partial y} &= 0 \\ \frac{\partial^2 M_{xx}}{\partial x^2} + 2\frac{\partial^2 M_{xy}}{\partial x\partial y} + \frac{\partial^2 M_{yy}}{\partial y^2} + N_{xx}\frac{\partial^2 w}{\partial x^2} + 2N_{xy}\frac{\partial^2 w}{\partial x\partial y} + N_{yy}\frac{\partial^2 w}{\partial y^2} + p &= 0 \end{aligned} \quad (2)$$

where  $w$  is the displacement component along the  $z$ -direction;  $p$  is the elastic foundation pressure; and  $(N_{xx}, N_{xy}, N_{yy})$  and  $(M_{xx}, M_{xy}, M_{yy})$  are the in-plane force and moment resultants, respectively, that can be defined as:

$$\begin{aligned} \begin{bmatrix} N_x \\ N_y \\ N_{xy} \end{bmatrix} &= \begin{bmatrix} A_{11} & A_{12} & A_{16} \\ A_{12} & A_{22} & A_{26} \\ A_{16} & A_{26} & A_{66} \end{bmatrix} \begin{bmatrix} \epsilon_x^0 \\ \epsilon_y^0 \\ \gamma_{xy}^0 \end{bmatrix} + \begin{bmatrix} B_{11} & B_{12} & B_{16} \\ B_{21} & B_{22} & B_{26} \\ B_{16} & B_{26} & B_{66} \end{bmatrix} \begin{bmatrix} \kappa_x^0 \\ \kappa_y^0 \\ \kappa_{xy}^0 \end{bmatrix}, \\ \begin{bmatrix} M_x \\ M_y \\ M_{xy} \end{bmatrix} &= \begin{bmatrix} B_{11} & B_{12} & B_{16} \\ B_{21} & B_{22} & B_{26} \\ B_{16} & B_{26} & B_{66} \end{bmatrix} \begin{bmatrix} \epsilon_x^0 \\ \epsilon_y^0 \\ \gamma_{xy}^0 \end{bmatrix} + \begin{bmatrix} D_{11} & D_{12} & D_{16} \\ D_{21} & D_{22} & D_{26} \\ D_{16} & D_{26} & D_{66} \end{bmatrix} \begin{bmatrix} \kappa_x^0 \\ \kappa_y^0 \\ \kappa_{xy}^0 \end{bmatrix} \end{aligned} \quad (3)$$

where  $A_{ij}, B_{ij}, D_{ij}$  are the extensional stiffness coefficients, the coupling stiffness coefficients, and the bending stiffness coefficients, respectively. These matrices are obtained from Equation (4):

$$(A_{ij}, B_{ij}, D_{ij}) = \int_{-t/2}^{t/2} [\bar{Q}_{ij}(1, z_i, z_i^2)] dz_i \quad (4)$$

where  $\bar{Q}_{ij}$  is transformed reduced stiffnesses, and  $z_i$  and  $t$  are the coordinates in the  $z$ -direction and the thickness of the tow, respectively. Since the prepreg is an orthotropic material, the matrix  $[B]$  is zero, and  $D_{16}, D_{26} = 0$ . By direct substitution of the moment and results from Equation (3) into Equation (2), the governing equation of a unidirectional

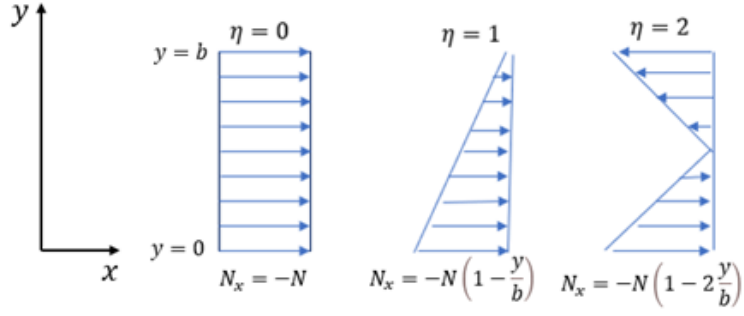


Figure 3.6: The stress distribution for different values of  $\eta$ .

prepreg tape resting on the Pasternak elastic foundation can be obtained by the following equation [Nazarimofrad and Barkhordar \(2016\)](#); [J. N. Reddy \(2003\)](#).

$$\left[ D_{11} \frac{\partial^4 w}{\partial x^4} + 2(D_{12} + D_{66}) \frac{\partial^4 w}{\partial x^2 \partial y^2} + D_{22} \frac{\partial^4 w}{\partial y^4} \right] - N_x \frac{\partial^2 w}{\partial x^2} + K_f w - G \left( \frac{\partial^2 w}{\partial x^2} + \frac{\partial^2 w}{\partial y^2} \right) = 0 \quad (5)$$

where  $k$ ,  $G$  are spring constants of Pasternak model, and according to the physics of the problem,  $N_x$  is a linearly varying in-plane load that can be defined by:

$$N_x = -N_1 - \frac{\eta y}{b} \quad (6)$$

where  $b$  is the width of the tow, and  $\eta$  is a constant between 0 and 2, for example,  $\eta = 0$  and  $\eta = 2$  correspond to uniform compressive load and pure bending load, respectively. Figure 3.6 demonstrates the in-plane load distribution for various values of  $\eta$ .

### 3.4.2 Initial Defect

There are two primary types of imperfections that may occur: interfacial imperfections and initial geometric defects. In this context, the interfacial imperfection is modeled by using a Pasternak elastic foundation which is presented in Equation 1. Initial geometric imperfections, on the other hand, may result from slight pre-existing deformations in the prepreg during its production, minor substrate defects, or misalignments in the AFP guidance system. These imperfections are modeled using the Koiter model, which represents

them as a small fraction of the shape modes employed to solve the buckling equation. The initial imperfection is formulated in Equation 7, where  $w^*(x, y)$  represents the initial defect. [Mirzavand and Eslami \(2006\)](#); [Shariat, Javaheri, and Eslami \(2005\)](#).

$$W^*(x, y) = \mu h w \quad (7)$$

where  $\mu h$  represents the amplitude of the initial defect (imperfection), and ( $0 \leq \mu \leq 1$ ) when the  $\mu = 0$ , it expresses a perfect lamina. To consider the initial defects, the vertical displacement  $w$  in Equation (5) needs to be replaced by  $w + w^*$ . It should be noticed that the expression in the bracket in Equation (5) remains constant for the reason that this expression resulted from the bending moments. The bending moments are only related to the curvature of the plate, and they remain unchanged by changing the total curvature. As a result, Equation (5) yields:

$$\begin{aligned} D_{11} \frac{\partial^4 w}{\partial x^4} + 2(D_{12} + D_{66}) \frac{\partial^4 w}{\partial x^2 \partial y^2} + D_{22} \frac{\partial^4 w}{\partial y^4} - N_x w_{xx} + w_{xx}^* + K_f(w + w^*) \\ - G(w_{xx} + w_{xx}^* + w_{yy} + w_{yy}^*) = 0 \end{aligned} \quad (8)$$

To obtain the values of wavelength or critical force of wrinkle formation, one needs to solve Equation (8).

### 3.4.3 Solution Procedure

To solve the PDE, Equation (8), since the edges loaded are clamped, the solution can be presented in the form:

$$w(x, y) = w_m(y) \left( 1 - \cos\left(\frac{2m\pi x}{a}\right) \right) \quad (9)$$

where  $1 - \cos\left(\frac{2m\pi x}{a}\right)$  satisfies the boundary condition at  $x = 0, a$ . By definition of initial defects based on the Koiter model, the  $w^*(x, y)$  can be expressed as:

$$w^*(x, y) = \mu h w_m(y) \left( 1 - \cos\left(\frac{2m\pi x}{a}\right) \right) \quad (10)$$

Substituting  $w(x,y)$  and  $w^*(x,y)$  into Equation (8) and after rearrangements, the following equation can be deduced:

$$\begin{aligned}
R_1 = & D_{22} \left( 1 - \cos \left( \frac{2m\pi x}{a} \right) \right) \frac{d^4 w_m(y)}{dy^4} \\
& + 2(D_{12} + D_{66}) \frac{4\pi^2 m^2}{a^2} \frac{d^2 w_m(y)}{dy^2} \cos \left( \frac{2m\pi x}{a} \right) \\
& - G(1 + \mu h) \frac{d^2 w_m(y)}{dy^2} \left( 1 - \cos \left( \frac{2m\pi x}{a} \right) \right) \\
& - D_{11} \frac{16\pi^4 m^4}{a^4} \cos \left( \frac{2m\pi x}{a} \right) w_m(y) \\
& - N_x \frac{4\pi^2 m^2}{a^2} (1 + \mu h) w_m(y) \cos \left( \frac{2m\pi x}{a} \right) \\
& + K_f (1 + \mu h) w_m(y) \left( 1 - \cos \left( \frac{2m\pi x}{a} \right) \right) \\
& - G \frac{4\pi^2 m^2}{a^2} (1 + \mu h) \cos \left( \frac{2m\pi x}{a} \right) w_m(y)
\end{aligned} \tag{11}$$

By direct substitution of  $N_x = -N_1 - \eta y b$  into Equation (11), it leads to a nonlinear and non-homogeneous ordinary differential equation. To solve for Equation (11), we first transform it from a non-homogeneous to a homogeneous equation using the Galerkin method. To reach a homogeneous equation, Equation (11) should be multiplied by an admissible function satisfying the boundary condition. The following function satisfies the conditions of the Galerkin method:

$$\psi = 1 - \cos \left( \frac{2n\pi x}{a} \right) \tag{12}$$

According to the Galerkin method:

$$\int_0^a R_1 \times \psi dx = 0 \tag{13}$$

In the calculation of the above integrals, two integrals appear which can be solved as follows:

$$\int_0^a \left(1 - \cos\left(\frac{2m\pi x}{a}\right)\right) \left(1 - \cos\left(\frac{2n\pi x}{a}\right)\right) dx = \frac{3}{2}a, \quad \text{for } m = n \quad (14)$$

$$\int_0^a \cos\left(\frac{2m\pi x}{a}\right) \left(1 - \cos\left(\frac{2n\pi x}{a}\right)\right) dx = -\frac{1}{2}a, \quad \text{for } m = n \quad (15)$$

By employing the Galerkin method, the non-homogenous Equation (11) transform the homogenous one, which after rearrangements, can be written as:

$$\begin{aligned} D_{22} \frac{d^4 w_m(y)}{dy^4} - 2(D_{12} + D_{66}) \frac{4\pi^2 m^2}{a^2} \frac{d^2 w_m(y)}{dy^2} + G(1 + \mu h) \frac{d^2 w_m(y)}{dy^2} + D_{11} \frac{16\pi^4 m^4}{a^4} w_m(y) \\ - N_x \frac{4\pi^2 m^2}{a^2} (1 + \mu h) w_m(y) + K_f (1 + \mu h) w_m(y) - G \frac{4\pi^2 m^2}{a^2} (1 + \mu h) w_m(y) = 0 \end{aligned} \quad (16)$$

Now, as mentioned in the problem definition, the boundary conditions of unloaded edges can be considered S.S. according to the physics of the problem. The boundary condition equations for S.S are presented as:

$$\begin{aligned} w &= 0 \\ M_{yy} &= D_{12} \frac{d^2 w}{dx^2} + D_{22} \frac{d^2 w}{dy^2} = 0 \end{aligned} \quad (17)$$

To write the boundary conditions in the form of  $w(y)$ , we substitute  $w$  from Equation (9) into Equation (17); the simply supported (S.S) equations result in:

$$\begin{aligned} w &= 0 \\ M_{yy} &= D_{12} \frac{4\pi^2 m^2}{a^2} w(y) \cos\left(\frac{2m\pi x}{a}\right) + D_{22} \frac{d^2 w}{dy^2} \left(1 - \cos\left(\frac{2m\pi x}{a}\right)\right) \approx 0 \end{aligned} \quad (18)$$

Applying the Galerkin method to the Equation (18), the boundary conditions lead to:

$$\begin{aligned} w &= 0 \\ M_{yy} &= D_{22} \frac{d^2 w(y)}{dy^2} - \frac{4\pi^2 m^2}{3a^2} D_{12} w(y) = 0 \end{aligned} \quad (19)$$

To solve the nonlinear homogenous ordinary Equation (16), The finite difference method

(FDM) was employed Lopatin and Morozov (2009). In this method, first, the interval between  $y=0$  and  $y=b$  is partitioned into  $n$  subintervals. Then, the differential operators are approximated by the differential quotients. Based on the FD method, differential operators can be expressed in the following forms:

$$\begin{aligned}
\frac{dw}{dy}_i &= \frac{1}{2s}(-w_{i-1} + w_{i+1}) \\
\frac{d^2w}{dy^2}_i &= \frac{1}{s^2}(w_{i-1} - 2w_i + w_{i+1}) \\
\frac{d^3w}{dy^3}_i &= \frac{1}{2s^3}(-w_{i-2} + 2w_{i-1} - 2w_{i+1} + w_{i+2}) \\
\frac{d^4w}{dy^4}_i &= \frac{1}{s^4}(w_{i-2} - 4w_{i-1} + 6w_i - 4w_{i+1} + w_{i+2})
\end{aligned} \tag{20}$$

where  $i$  is the node number,  $w_i$  represents the deflection component in  $z$ -direction for the  $i$ th node, and  $s = b/n$  is the distance between the two nodes. Figure 3.7 shows the sections in the  $y$ -direction. According to Figure 3.7, the coordinates of the nodes in the  $y$ -direction can be written as:

$$y_i = s(i - 1) \tag{21}$$

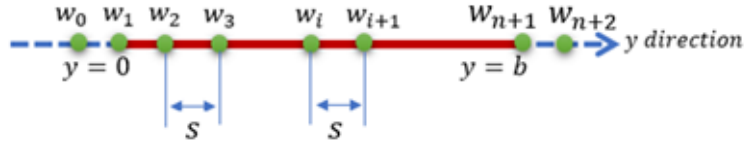


Figure 3.7: Staggered grid and nodes in the  $y$ -direction.

By replacing Equations (20) and (21) into Equation (16), and after rearrangements, the nonlinear equation can be written as:

$$X_1w_i - X_2Z_i + X_3U_i - X_4F_iw_i = 0 \tag{22}$$

where

$$\begin{aligned}
X_1 &= D_{11} \frac{16\pi^4 m^4}{3a^4} + K_f(1 + \mu h) + G \frac{4\pi^2 m^2}{a^2} (1 + \mu h) \\
X_2 &= G(1 + \mu h) + 2(D_{12} + D_{66}) \frac{4\pi^2 m^2}{a^2} \frac{1}{s^2} \\
X_3 &= D_{22} \frac{1}{s^4} \\
X_4 &= N \frac{4\pi^2 m^2}{a^2} (1 + \mu h) \\
Z_i &= (w_{i-1} - 2w_i + w_{i+1}), \\
U_i &= w_{i-2} - 4w_{i-1} + 6w_i - 4w_{i+1} + w_{i+2}, \\
F_i &= \left(1 - \frac{\eta(i-1)}{n}\right)
\end{aligned} \tag{23}$$

As it can be seen in Figure 3.7, there are two nodes named  $w_0, w_{(n+2)}$  which are out of the trivial difference between  $y = 0$  and  $y = b$ . These nodes are defined by boundary conditions at  $y = 0, b$ . Replacing  $w_1$  into the boundary condition equations at  $y = 0$  leads to:

$$\begin{aligned}
w = 0 &\implies w_1 = 0 \\
D_{22} \frac{d^2 w(y)}{dy^2} - \frac{4\pi^2 m^2}{3a^2} D_{12} w(y) = 0 &\implies \\
- D_{12} \frac{4\pi^2 m^2}{3a^2} w_1 + D_{22} \frac{1}{s^2} (w_0 - 2w_1 + w_2) = 0 &\xrightarrow{w_1=0} w_0 = -w_2
\end{aligned} \tag{24}$$

Again, the substitution of  $w_{n+1}$  into the boundary condition equation at  $y = b$  leads to:

$$\begin{aligned}
w = 0 &\implies w_{n+1} = 0 \\
D_{22} \frac{d^2 w(y)}{dy^2} - \frac{4\pi^2 m^2}{3a^2} D_{12} w(y) = 0 &\implies \\
- D_{12} \frac{4\pi^2 m^2}{3a^2} w_1 + D_{22} \frac{1}{s^2} (w_n - 2w_{n+1} + w_{n+2}) = 0 &\xrightarrow{w_{n+1}=0} w_{n+2} = -w_n
\end{aligned} \tag{25}$$

With regard to the simply supported conditions,  $w_{(n+1)}$  and  $w_1$  are zero. Therefore, Equation (22) for each node can be obtained. By substitution of  $w_i$  for  $(i=2, \dots, n)$  into Equation (22), we have a linear system of  $n-1$  equations for the  $n-1$  unknowns  $[w_2, w_3, \dots, w_n]$ . This equation system can be written in matrix form:

$$\begin{aligned}
& X_1 \begin{bmatrix} 1 & 0 & \dots & 0 \\ 0 & 1 & \dots & 0 \\ 0 & 0 & \dots & 0 \\ \vdots & \vdots & \ddots & \vdots \\ 0 & 0 & \dots & 0 \\ 0 & 0 & \dots & 1 \end{bmatrix}_{n-1 \times n-1} \quad -X_2 \begin{bmatrix} -2 & 1 & 0 & 0 & \vdots & 0 & 0 & 0 \\ 1 & -2 & 1 & 0 & \vdots & 0 & 0 & 0 \\ 0 & 1 & -2 & 1 & \vdots & 0 & 0 & 0 \\ \vdots & \vdots \\ 0 & 0 & 0 & 0 & \vdots & 1 & -2 & 1 \\ 0 & 0 & 0 & 0 & \vdots & 0 & 1 & -2 \end{bmatrix}_{n-1 \times n-1} \\
& X_3 \begin{bmatrix} 5 & -4 & 1 & 0 & 0 & \vdots & 0 & 0 & 0 & 0 \\ -4 & 6 & -4 & 1 & 0 & \vdots & 0 & 0 & 0 & 0 \\ 1 & -4 & 6 & -4 & 1 & \vdots & 0 & 0 & 0 & 0 \\ \vdots & \vdots \\ 0 & 0 & 0 & 0 & 0 & \vdots & 1 & -4 & 6 & -4 \\ 0 & 0 & 0 & 0 & 0 & \vdots & 0 & 1 & -4 & 5 \end{bmatrix} \\
& -X_4 \begin{bmatrix} 1 & 0 & \dots & 0 \\ 0 & 1-\eta/n & \dots & 0 \\ 0 & 0 & \dots & 0 \\ \vdots & \vdots & \ddots & \vdots \\ 0 & 0 & \dots & 0 \\ 0 & 0 & \dots & 1-\eta(n-1)/n \end{bmatrix}_{n-1 \times n-1} \begin{bmatrix} w2 \\ w3 \\ w4 \\ \vdots \\ w5 \\ w6 \end{bmatrix} = 0
\end{aligned} \tag{26}$$

To have a non-trivial solution for the above system of equations, the determinant of the matrix expression in the bracket is to be equal to zero. This determinant is an expression for  $a$  (wrinkle wavelength) and  $N$  (critical buckling load).

### 3.4.4 Relation between Critical Steering Radius and Critical Load

Owing to the unbalanced length during the steering process, a linearly varying in-plane load is generated in tow.

This load is shown in Figure 3.4. To find a relation between steering radius and the

applied load, the bending moment and curvature equation can be employed. Figure 3.8 shows the tape under a bending load. The bending moment and curvature are linked to each other by the following equation.

$$R = \frac{E_1 I}{M_0} \quad (27)$$

where  $E_1$  is Young's modulus in the fiber direction,  $I$  is the moment of inertia for the tow,  $R$  is the steering radius, and  $M_0$  is the moment about point O (see Figure 3.8).

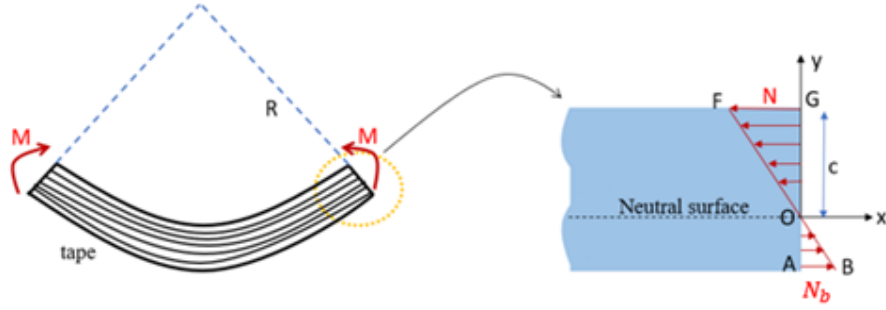


Figure 3.8: A schematic diagram of a steered tow under the bending load generated by the roller.

Regarding Figure 3.8, the value of  $c$  is equal to  $\frac{b}{\eta}$ , and from the similarity of the two triangles  $\triangle AOB$  and  $\triangle FOG$ , the value of  $N_b$  (the tensile force at the outer edge) can be found:

$$\triangle FTO \sim \triangle AOB \implies \frac{N}{N_b} = \frac{b}{\eta b} \implies N_b = N(\eta - 1) \quad (28)$$

As a result, the value of the moment about the natural axis (point O) yields:

$$M_o = \frac{N_b}{2} \frac{3}{\eta^2} + \frac{N_b}{2} \frac{(\eta - 1)}{3\eta^2} \quad (29)$$

The moment of inertia of the cross-section with respect to the x-axis is obtained from the equation:

$$I = tb^3 \left( \frac{1}{12} + \left( \frac{1}{2} - \frac{1}{\eta^2} \right)^2 \right) \quad (30)$$

where  $t$  and  $b$  represent the thickness and width of the tape, respectively. Substituting

Equations for  $M_o$  and  $I$  into the previous equation, we get:

$$R = \frac{E_1 I}{M_o} = \frac{E_1 t b \left( \frac{1}{12} + \left( \frac{1}{2} - \frac{1}{\eta^2} \right)^2 \right)}{N \left( \frac{1}{3\eta^2} + \frac{(\eta-1)^3}{3\eta^2} \right)} \quad (31)$$

Thus, if the maximum induced load  $N$  obtained from this equation for various values of the steering radius is more than the buckling load (obtained from the buckling equation), the wrinkle will occur in the tow. In contrast, the tows will be wrinkle-free if the induced load is less than the buckling load (Equation (26)).

## 3.5 Result and Discussion

### 3.5.1 Numerical Results Obtained from Wrinkle Model

For the calculations, the mechanical properties of prepreg used in this paper were measured in a previous paper published by Bakhshi and Hojjati [Bakhshi and Hojjati \(2019\)](#). Table 3.5.1 indicates these mechanical properties.

$E_1$ (GPa)	$E_2$ (MPa)	$G_{12}$ (MPa)	$\eta$	$\nu_{12}$	t(mm)	b(mm)
31	0.046	3.025	2	0.2	0.2	6.35

Another important point to be mentioned is that since the wrinkle forms in tow as the first buckling load, the value of  $m$  in Equations (9) and (10) should be one.

### The Effect of Initial Defect on Critical Load and Steering Radius

As mentioned before, the initial geometric defect (imperfection) is introduced as a slight deviation of the midplane from a flat one. The impact of increasing the initial defect on buckling load and steering radius is presented in Figures 9 and 10. The values of spring constants assume to be  $k = 3.25 \times 10^8$  N/m and  $G = 605$  N/m according to [Bakhshi and Hojjati \(2019\)](#); [Belhaj and Hojjati \(2018\)](#) in the mathematical wrinkle model. As can be seen, a rise in initial defect is associated with a small reduction in critical load, which, according to Equation (31), implies an increase in minimum steering radius. In Figures 3.9

and 3.10, the value of  $h$  is assumed to be one.

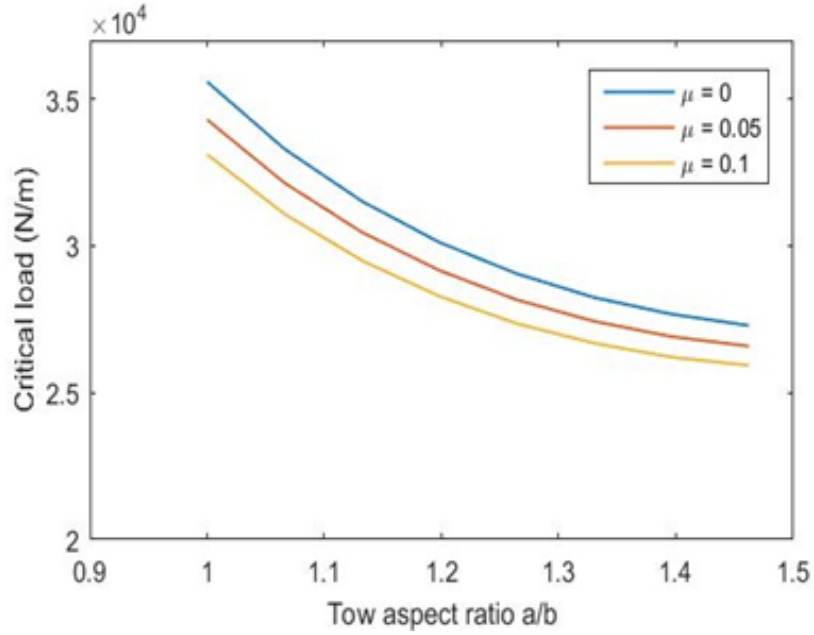


Figure 3.9: The variations of critical load versus different plate aspect ratios for various initial defect coefficients.

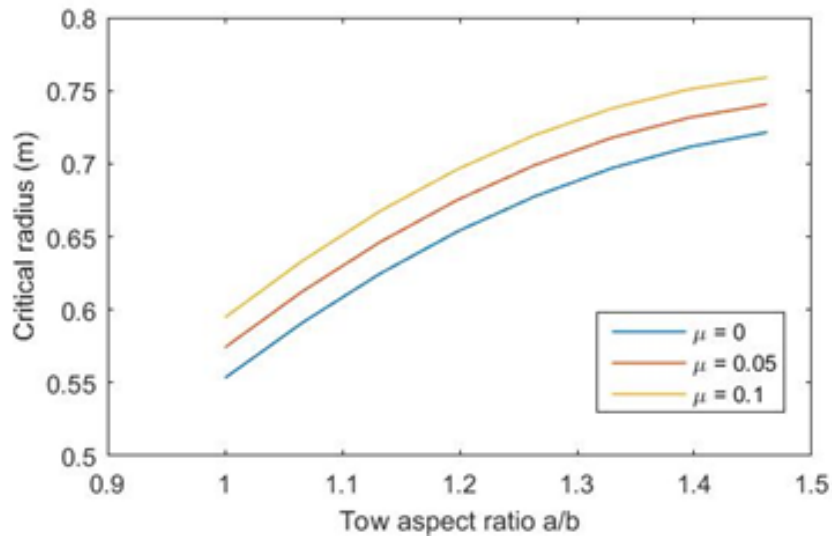


Figure 3.10: The variations of critical radius versus different plate aspect ratios and initial defect coefficients.

### The Effects of Tack Stiffness (Spring Constant of the Pasternak Model) and Initial defect (Imperfection) of the Tape on the Minimum Steering Radius

The variations of steering radius and buckling load with stiffness parameter of Pasternak foundation model for a tow with different initial defects are displayed in Figures 11 and 12, respectively. The most important observations are as follows. As the stiffness parameter increases, the critical radius declines, and the buckling load increases. This can be explained by the fact that increasing the stiffness ( $K_f$ ) means a stronger tack. Thus, to overcome the tack of prepreg, the axial in-plane load applied to the prepreg plate should be increased.

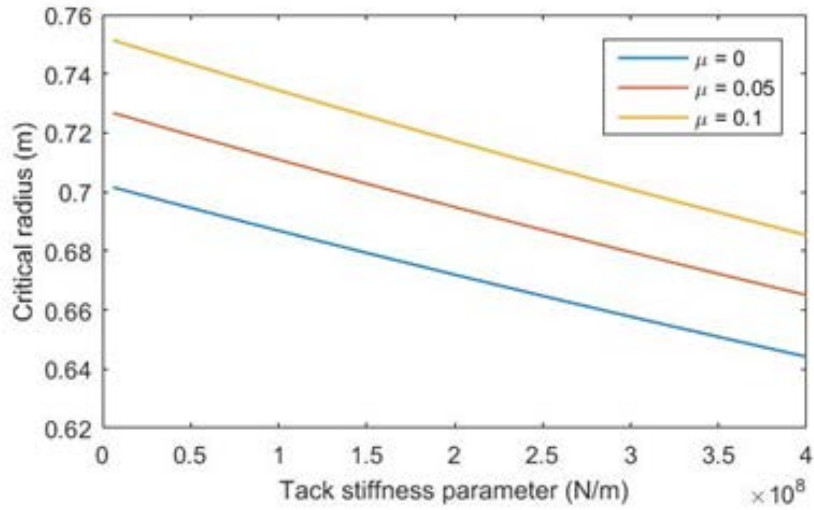


Figure 3.11: Critical radius steering variations with respect to tack stiffness parameter for different initial defect coefficients.

In contrast, according to Equation (30), the steering radius has an inverse relation with the buckling load. As a result, an increasing in-plane load leads to a decrease in radius steering. Besides, a rise in the value of the initial defect of the tow based on the Koiter model leads to a slight growth in critical steering radius and a slight reduction in buckling load. In Figures 3.11 and 3.12, the value of the aspect ratio for the tow is assumed to be 1.5.

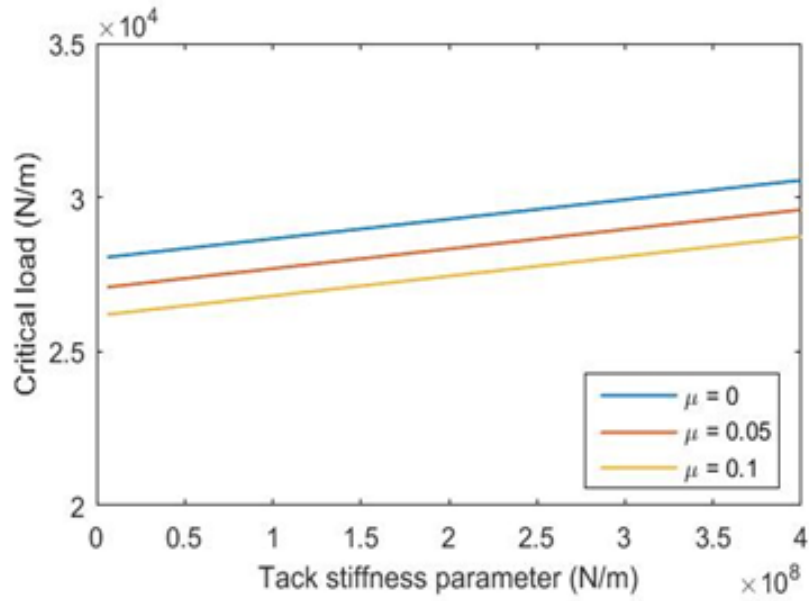


Figure 3.12: Critical buckling load variations with respect to tack stiffness parameter for different initial defect coefficients.

### 3.5.2 Drawing a Comparison between Wrinkle Wavelengths Obtained from the Theoretical Model and Experimental Work

To validate the theoretical model with experiment results, in this section, a comparison is made between the values of the wrinkle wavelengths calculated from the theoretical wrinkle model and the experimental findings. For this reason, the value of maximum load from Equation (30) as a function of critical radius is replaced into Equation (25) instead of  $N$ . By solving the determinant of Equation (25) for wrinkle wavelength ( $L$ ), the value of wavelength is found for each critical radius. Figure 13 shows steering radius versus wrinkle wavelength for both experimental and theoretical results. The values of spring constants assume to be  $k = 3.25 \times 10^8 \text{ N/m}$  and  $G = 605 \text{ N/m}$  according to [Bakhshi and Hojjati \(2019\)](#); [Belhaj and Hojjati \(2018\)](#) in the mathematical wrinkle model.

As can be seen, the results yielded from the proposed model are in good agreement with experiment results. Also, it is found that considering the effect of a slight defect (imperfection) with an initial defect coefficient of  $\mu=0.05$  leads to a better agreement between the proposed model and experiment results.

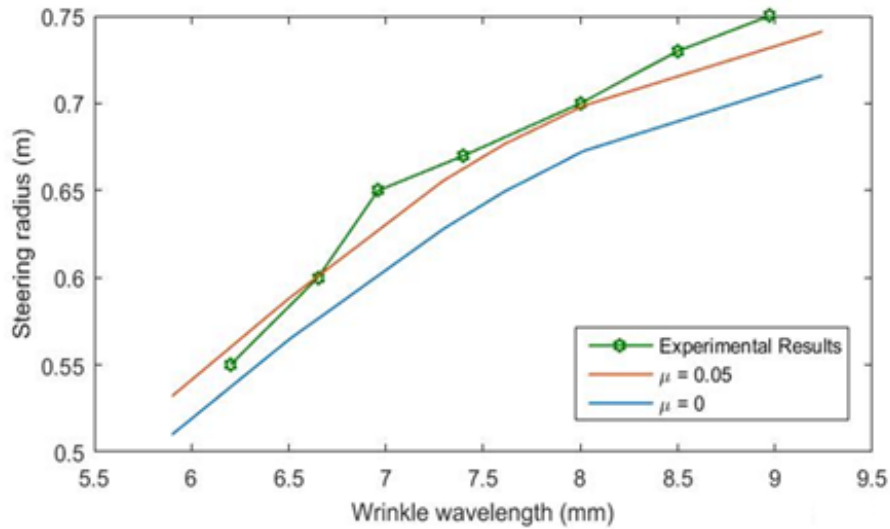


Figure 3.13: Wrinkle wavelength of the tape versus different steering radius.

### 3.6 Conclusions

This study is concerned with the wrinkle formation during steering with an initial defect based on the Koiter model. A theoretical buckling model is presented to model the wrinkle formation of the prepreg tape resting on an elastic foundation. Pasternak model is adopted to model tack properties. The Galerkin method along with the finite difference method are employed to solve the problem for critical buckling load and steering radius. The solution method presented in this study can completely satisfy the different boundary conditions of the problem. The obtained results reveal that an increasing initial defect is associated with an overall reduction in buckling load, and consequently, the smaller critical loads occur for higher critical radius steering values. Any improvement in tack (elastic foundation) properties significantly affects the numerical values of the critical load and radius. Specifically, growth in foundation stiffness results in a notable reduction in the critical radius, which subsequently leads to increasing the load. Finally, the results for wrinkle wavelengths yielded from the applied model are compared to those of experimental work. It is worth noting that the diagrams showed that the model predictions are very close to the results measured from experimental work.

## Chapter 4

# Exact three-dimensional elasticity analysis for buckling of composite laminated plates resting on viscoelastic foundation

This work has been published in:

Kheradpisheh, Meisam, and Mehdi Hojjati. "Exact three-dimensional elasticity analysis for buckling of composite laminated plates resting on viscoelastic foundation." *Thin-Walled Structures* (2024): 112060.

### 4.1 Abstract

This paper aims to present novel exact solutions for the buckling of a laminated plate resting on the viscoelastic foundation with both normal and shear viscoelastic layers. The governing equations of plate buckling are derived using three-dimensional elasticity theory and state-space formulation. The normal and shear layers of the viscoelastic foundations

are modeled using the generalized Maxwell model to represent both the elastic and viscoelastic properties of the foundation. To couple the viscoelastic foundation equation with the buckling equation, Boltzmann's superposition principle along with the Laplace transform is utilized. Then, the effects of geometry, relaxation modulus of normal and shear layers, viscosity, and time are investigated on the buckling load. The results reveal that the higher viscosity coefficient leads to a slower rate of change in the buckling loads. In addition, the viscoelastic properties have a significant impact on the buckling behavior of the plate. In this regard, the results show that instead of the expected second mode at a constant aspect ratio, the plate experiences the first mode as time passes. The computed results also show that there is a critical threshold. When the foundation stiffness exceeds this threshold, the conventional method of reducing the aspect ratio to prevent buckling not only proves ineffective in reducing the probability of buckling but also, in fact, leads to an increase in buckling occurrences. In addition to the analytical investigation, a finite element (FE) analysis is carried out to study the buckling response of the composite plate. The finite element results also show a reasonably good agreement with those of the analytical method.

## 4.2 Introduction

Composite materials such as Carbon fiber reinforced polymer (CFRP) and Glass fiber reinforced polymer (GERP) have been widely used in a variety of industry structures thanks to their high strength-to-weight ratio, and excellent specific mechanical and chemical resistance. Such structures experience severe loading conditions both during the manufacturing process and in the place of their use in the industry. During the manufacturing process, including the automated fiber placement (AFP) and autoclave processes, the composite parts are subjected to various pressure, and in industry applications, these structures are subjected to significant loading such as aerodynamic pressure and thermal loads, e.g. [Y. Hu, Han, Cheng, and Hu \(2023\)](#); [Jing and Duan \(2022\)](#).

The growing demand and diverse operating conditions have resulted in a rich body of literature focused on the mechanical behavior of composite materials in various situations.

Notably, buckling, as a catastrophic failure mode, has consistently received great attention from researchers [Alimirzaei, Najafabadi, and Khodaei \(2022\)](#); [Han, Cheng, Lu, Li, and Lu \(2016\)](#); [Sayyad and Ghugal \(2017\)](#). Early research into this field goes back to [J. Reddy and Khdeir \(1989\)](#); [J. N. Reddy \(2003\)](#) works which are according to existing theories such as the classical laminate theory (CLT) and the first and higher order shear deformation theories (FSDT, HSDT). However, a limitation of these theories is that they neglect or simplify the consideration of transverse stresses. Therefore, exact solution theories such as the three-dimensional theory of elasticity (3D elasticity theory) and state-space method were employed to investigate the mechanical behavior of the structures under various loading [Bakhtiari and Kheradpisheh \(2020\)](#); [Chen, Lee, and Ding \(2005\)](#); [Kim and Lee \(2008\)](#). The author in the work [Chen et al. \(2005\)](#), employed 3D elasticity theory to investigate an exact solution for the vibration response of a non-homogeneous plate. The work in [Kim and Lee \(2008\)](#) investigated the buckling of a piezoelectric plate. They used 3D elasticity theory along with the state-space method to find the exact solution for a piezoelectric plate with an imperfect interface. An analytical solution for the buckling of doubly curved composites using the state-space method was performed in [Juhász and Szekrényes \(2020\)](#). The work in [D. Liu, Kitipornchai, Chen, and Yang \(2018\)](#) investigated the mechanical behavior of a functionally graded graphene composite cylinder employing 3D elasticity theory.

Structures supported by elastic and viscoelastic foundations have been a subject of interest among researchers due to their importance in modeling different mechanical problems. These foundations are utilized in industry to prevent mechanical failures in structures [Bagherizadeh, Kiani, and Eslami \(2011\)](#); [Huang, Lü, and Chen \(2008\)](#); [Zenkour and Alghanmi \(2022\)](#). There are various models to describe the interactions between plate and viscoelastic and elastic foundations, as can be found in the informative work by [Younesian, Hosseinkhani, Askari, and Esmailzadeh \(2019\)](#). For the first time, Winkler introduced a straightforward model to explain the concept of an elastic foundation. This model employs a system of springs to define the interaction between a beam and its underlying foundation [Dillard, Mukherjee, Karnal, Batra, and Frechette \(2018\)](#); [Kerr \(1964\)](#). However, it was recognized that the Winkler model had limitations in capturing all the properties exhibited

by different types of foundations. Thus, alternative models like the Pasternak model were introduced, which consider shear interactions to provide a more comprehensive characterization of elastic foundations [Esen \(2019\)](#); [Hadji, Avcar, and Zouatnia \(2022\)](#). The work in [Zenkour and Alghanmi \(2022\)](#) studied the bending behavior of the FG porous sandwich plate resting on Pasternak's elastic foundation. They used a quasi-3D theory along with a novel form for describing the porosity distribution to derive the related equations. The mechanical response of a FG plate resting subjected to the elastic Pasternak foundation is presented in [Huang et al. \(2008\)](#). Solutions for the thermal and mechanical buckling of a cylindrical shell surrounded by a Pasternak elastic foundation can be found in [Shen, Xiang, and Lin \(2017\)](#) and [Kiani et al. \(2012\)](#). They used the higher-order shear deformation theory to find a solution for the buckling problem. The authors in [Belhaj and Hojjati \(2018\)](#) studied the wrinkle formation in viscoelastic tape as a buckling problem. They modeled the foundation as an elastic Pasternak foundation.

On the other hand, in many applications particularly when dealing with composite materials, the foundations are viscoelastic materials like the adhesive nature of resins [Budelmann et al. \(2020\)](#); [Kheradpisheh and Hojjati \(2023\)](#). As a result, foundation models have been developed by incorporating viscose elements. In [Kheradpisheh and Hojjati \(2023\)](#), the authors modeled wrinkle formation at prepreg tape as a fiber-buckling formation on the viscoelastic foundation. The work in [Askarian, Permoon, and Shakouri \(2020\)](#) studied the stability of a fluid-conveying pipe on a fractional Kelvin-Voigt viscoelastic foundation. They employed a fractional model along with the Laplace method to solve the governing equations. In [Muscolino and Palmeri \(2007\)](#), the vibration equation of a beam on a viscoelastic foundation under a moving load was solved. The work in [Kiasat, Zamani, and Aghdam \(2014\)](#) investigated the free vibration of viscoelastic plates resting on Kelvin-Voigt viscoelastic foundations. They used Euler-Bernoulli and Kirchhoff-Love theories to approximately derive the equation of motion. The authors in [Zaitoun et al. \(2022\)](#) studied the buckling response of a FGM plate simply supported on the viscoelastic foundation using the higher-order shear deformation. The vibration behavior of the laminated plate on the normal layer of the viscoelastic foundation is presented by [Zenkour and El-Shahrany \(2021\)](#). The authors

in [Hebali et al. \(2022\)](#) used the higher order shear deformation theory to find the bending behavior of FG plate on the viscoelastic foundation.

Although the prior studies have investigated the buckling response of plates on elastic foundations, a few studies have been focused on viscoelastic foundations and it appears that the exact solutions of buckling load for a plate subjected to a viscoelastic foundation have not been carried out thus far. Accordingly, the primary purpose of this study is to provide exact 3D solutions for the buckling of a plate resting on both normal and shear viscoelastic foundations. The present work considers two generalized Maxwell models to describe the shear and normal viscoelastic layers of the foundation. In addition, Boltzmann's principle along with the Laplace transform is employed for coupling the foundation equation to the buckling problem. The method used in this paper reduces the complexity of buckling analysis of the structures on the viscoelastic foundation. In this approach, the viscoelastic foundation equations and plate equation are driven independently and subsequently, these individual equations are coupled to yield exact solutions for the buckling response. The present analyses are firstly validated by comparing computed results to those obtained by classical laminate theory. Then, The effects of viscoelastic and geometry parameters on buckling response are thoroughly examined and discussed.

### 4.3 Analytical procedure

Consider a rectangular laminated plate with dimensions of the length of  $a$ , width  $b$ , and thickness  $h$  resting on a visco-elastic foundation as visually depicted in [Fig. 4.1](#). A generalized Maxwell model is used to model both the viscoelastic normal layer and the viscoelastic shear layer.

The stress-strain relationships for each orthotropic ply are represented by the generalized

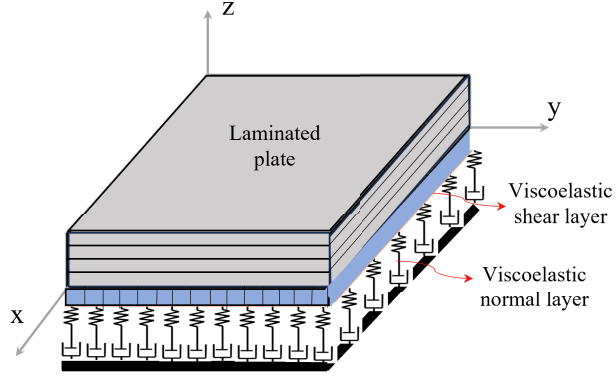


Figure 4.1: Schematic of a laminated plate resting on Maxwell viscoelastic foundation.

Hooke's law [Hyer and White \(2009\)](#):

$$\begin{bmatrix} \sigma_x \\ \sigma_y \\ \sigma_z \\ \tau_{yz} \\ \tau_{xz} \\ \tau_{xy} \end{bmatrix}_{(i)} = \begin{bmatrix} C_{11} & C_{12} & C_{13} & 0 & 0 & 0 \\ C_{21} & C_{22} & C_{23} & 0 & 0 & 0 \\ C_{31} & C_{32} & C_{33} & 0 & 0 & 0 \\ 0 & 0 & 0 & C_{44} & 0 & 0 \\ 0 & 0 & 0 & 0 & C_{55} & 0 \\ 0 & 0 & 0 & 0 & 0 & C_{66} \end{bmatrix} \begin{bmatrix} \varepsilon_x \\ \varepsilon_y \\ \varepsilon_z \\ \gamma_{yz} \\ \gamma_{xz} \\ \gamma_{xy} \end{bmatrix}_{(i)} \quad (32)$$

where (i) represents the number of ply in the laminated plate, and  $C_{ij}$  are the components of the stiffness matrix, which can be defined by Young's modulus and Poisson's ratio [Hyer and White \(2009\)](#). Moreover, the strain displacement relationships in the three dimensions are expressed as [Hyer and White \(2009\)](#):

$$\begin{aligned} \varepsilon_x &= \frac{\partial u}{\partial x}, \quad \varepsilon_y = \frac{\partial v}{\partial x}, \quad \varepsilon_z = \frac{\partial w}{\partial x}, \quad \gamma_{yz} = \frac{\partial v}{\partial x} + \frac{\partial w}{\partial x}, \\ \gamma_{xy} &= \frac{\partial u}{\partial x} + \frac{\partial v}{\partial x}, \quad \gamma_{xz} = \frac{\partial u}{\partial x} + \frac{\partial w}{\partial x}, \end{aligned} \quad (33)$$

where  $u, v$ , and  $w$  are the three displacement components in  $x, y$ , and  $z$  direction. Besides, the equations of equilibrium in Cartesian coordinates are written as [Ding, Chen, and Zhang](#)

(2006):

$$\begin{aligned}
\frac{\partial \sigma_x}{\partial x} + \frac{\partial \tau_{xy}}{\partial y} + \frac{\partial \tau_{xz}}{\partial z} + Fu &= 0 \\
\frac{\partial \tau_{xy}}{\partial x} + \frac{\partial \sigma_y}{\partial y} + \frac{\partial \tau_{yz}}{\partial z} + Fv &= 0 \\
\frac{\partial \tau_{zx}}{\partial x} + \frac{\partial \tau_{yz}}{\partial y} + \frac{\partial \sigma_z}{\partial z} + Fw &= 0
\end{aligned} \tag{34}$$

where  $F = N_x \frac{\partial^2}{\partial x^2} + N_y \frac{\partial^2}{\partial y^2}$  in which  $N_x$ , and  $N_y$  represent the in plane load applied to the composite plate in x and y directions, respectively. By substitution of Eq.(33) and Eq.(32) into Eq.(34) and rearranging the equation according to the state-space method [Ding et al. \(2006\)](#), the following state equation for the buckling of  $i$ th layer is obtained:

$$\frac{\partial}{\partial z} \begin{bmatrix} \sigma_z \\ u \\ v \\ w \\ \tau_{xz} \\ \tau_{yz} \end{bmatrix}_{(i)} = \begin{bmatrix} [0]_{3 \times 3} & [M_2]_{3 \times 3} \\ [M_3]_{3 \times 3} & [0]_{3 \times 3} \end{bmatrix}_{(i)} \begin{bmatrix} \sigma_z \\ u \\ v \\ w \\ \tau_{xz} \\ \tau_{yz} \end{bmatrix}_{(i)} \tag{35}$$

where  $[M_2]_{3 \times 3}$ , and  $[M_3]_{3 \times 3}$  components of the sixth order matrix are given in Appendix A.

For a plate with simply supported conditions at the four edges which its lower surface is assumed subjected to a Maxwell viscoelastic foundation (see Fig.4.1), the boundary condition can be specified as:

$$w = v = 0, \quad \sigma_x = 0 \quad \text{at } x = 0, a, \tag{36a}$$

$$w = v = 0, \quad \sigma_y = 0 \quad \text{at } y = 0, a. \tag{36b}$$

To satisfy the aforementioned boundary conditions, the description of displacements and

stresses can be written into infinite dual trigonometric series as:

$$\begin{bmatrix} \sigma_z \\ u \\ v \\ w \\ \tau_{xz} \\ \tau_{yz} \end{bmatrix} = \sum_{m=0}^{\infty} \sum_{n=0}^{\infty} \begin{bmatrix} \bar{\Psi}_z(z) \sin(m\pi x/a) \sin(n\pi y/b) \\ \bar{U}(z) \cos(m\pi x/a) \sin(n\pi y/b) \\ \bar{V}(z) \sin(m\pi x/a) \cos(n\pi y/b) \\ \bar{W}(z) \sin(m\pi x/a) \sin(n\pi y/b) \\ \bar{\Gamma}_{xz}(z) \cos(m\pi x/a) \sin(n\pi y/b) \\ \bar{\Gamma}_{yz}(z) \sin(m\pi x/a) \cos(n\pi y/b) \end{bmatrix} \quad (37)$$

where  $n$  and  $m$  are the half-wave numbers in the  $x$  and  $y$  directions, respectively, and. Subsequent substituting Eq. (37) into ordinary differential Eq. (35), we may derive the following equations for the  $i$ th layer:

$$\frac{dV^{(i)}(z)}{dz} = D_{mn}^{(i)} V^{(i)}(z) \quad (38)$$

where  $V^{(i)}(z) = [\bar{\Psi}_z(z), \bar{U}(z), \bar{V}(z), \bar{W}(z), \bar{\Gamma}_{xz}, \bar{\Gamma}_{yz}]^T$  is called the state vector for  $i$ th layer, and  $D_{mn}^{(i)}$  is a  $6 \times 6$  matrix for  $i$ th layer whose coefficients are defined as:

$$D_{mn}^{(i)} = \begin{bmatrix} [0]_{3 \times 3} & [D_2]_{3 \times 3} \\ [D_3]_{3 \times 3} & [0]_{3 \times 3} \end{bmatrix}_i$$

where

$$[D_2]_{3 \times 3} = \begin{bmatrix} \Omega & \mu_{ma} & \mu_{nb} \\ -\mu_{ma} & \frac{1}{C_{55}} & 0 \\ -\mu_{nb} & 0 & \frac{1}{C_{44}} \end{bmatrix}$$

$$[D_3]_{3 \times 3} = \begin{bmatrix} 1/C_{33} & -(C_{13}/C_{33})\mu_{ma} & -(C_{23}/C_{33})\mu_{nb} \\ (C_{13}/C_{33})\mu_{ma} & \beta_1 & (\alpha_2 + C_{66})\mu_{ma}\mu_{nb} \\ (C_{23}/C_{33})\mu_{nb} & (\alpha_2 + C_{66})\mu_{ma}\mu_{nb} & \beta_2 \end{bmatrix}$$

where

$$\begin{aligned}\Omega &= -(N_x \mu_{ma}^2 + N_y \mu_{nb}^2), \mu_{ma} = m\pi x/a, \mu_{nb} = n\pi y/b, \\ \alpha_1 &= C_{11} - \frac{C_{13}^2}{C_{33}}, \alpha_2 = C_{12} - \frac{C_{13}C_{23}}{C_{33}}, \alpha_3 = C_{22} - \frac{C_{23}^2}{C_{33}}, \\ \beta_1 &= \Omega + \alpha_1 \mu_{ma}^2 + C_{66} \mu_{nb}^2, \beta_2 = \Omega + C_{66} \mu_{ma}^2 + \alpha_3 \mu_{nb}^2.\end{aligned}$$

Given the small thickness of each individual ply, the components of matrix  $D_{mn}^{(i)}$  remain constant for each layer. Consequently, referring to the matrix theory as presented in the work [D. Liu et al. \(2018\)](#), the general solution for the first order matrix differential Eq. (38) is written in the following formula for each layer:

$$V^{(i)}(z_k) = \exp[D_{mn}^{(i)} h^{(i)}] V^{(i)}(z_{k-1}) \quad (39)$$

where  $h^{(i)}$  is the thickness of  $i$ th ply,  $V^{(i)}(z_k)$ , and  $V^{(i)}(z_{k-1})$  represent the state vector at the upper surface and bottom surface of each layer. Under the assumption of a perfect bond at the interface between the layers, the state vector of the upper surface in the  $i$ th layer is considered to be equal to that of the bottom surface in the  $i+1$ th layer ( $V^{(i)}(z_k) = V^{(i+1)}(z_{k-1})$ ). Therefore, the relationship between the state vectors of the outermost surface and the innermost surface of the laminated plate can be written as follows:

$$V^{(i)}(z = h) = G_{nm} V^{(i)}(z = 0) \quad (40)$$

where  $G_{nm} = \prod_{i=N}^1 \exp[D_{mn}^{(i)} h^{(i)}]$  is the global transfer matrix,  $V^{(i)}(z = h)$  and  $V^{(i)}(z = 0)$  are the vector states at the top and bottom surfaces of the plate, respectively.

As mentioned in the introduction section, the generality of the presented method allows for its application to various other problems, including vibration analysis. For instance, in solving the vibration equation, terms related to time are incorporated into the equilibrium equations (Eq. 3) on the right-hand side. These terms appear as  $\rho \frac{\partial^2 u}{\partial t^2}$ ,  $\rho \frac{\partial^2 v}{\partial t^2}$ , and  $\rho \frac{\partial^2 w}{\partial t^2}$  where  $t$  and  $\rho$  are time and density, respectively. Besides, the mode shape functions (Eq. 6) also include terms associated with time. This term is defined as  $e^{i\omega t}$  where  $\omega$  is natural frequency. References [Ying, Lü, and Chen \(2008\)](#) and [Lü, Lim, and Chen \(2009\)](#) provide

valuable insights into these issues.

### 4.3.1 Maxwell model for describing the viscoelastic foundation

To mathematically define the behavior of viscoelastic foundation, a hereditary approach is employed based on Boltzmann's superposition principle. According to this principle, if we assume that the strain history  $\varepsilon(t)$  follows a linear functional pattern, the formal representation of the stress-strain relationship can be expressed as follows [Hajikarimi and Nejad \(2021\)](#):

$$\sigma(t) = \int_{-\infty}^t K_n(t-\xi) \frac{dw(\xi)}{d\xi} d\xi = \int_{-\infty}^t K_n(t-\xi) dw(\xi) \quad (41a)$$

$$\tau(t) = \int_{-\infty}^t K_G(t-\xi) \frac{d\gamma(\xi)}{d\xi} d\xi = \int_{-\infty}^t K_G(t-\xi) d\gamma(\xi) \quad (41b)$$

where  $\xi$ ,  $\gamma$  are an integration variable and shear strain, respectively,  $K_n(t)$  and  $K_G(t)$  are relaxation functions of normal and shear layers for viscoelastic foundation, respectively.

In general, a viscoelastic model for the viscoelastic foundation can be defined using a physical model containing springs and dashpots. The generalized Maxwell model (GMM) is one of the widely used models which consists of multiple Maxwell elements connected in parallel. Fig. 4.2a. shows this configuration.

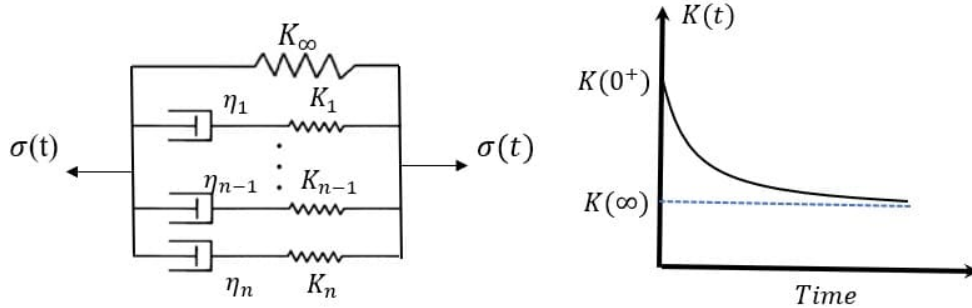


Figure 4.2: The generalized Maxwell model.

According to the differential form of viscoelasticity for each maxwell element,  $\frac{d\varepsilon}{dt} =$

$\frac{1}{E_i} \frac{d\sigma}{dt} + \frac{\sigma}{\eta_i}$ , the relaxation modulus function of the generalized Maxwell can be written individually in the analytical form of a series of exponential known as the Prony series:

$$K(t) = K_\infty + \sum_{i=1}^n K_i \exp\left(-\frac{t}{\tau_i}\right) \quad (42)$$

where  $K_\infty$  is the equilibrium modulus  $K_i$  is stiffness of each spring,  $n$ ,  $t$ , and  $\tau_i = \frac{\eta_i}{E_i}$  represent the number of Maxwell elements, time, and relaxation time, respectively. The relaxation modulus-time curve for the generalized Maxwell model is shown in Fig.4.2b. The coefficients of the generalized Maxwell model can be determined by employing a curve-fitting algorithm on experimental data (see [Kheradpisheh and Hojjati \(2023\)](#) for more information).

### 4.3.2 Coupled influence of viscoelastic foundation and exact solution

The critical buckling load ( $N_x$  and  $N_y$ ) can be determined from Eq. (40) by considering the appropriate boundary condition imposed on the bottom and top surfaces ( $z = 0$ , and  $h$ ) of the laminated plate. Since the bottom surface of the plate is subjected to the viscoelastic foundation, the equilibrium equation for an element of the viscoelastic shear layer in the  $z$ -direction at the bottom surface ( $z=0$ ) is written as follows (see Fig. 4.3):

$$\sigma_{z=0}(t) = \sigma_n(t) - \frac{\partial \tau_x(t)}{\partial x} - \frac{\partial \tau_y(t)}{\partial y} \quad (43)$$

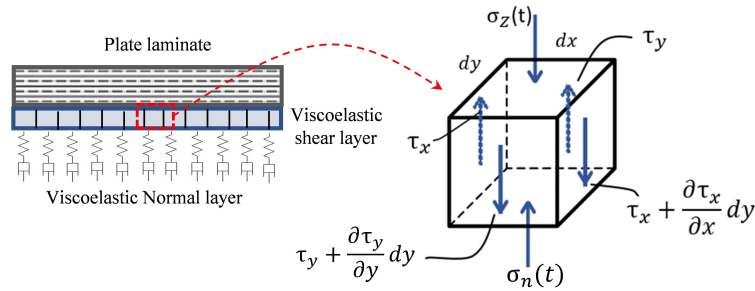


Figure 4.3: Schematic of stress components in an element of the viscoelastic shear layer.

By replacing the expressions from Equation (41) in Eq. (43), while considering the relationships  $\gamma_x = \frac{\partial w}{\partial x}$  and  $\gamma_y = \frac{\partial w}{\partial y}$ , and also substituting Eq. (37) into Eq. (43), performing some simple calculations, one can derive the following result:

$$\begin{aligned}\bar{\Psi}_z(t) = & \int_{-\infty}^t K_n(t-\xi) \frac{d\bar{W}(\xi)}{d\xi} d\xi + \mu_{ma}^2 \int_{-\infty}^t K_{Gx}(t-\xi) \frac{d\bar{W}(\xi)}{d\xi} d\xi \\ & + \mu_{nb}^2 \int_{-\infty}^t K_{Gy}(t-\xi) \frac{d\bar{W}(\xi)}{d\xi} d\xi\end{aligned}\quad (44)$$

Then, applying Laplace transform to Eq. (44) leads to:

$$\bar{\Psi}_{z=0}(s) = s\tilde{W}(s)[\tilde{K}_n(s) + \mu_{ma}^2 \tilde{K}_{Gx}(s) + \mu_{nb}^2 \tilde{K}_{Gy}(s)] \quad (45)$$

where  $\bar{\Psi}_{z=0}(s) = \tilde{K}(s) \tilde{W}(s)$  are the Laplace transform of  $\bar{\Psi}_z(0)$ ,  $K(t)$ , and  $W(t)$  and  $s\tilde{K}(s)\tilde{W}(s)$  is obtained from the following Laplace integral:

$$s\tilde{K}(s)\tilde{W}(s) = \int_0^\infty \int_{-\infty}^t e^{-st} K_z(t-\tau) \frac{dw(\xi)}{d\xi} d\xi dt$$

Applying inverse Laplace to Eq. (45), the time-dependent stress response at the bottom surface of the plate is written in the form:

$$\Psi_{z=0}(t) = [K_n(t) + \mu_{ma}^2 K_{Gx}(t) + \mu_{nb}^2 K_{Gy}(t)]W(z=0) \quad (46)$$

Furthermore, other boundary conditions at the lateral surfaces ( $z = 0$  and  $z = h$ ) of the plate can be expressed as:

$$\tau_{xz}(0) = \tau_{yz}(0) = 0 \quad (47a)$$

$$\sigma_z(h) = \tau_{xz}(h) = \tau_{yz}(h) = 0 \quad (47b)$$

Making use of Eq. (46) into Eq. (40), one can derive the following linear system of

equations.

$$\begin{bmatrix} \bar{\Psi}_z(h) \\ \bar{U}(h) \\ \bar{V}(h) \\ \bar{W}(h) \\ \bar{\Gamma}_{xz}(h) \\ \bar{\Gamma}_{yz}(h) \end{bmatrix} = \begin{bmatrix} G_{mn}^{1,2} & G_{mn}^{1,3} & \lambda(t)G_{mn}^{1,1} + G_{mn}^{1,4} & G_{mn}^{1,5} & G_{mn}^{1,6} \\ G_{mn}^{2,2} & G_{mn}^{2,3} & \lambda(t)G_{mn}^{2,1} + G_{mn}^{2,4} & G_{mn}^{2,5} & G_{mn}^{2,6} \\ G_{mn}^{3,2} & G_{mn}^{3,3} & \lambda(t)G_{mn}^{3,1} + G_{mn}^{3,4} & G_{mn}^{3,5} & G_{mn}^{3,6} \\ G_{mn}^{4,2} & G_{mn}^{4,3} & \lambda(t)G_{mn}^{4,1} + G_{mn}^{4,4} & G_{mn}^{4,5} & G_{mn}^{4,6} \\ G_{mn}^{5,2} & G_{mn}^{5,3} & \lambda(t)G_{mn}^{5,1} + G_{mn}^{5,4} & G_{mn}^{5,5} & G_{mn}^{5,6} \\ G_{mn}^{6,2} & G_{mn}^{6,3} & \lambda(t)G_{mn}^{6,1} + G_{mn}^{6,4} & G_{mn}^{6,5} & G_{mn}^{6,6} \end{bmatrix} \begin{bmatrix} \bar{U}(0) \\ \bar{V}(0) \\ \bar{W}(0) \\ \bar{\Gamma}_{xz}(0) \\ \bar{\Gamma}_{yz}(0) \end{bmatrix} \quad (48)$$

where  $G_{mn}^{i,j}$  are the components of the global transfer matrix  $G_{mn}$ , and  $\lambda(t) = K_n(t) + \mu_{ma}^2 K_{Gx}(t) + \mu_{nb}^2 K_{Gx}(t)$ . Then by direct substituting the values of Eq. (47) into Eq. (48), the following system of equations can be extracted:

$$\begin{bmatrix} G_{mn}^{1,2} & G_{mn}^{1,3} & \lambda(t)G_{mn}^{1,1} + G_{mn}^{1,4} \\ G_{mn}^{5,2} & G_{mn}^{5,3} & \lambda(t)G_{mn}^{5,1} + G_{mn}^{5,4} \\ G_{mn}^{6,2} & G_{mn}^{6,3} & \lambda(t)G_{mn}^{6,1} + G_{mn}^{6,4} \end{bmatrix} \begin{bmatrix} \bar{U}(0) \\ \bar{V}(0) \\ \bar{W}(0) \end{bmatrix} = \begin{bmatrix} 0 \\ 0 \\ 0 \end{bmatrix} \quad (49)$$

As a result, the nontrivial solution for Eq. (49) can be determined as:

$$\begin{vmatrix} G_{mn}^{1,2} & G_{mn}^{1,3} & \lambda(t)G_{mn}^{1,1} + G_{mn}^{1,4} \\ G_{mn}^{5,2} & G_{mn}^{5,3} & \lambda(t)G_{mn}^{5,1} + G_{mn}^{5,4} \\ G_{mn}^{6,2} & G_{mn}^{6,3} & \lambda(t)G_{mn}^{6,1} + G_{mn}^{6,4} \end{vmatrix} = 0 \quad (50)$$

Therefore, the buckling load values corresponding to different mode shapes (n,m) are determined through the solution of the above equation.

Table 4.1: Material properties of graphite composite material.

<i>Material constants</i>	<i>Graphite – composite</i>
$E_1$	155 <i>GPa</i>
$E_2$	12.1 <i>GPa</i>
$E_3$	12.1 <i>GPa</i>
$\nu_{12}$	0.248
$\nu_{13}$	0.248
$\nu_{23}$	0.458
$G_{12}$	4.7 <i>GPa</i>
$G_{13}$	4.7 <i>GPa</i>
$G_{23}$	3.2 <i>GPa</i>

## 4.4 Analytical results and discussion

In order to illustrate the general buckling behavior of the laminated plate resting on a viscoelastic foundation, a graphite laminated composite plate on a viscoelastic foundation is considered. The material properties of graphite composite are given in Table 4.1.

### 4.4.1 Validation of the proposed method

To validate the presented theory, a comparison is made between the results obtained in this study and those reported in the literature [J. N. Reddy \(2003\)](#). Due to the limited availability of validation data and for convenience in analysis and discussion, the buckling loads of a laminated composite on an elastic foundation are initially examined. Subsequently, the influence of a viscoelastic foundation on the buckling load is investigated in the following section.

To compare the results of the proposed 3D elasticity theory in this research and classical laminate theory (CLT) presented at the work [J. N. Reddy \(2003\)](#), the buckling loads of a graphite cross-ply composite laminate with a stacking sequence of [0/90/90/0] are computed using both approaches for two different shape modes ( $m = 1$ , and 2). The values of the spring constants of the shear foundation are considered to be the same in the x and y directions ( $K_{Gx} = K_{Gy}$ ), and the thickness of each ply in this example is assumed to be 0.15 mm. Table 4.4.1 represents the comparison between the present work and the results obtained using classical laminate theory [J. N. Reddy \(2003\)](#). The results presented in Table 4.4.1

Table 4.2: The comparison of the buckling loads determined on the basis of the presented method and classical laminate theory

a/b		<b>Kn=100, Kg=0</b>		<b>Kn=0, Kg=10</b>		<b>Kn=10, Kg=10</b>	
		CLT theory	Presented theory	CLT theory	Presented theory	CLT theory	Presented theory
m=1 n=1	0.8	9.78	9.80	11.64	11.70	11.75	11.82
	0.9	8.77	8.86	10.62	10.69	10.77	10.83
	1	8.25	8.32	10.09	10.16	10.28	10.34
	1.1	8.06	8.13	9.90	9.96	10.13	10.18
	1.2	8.13	8.20	9.96	9.98	10.23	10.27
	1.3	8.38	8.40	10.21	10.22	10.52	10.56
	1.4	8.78	8.79	10.61	10.64	10.98	11.01
	1.5	9.33	9.35	11.14	11.17	11.57	11.60
m=2 n=1	2	8.25	8.32	10.09	10.14	10.28	10.32
	2.1	8.12	8.18	9.96	10.01	10.17	10.20
	2.2	8.06	8.13	9.90	9.95	10.13	10.16
	2.3	8.07	8.14	9.90	9.95	10.15	10.18
	2.4	8.12	8.16	9.96	9.99	10.23	10.26
	2.5	8.23	8.27	10.06	10.09	10.35	10.40
	2.6	8.38	8.40	10.20	10.21	10.53	10.56
	2.7	8.56	8.57	10.39	10.39	10.73	10.75

demonstrate an excellent agreement between the findings of the present study and those obtained through classical laminate theory.

#### 4.4.2 The effect of the spring constants of the foundation and aspect ratio on the buckling load

The buckling load of the laminated plate is plotted as a function of the aspect ratio and different values of the spring constant of the foundation in Fig. 4.4. In Figure 4.4a, it can be observed that for moderate values of  $K_n$  ( $100 < K_n < 1000$ ), the buckling load decreases as the aspect ratio increases. On the other hand, an interesting observation is made in Figure 4.4b, where larger values of  $K_n$  ( $5000 < K_n$ ) exhibit an increase in the buckling load with an increasing aspect ratio. The underlying reason for this behavior is that, with higher aspect ratios, the foundation applies stronger stress to the bottom surface of the plate, thereby resulting in an increase in buckling load. These results indicate that if the foundation's elasticity surpasses a specific value, reducing the aspect ratio, as one of

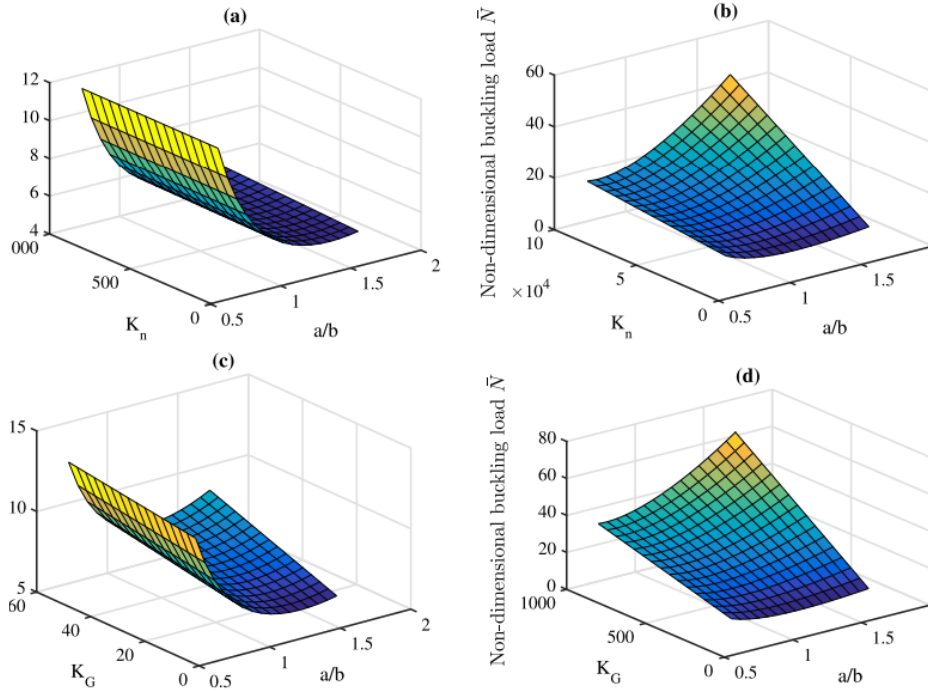


Figure 4.4: The values of buckling load as a function of the aspect ratio and Spring constant of the foundation.

the common ways to reduce buckling in structures, not only fails to prevent buckling but can potentially expedite the onset of buckling in the structure.

#### 4.4.3 The effect of time parameter at normal and shear viscoelastic modulus $K(t)$ on the transient buckling response

Based on the Generalized Maxwell Model (GMM) presented for the viscoelastic behavior of the foundation, the transient buckling responses can be categorized into several types: plate buckling can initiate immediately after the load is applied to the plate. This buckling load corresponds to the value of the relaxation modulus of the foundation in the first moment ( $K(0^+)$ ) which is called the highest buckling load (See Fig. 4.2). In addition, the plate can buckle after relaxation occurs in the viscoelastic foundation. The buckling load reaches its lowest value when the viscoelastic foundation completely relaxes. This buckling load is attributed to the value of relaxation modulus over time ( $K(\infty)$ ). Fig. 4.5 shows the transient buckling load versus the aspect ratio for the laminated plate. Accordingly, the

value of the relaxation modulus ( $K_n(t)$ ) is considered to be  $K_n(t) = 1000 + 2000e^{-0.02t}$  for the calculation. The graphs in Fig. 4.5 present that initially, there is a rapid decrease in the buckling load, but as time progresses, this rate of reduction diminishes. Moreover, it can be observed that the aspect ratio corresponding to the onset of the second mode in the plate increases over time. This trend is demonstrated in Fig. 4.5, where the aspect ratio values at time zero, 100 s, and infinity are recorded as 1.88, 1.97, and 2, respectively.

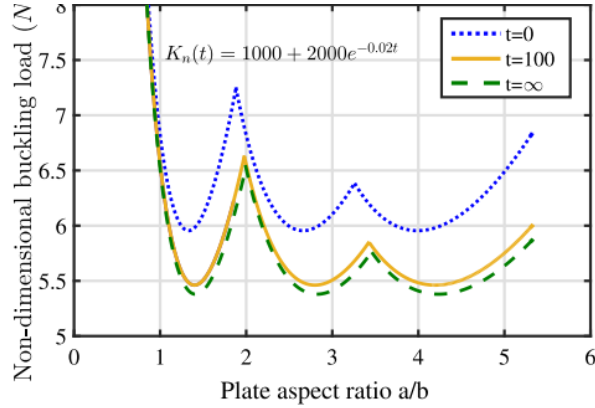


Figure 4.5: A schematic of automated fiber placement.

Since viscosity has a direct relation with relaxation time ( $\tau = \frac{\eta}{E}$ )n, in order to investigate the effect of the viscosity coefficient on the buckling load, the diagrams of buckling load versus time for different relaxation time values are plotted in Fig. 4.6. This figure is plotted for two different relaxation modulus values, one with a lower value  $K_n(t) = 250 + 600e^{-\tau t}$  and another with a higher value  $K_n(t) = 500 + 900e^{-\tau t}$ . The most important observations from Fig. 4.5 can be outlined as follows:

- An increase in the viscosity coefficient results in a longer relaxation time. This leads to a reduction in the rate at which the buckling loads change over a period. In other words, when viscosity increases, the slope of the buckling-time graph decreases, indicating a slower rate of change in the buckling loads.
- For the lower value of the relaxation modulus, the probability of the occurrence of the second mode instead of the first mode decreases with increasing time. The viscoelastic property of the foundation contributes to the occurrence of the first mode instead of

the second mode in aspect ratios near 2. As can be observed from the graphs, for  $\tau = 200$ ,  $\tau = 100$ , and  $\tau = 50$ , the first mode replaces the second mode after 219s, 104s, and 52s respectively, and for the higher value of the modulus, this transition to the second mode occurs more rapidly, and the second mode displaces the first mode right from the beginning (time= zero).

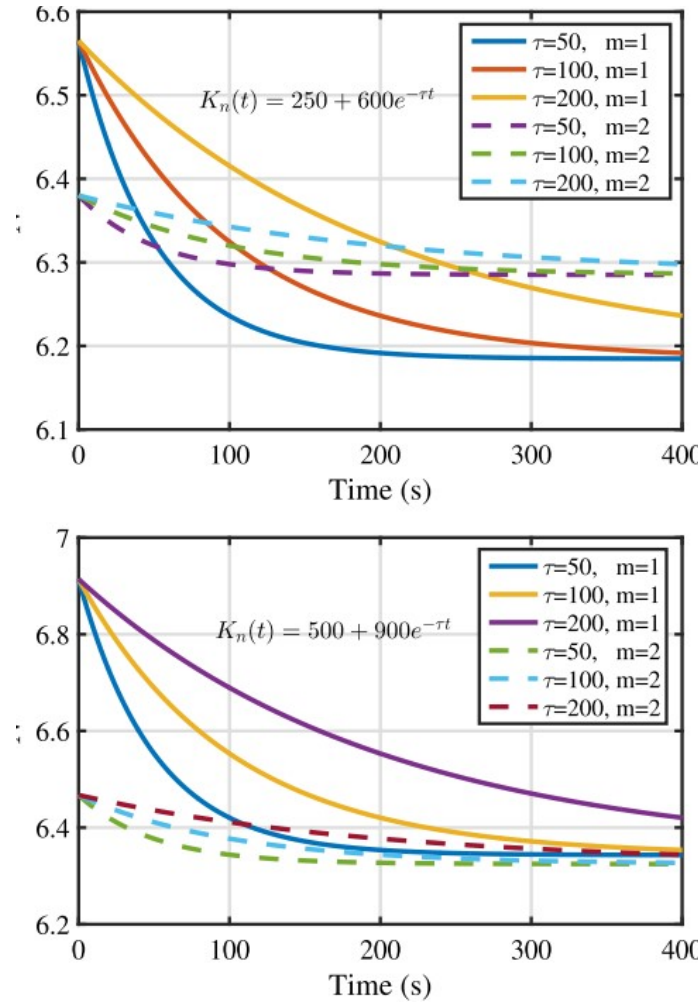


Figure 4.6: The response of the buckling load versus aspect ratio changes with considering the time effect on the viscoelastic foundation.

## 4.5 Numerical simulation and results

#### 4.5.1 Description of finite element model (FEM)

For further investigation and validation, the ABAQUS/Explicit software was employed to simulate the buckling response of the composite rectangular plate supported by an elastic foundation and subjected to in-plane loading. The rectangular composite plate is modeled as a shell structure (plate) and each composite ply thickness is considered to be 0.15mm. Therefore, the thickness of shell structure is related to the number of layers. The material for the shell structures is determined as a type of engineering constant with the properties listed in Table 1. The simply supported conditions are adopted for all edges of the plate. In the next step, the elastic foundation is modeled through the interaction section in ABAQUS software. In this section, the elastic elements are introduced in the initial step with an assigned stiffness (Spring constant). A 4-node doubly curved thin or thick shell element (S4R) is used to discretize the composite plate. The mesh size is also considered to be 1mm to produce good agreement with the literature and presented model results. Finally, the first five modes of buckling for each plate are calculated using simulation.

#### 4.5.2 Numerical results

The comparison between the presented method and the FE method for a plate with a lay-up sequence of [0/90/90/0] is presented in Table 4.3. The results reveal a high level of agreement between the FE model and the presented method. Further investigation in Table 4.3 yields an interesting finding: increasing the stiffness of the elastic foundation causes the order of buckling mode shapes to change in the composite plate. For example, by increasing the stiffness from 0 to 0.04 N/mm, the plate's second, third, and fourth modes ( $m=2,3,4$ ,  $n=1$ ) occur earlier than the first mode ( $m=1$ ,  $n=1$ ).

#### 4.5.3 Thickness and Lay-up sequence effect

One of the significant advantages of composite materials is their ability to determine different sequences for the lay-up. For example, a change in the lay-up sequence can result in

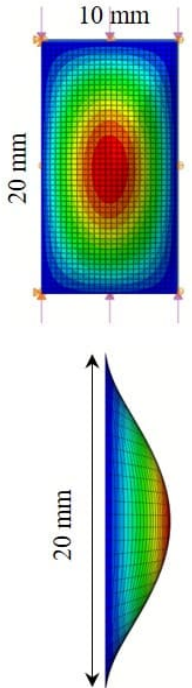
Table 4.3: Comparing the buckling loads calculated using the presented method with those from the FE method.

Plate dimension and spring constant	mode shapes	Presented method	FE method
a=100, b=50mm, $K_n=0$	m=1, n=1	12.85	13.04
	m=2, n=1	13.81	13.78
	m=3, n=1	24.63	24.79
	m=4, n=1	42.45	41.31
	m=3, n=2	44.01	45.3
a=100, b=50mm, $K_n=0.04$ N/mm	m=2, n=1	23.89	24.02
	m=3, n=1	29.25	29.34
	m=4, n=1	43.93	43.76
	m=3, n=2	48.86	49.95
	m=1, n=1	53.44	54.71
a=100, b=50mm, $K_n=0.1$ N/mm	m=3, n=1	36.02	36.16
	m=2, n=1	38.49	39.05
	m=3, n=2	55.29	56.94
	m=4, n=2	60.84	61.87
	m=5, n=1	67.31	66.72

different buckling responses. In this regard, to investigate how thickness and lay-up sequence affect buckling responses, buckling loads are calculated for a 20mm by 10mm rectangular plate with various thicknesses and lay-up sequences. The reduction in plate dimensions is intended to increase the length-to-thickness ratio, allowing for better observation of the shear load's impact on buckling loads. The results of buckling loads for plates with different length-to-thickness ratios are shown in Table 4.4.3. The buckling loads were calculated using the finite element (FE) method, the presented method (PM) proposed in this study, and classical laminate theory (CLT). As shown in Table 4.4.3, as the length-to-thickness ratio increases, CLT predicts higher buckling loads compared with both the FE method and the presented method. This discrepancy is because the FE method's mesh elements can account for shear stress in thick plates, and the presented method, as per Eq. 4, considers shear stress effects in plate calculations. In contrast, classical laminate theory does not consider shear stress effects, leading to higher predictions than the FE and presented methods.

Besides the effect of lay-up sequence is shown in Table 4.5 The most important observation from Table can be outlined as: While initially it seems that the plate with a lay-up sequence of [0/0/0/0] buckles under higher in-plane loading, the findings indicate

Table 4.4: The effect of length-to-thickness ratio on buckling response.

First mode and details of boundary conditions and the mesh	Length to thickness ratio ( $a/h$ ) and lay-up sequence	Critical buckling loads for each method ( $N/mm$ )
	[0]	FEM: 3.1 PM:3.1
	$a/h=133$	CLT: 3.1
	[0/0]	FEM: 25 PM:24
	$a/h=66$	CLT: 24
	[0/0/0/0] $a/h=33$	FEM: 192 PM:196 CLT: 199
	[0/0/0/0/0/0] $a/h=22$	FEM: 622 PM:634 CLT: 673
	[0]	FEM: 6.98 PM:7.15
	$a/h=133$	CLT: 7.16
	[0/0]	FEM: 29.81 PM:29.84
	$a/h=66$	CLT: 29.84
	[0/0/0/0]	FEM: 199 PM:199
	$a/h=33$	CLT: 203
	[0/0/0/0/0/0] $a/h=22$	FEM: 635 PM:645 CLT: 677

that the plate with the sequence of  $[0/90/90/0]$  buckles at higher force levels. This is attributed to the boundary condition, since the plate is simply supported on all four sides, which makes it stronger due to the presence of 90-degree layers in the transverse direction, resulting in a delayed threshold in out-of-plane deformation. A notable observation can be obtained from comparing the initial buckling loads of the laminate configurations  $[0/90/90/0]$ ,  $[90/0/0/90]$ , and  $[90/0/90/0]$ . It is evident that the highest initial buckling load corresponds to the  $[0/90/90/0]$  lay-up, while the lowest is associated with  $[90/0/0/90]$ . This difference can be attributed to the distribution of the moment resultants within the plate. According to mechanical principles, inducing bending deformation in a plate with outer layers of higher stiffness is more challenging than in a plate with outer layers of lower stiffness, resulting in a higher initial buckling load for the former. Indeed, since the  $[0/90/90/0]$  includes layers with higher stiffness the outer layer has a higher initial buckling load compared to the  $[90/0/0/90]$  and  $[90/0/90/0]$ . Besides, it can also be seen that despite having the same number of layers and orientations, variations in their lay-up sequences lead to changes in the buckling mode shapes occurring at the composite plates. For example, in lay-ups  $[0/0/0/0]$  and  $[0/90/90/0]$ , mode shape ( $m = 1$  and  $n = 1$ ) occurs first, while in  $[90/0/0/90]$ , mode shape ( $m = 3$  and  $n = 1$ ) appears first, and in  $[0/90/0/90]$ , mode ( $m = 2$  and  $n = 1$ ) occurs first.

## 4.6 Conclusion

In this research paper, a novel approach is proposed to investigate the buckling behavior of a cross-ply laminated composite resting on both normal and shear viscoelastic layers. The three-dimensional elasticity theory and the state-space method are employed to derive the governing equations for the laminated plate. Furthermore, a straightforward technique using Boltzmann's superposition principle along with the Laplace transform is employed to couple the viscoelastic foundation equation with the buckling equation. The research analyzes the influence of a range of parameters, including geometric aspects and viscoelastic properties such as time, relaxation time, and viscosity, on the buckling response of the laminated plate.

The numerical results are presented for a cross-ply laminate with stacking sequence

Table 4.5: The effect of lay-up sequence on buckling response.

Buckling load $N/mm$		
Lay-up sequence and foundation constant	Three corresponding mode shapes and buckling loads	
[0/0/0/0] & $K_n=0$	$m = 1, n = 1$	$m = 2, n = 1$
	FEM: 7.98	FEM: 13.61
	PM:7.98	PM: 13.70
[0/90/90/0] & $K_n=0$	$m = 1, n = 1$	$m = 2, n = 1$
	FEM: 13.42	FEM: 13.78
	PM:12.85	PM: 13.81
[90/0/0/90] & $K_n=0$	$m = 3, n = 1$	$m = 4, n = 1$
	FEM: 10.94	FEM: 12.81
	PM:10.9	PM: 13.81
[0/90/0/90] & $K_n=0$	$m = 2, n = 1$	$m = 2, n = 1$
	FEM: 12.07	FEM: 15.66
	PM:12.32	PM: 17

[0/90/90/0] supported by a viscoelastic foundation with both viscoelastic normal and shear layers. The computed results show that when the plate is in contact with the foundation, there is a significant threshold. If the foundation stiffness surpasses this threshold, the conventional method of reducing the aspect ratio to prevent buckling not only proves ineffective in reducing the probability of buckling but also leads to an increase in the occurrence of buckling. The reason behind this behavior is that as the aspect ratios increase, the foundation applies more stress to the bottom surface of the plate, causing the buckling load to increase. The surface plotted in Fig. 4.4 shows this fact. Moreover, it is found from numerical results that higher viscosity coefficients result in a reduced slope of the buckling-time graph, indicating a slower rate of change in the buckling loads. Besides, the viscoelastic property of the foundation has also an effect on the occurrence of the first mode instead of the second mode in the constant aspect ratio. Indeed in lower values of relaxation modulus, with passing time the first mode happens in the plate instead of the second mode in a constant aspect ratio. Together, a finite element simulation is developed in ABAQUS to capture the buckling response accurately. An important observation from both the finite element and analytical results is that, contrary to initial expectations, the plate with a [0/0/0/0] lay-up sequence was expected to buckle under higher in-plane loading. However,

the findings indicate that the plate with a  $[0/90/90/0]$  sequence buckles at higher force levels. This difference is attributed to the boundary condition; the plate is simply supported on all four sides, making it stronger due to the presence of 90-degree layers in the transverse direction, which delays the threshold for out-of-plane deformation.

It is also worth mentioning that the proposed analysis does not make any assumptions on the deformation of the plate which ensures the precision of our research. In addition, the proposed method can be applied to a wide range of mechanical problems , including those involving viscoelastic foundations, buckling of the structures subjected to lateral and transverse load, and structures with imperfect interfaces, etc.

## Chapter 5

# In-plane and out-of-plane deformations in automated fiber placement employing micromechanics method

This work has been published in:

**Kheradpisheh, Meisam, and Mehdi Hojjati. "In-plane and out-of-plane deformations in automated fiber placement employing micromechanics method." *Composites Part A: Applied Science and Manufacturing* 170 (2023): 107543.**

### 5.1 Abstract

An experimental and theoretical investigation is performed on the in-plane and out-of-plane configurations of the thermoset tow preregs in the automated fiber placement (AFP) process. Both in-plane and out-of-plane deformations, also known as waviness and wrinkle defects, respectively, are created mainly due to steering during the AFP process.

This paper aims to present a viscoelastic micro-mechanics approach to capture the behavior of planar and non-planar deformations in order to predict these defects during the process and, more importantly, determine the conditions under which either in-plane or out-of-plane deformations occur. In this regard, a fiber-buckling model is employed to describe the deformation behavior of the fibers embedded in a viscoelastic uncured thermoset matrix. In this approach, fiber is considered as an elastic material embedded in an uncured viscoelastic matrix. The stickiness of the matrix in out-of-plane and in-plane directions is measured by different relaxation test methods using a rheometer equipment. On the basis of the obtained solutions, critical radii for in-plane and out-of-plane deformations are derived. The wavelength changes of out-of-plane buckling in the width direction of a steered tow are calculated and compared with the experimental results. In addition, we show the separation between the threshold of critical loading and critical radius for both in-plane and out-of-plane buckling in a steered tow. Finally, the values of the relaxation modulus that lead to a mixed mode in planar buckling are obtained, and also the effect of these values on the deformation behavior of in-plane buckling are discussed.

## 5.2 Introduction

Carbon fiber reinforced polymer (CFRP) materials have attracted great attention from industry and academia thanks to their high strength-to-weight ratio, and excellent specific mechanical and chemical resistance. In this regard, to meet the increasing demand for reducing the production cycle time and manufacturing large-scale composite parts, new manufacturing technologies and processes, such as automated fiber placement (AFP) systems, arose. In the AFP process, the composite parts are fabricated in plies. Each ply is composed of unidirectional prepreg tows delivered side by side through the fiber placement head and then heated and compacted on the mold surface [Böckl, Wedel, Misik, and Drechsler \(2022\)](#); [Nguyen, Vu, and Ferrier \(2019\)](#).

Despite the great benefits of AFP technology, however, the occurrence of various defects during the AFP process still remains a significant challenge in the manufacturing industry.

The presence of these defects gives rise to a significant reduction in the structural performance of the parts produced by the AFP process. The defects can depend on the AFP process parameters, initial imperfections of prepreg materials, and the complexity of the part or steered preregs. Since the main use of the AFP machine is manufacturing large complex structures, steering the tow so as to ensure acceptable part quality is an absolute necessity, and as a consequence, the defects that occurred during the steering have received interest from researchers [Das, Choong, Dillard, De Focatiis, and Bortner \(2022\)](#); [Y. Wang, Belnoue, Ivanov, and Hallett \(2021\)](#). Two main defects most likely to occur during tow steering are in-plane and out-of-plane buckling, also known as waviness and wrinkle, respectively. The cause of these defects is due to the mismatch between the length of the curvilinear path on the surface and the actual length of the tow before placing it on the predetermined path [Oromiehie, Prusty, Compston, and Rajan \(2019\)](#); [Rousseau, Wehbe, Halbritter, and Harik \(2019\)](#). Firstly, the in-plane buckling occurs at the inner edge of the prepreg tape due to steering the prepreg tape which is causing the inner edge of the tape to be compressed. If the curvature radius is smaller than a certain value, the compressive load in the inner edge of the prepreg tape increases and causes the inner edge of the tape to buckle in the out-of-plane direction [Hörmann \(2015\)](#).

### 5.2.1 Related work

The relevant research related to steering defects can be investigated into two categories. Firstly, we study the researches that investigate experimentally the in-plane and out-of-plane defects during the steering process. Then the publications focusing on the mechanical and analytical models of the in-plane and out-of-plane buckling are reviewed.

- Experimental studies:

To develop a model and remove the defects, it is essential to understand the occurrence of defects at the steered tape. In this regard, recently scholars have experimentally studied the formation of defects due to the steering process. Extensive AFP trials in a variety of process conditions were conducted by [Bakhshi and Hojjati \(2018\)](#) to investigate the defect formation

during the steering process. The work in [Rajan et al. \(2019\)](#) experimentally studied wrinkle formation and waviness in steered and straight tapes using StereoDIC camera. A full-field 3D shape and deformation data were retrieved by StereoDIC, which was valuable for a deeper understanding of the defects in tow steering. In [R. Wehbe, Sacco, et al. \(2020\)](#), the influence of process parameters, including temperature, head speed, and compaction force on the quality of a steered tow on a cylindrical mold. The work in [Tang et al. \(2022\)](#) investigated the presence of wrinkles and waviness in specimens created by the AFP machine led to an about 12% decrease in bending properties of specimens. The effect of the non-planar wrinkle defects on the failure behavior of  $L$  shaped composite laminate is studied in [H. Hu et al. \(2021\)](#). The author in [Mizukami et al. \(2016\)](#), presented a new experimental method for the detection of in-plane and out-of-plane defects in unidirectional carbon fiber-reinforced plastics. In [Hörmann \(2015\)](#), the impact of the waviness on the mechanical properties of the cured thermoset prepreg was investigated. In addition, the compaction roller as an important component of fiber placement head was experimentally and numerically studied in [Bakhshi and Hojjati \(2020\)](#); [Jiang et al. \(2019\)](#); [Jiang, He, Wang, and Ke \(2021\)](#); [Poursartip et al. \(2021\)](#). The work in [Bakhshi and Hojjati \(2020\)](#) studied the five different compaction roller made of polyurethane and steel and their effect on the quality of the steered tows. The authors also investigated the pressure distribution and surface contact of each roller during the AFP process. The authors in [Rajasekaran and Shadmehri \(2022\)](#) studied the relationship between an in-situ treatment, AKA repass, and the quality and geometry of the thermoplastic steered tape.

Besides, due to the importance of interfacial stickiness between the uncured prepreg and substrate in out-of-plane and in-plane deformations, the works in [Beakou et al. \(2011\)](#); [Budelmann et al. \(2019, 2020\)](#); [R. Crossley et al. \(2012\)](#); [R. J. Crossley et al. \(2013\)](#); [A. Smith, Endruweit, Choong, De Focatiis, and Hubert \(2020\)](#) focused on measuring the stickiness of the prepreg experimentally. In [Beakou et al. \(2011\)](#), the authors measured prepreg tack using a probe test. The approach employed in this study for measuring the tackiness of the prepreg involved the use of a probe that contacts the prepreg's surface, then it is separated. During the separation, The separation force and tack energy were measured

and recorded and as consequence, the slope of the force-displacement plot was considered as the normal stiffness of the interface between the prepreg and substrate. The authors in [Budelmann et al. \(2019\)](#) performed a probe tack test to determine the tackiness of the prepreg employing rotational rheometer equipment. They applied a constant compaction force by the probe to the surface of the prepreg sample, and then the probe is slowly separated during the tensile phase. During the test, the separation force is recorded until the measured stress reached zero. In the works [R. Crossley et al. \(2012\)](#); [R. J. Crossley et al. \(2013\)](#), a new peel test method was developed to determine the dynamic stiffness and the tackiness of the prepreg. The test rig comprises two pairs of rollers: the first set guides the rigid substrate imitating the mold surface during the AFP process while the second set of spring-loaded rollers applies the compaction force to the prepreg's surface. During the test, by separating the prepreg material at a  $90^\circ$  peel using a universal test machine, the dynamic stiffness and peel force results were measured. In addition, the influence of the temperature and feed rate on the tack and dynamic stiffness of the prepreg were presented. In [A. Smith et al. \(2020\)](#), the relationship between the tackiness of prepreg and process parameters, such as feed rate, and temperature was examined through a new single-stage peel method which is introduced in the work [R. Crossley et al. \(2012\)](#). In the work [Pan, Yang, Qu, Li, and Ke \(2022\)](#), the authors employed a probe tack test, which was mounted on a universal tensile testing machine, to measure the normal tackiness response of the prepreg matrix.

- Mechanical and analytical models:

Experimental observation of defects during tow steering led to an interest in modeling and numerically investigating these defects. A number of works have analytically modeled the out-of-plane wrinkle as a buckling of the plate resting on an elastic foundation [Bakhshi and Hojjati \(2019\)](#); [Beakou et al. \(2011\)](#); [Belhaj and Hojjati \(2018\)](#); [Kheradpisheh and Hojjati \(2021\)](#); [Matveev et al. \(2016\)](#). The out-of-plane wrinkle was modeled as a plate buckling was for the first time in the work [Beakou et al. \(2011\)](#). The authors considered the tow as

a solid plate under a linearly varying load provided by the compaction roller, and the interface adhesion between the tow and substrate was defined as an elastic foundation. Then, the authors of [Matveev et al. \(2016\)](#) modified the model and also validated the developed model using the experimental results. The effect of the in-plane shear parameter on wrinkling of a steered tow was analytically investigated in the work [Belhaj and Hojjati \(2018\)](#). Regarding the viscoelasticity of the prepreg matrix, the authors in [Bakhshi and Hojjati \(2019\)](#) presented a theoretical model taking into consideration the viscoelastic properties of the wrinkle formation. Investigation of the initial imperfection due to the initial waviness of the tape or initial imperfections of the substrate on wrinkle formation is modeled in the work [Kheradpisheh and Hojjati \(2021\)](#). The authors employed a Koiter model to describe the initial imperfection, showing that initial imperfection leads to a decrease in the critical buckling load. Furthermore, different finite element models for out-of-plane deformations at tow were presented in [Bakhshi and Hojjati \(2018\)](#); [Le, Zobeiry, Erkmén, and Malek \(2021\)](#); [Rajan et al. \(2020\)](#). The authors in [Rajan et al. \(2020\)](#), modeled the tackiness between the tow and substrate using cohesive surface interaction. For their model, they found modes I and II of traction separation law using rigid cantilever beam experiments. In-plane buckling (waviness) models were analytically presented in [Hörmann \(2015\)](#); [R. Y. Wehbe, Harik, and Gurdal \(2019\)](#). The author in [Hörmann \(2015\)](#) presented a strain energy model to describe in-plane waviness within steered prepreg slit tape. In [R. Y. Wehbe et al. \(2019\)](#), an energy approach was utilized for a steered tow surrounded by an elastic foundation to model the in-plane deformations occurring due to the steering in the AFP process. The in-plane and out-of-plane bucklings of a slender embedded in a matrix using Timoshenko beam theory were studied by [Su, Liu, Terwagne, Reis, and Bertoldi \(2014\)](#). The main difference between the models presented for in-plane and out-of-plane bucklings is that in-plane models obtain the energy equation for the fiber and the out-of-plane models derive the energy equations for the prepreg as a plate.

Although the aforementioned researchers have investigated the defects, a few of them have worked on mathematical modeling to study the in-plane buckling formation [Hörmann \(2015\)](#); [R. Y. Wehbe et al. \(2019\)](#). They considered the strain energy for the prepreg tape

to predict in-plane waviness at the steered tape. On the other hand, the researchers that focused on wrinkle formation have considered wrinkles as plate buckling. In this regard, although according to the experimental observations and the literature review the nature of the formation of in-plane and out-of-plane defects during the steering process is similar to each other, their proposed models are different and are often modeled on a macro scale. As a result, in this paper, a micro-mechanical approach is employed to model both planar and non-planar deformations in the steered prepreg tape.

### 5.2.2 Contributions

This research focuses on modeling the in-plane and out-of-plane deformations in a steered prepreg tow during the AFP process. Within this framework of linear stability theory, a micro-mechanics approach is presented to study the in-plane and out-of-plane buckling of the fiber embedded in the viscoelastic matrix in uncured prepreg slit tapes. In this case, we consider the fiber as an elastic material and the resin matrix as a viscoelastic foundation to develop a fiber buckling model for both in-plane and out-of-plane bucklings. Due to the different properties of prepreg tape in out-of-plane and in-plane directions, two generalized Maxwell models are obtained by rheological test methods for modeling viscoelastic foundations. The contributions of this paper are highlighted as follows:

- We propose a micro-mechanics model to account for the viscoelastic behaviour of both wrinkle and waviness during the steering process. presenting a fiber buckling model for both defects makes a contribution to investigate and compare two defects with each other.
- In our model, we propose two relaxation tests using a rheometer to measure prepreg viscoelastic modulus for in-plane and out-of-plane buckling models. Two generalized Maxwell models with different parameters are driven for prepreg relaxation modulus in each direction by applying curve fitting on experimental results.
- In this research, A mathematical explanation is obtained for why in-plane waviness usually accompanies by a slight out-of-plane buckling. Our results are also validated

Table 5.1: AFP process conditions used during the steering.

Compaction force (N)	Nitrogen gas temperature (C)	Flow rate of Nitrogen (L/min)	Feed rate (mm/s)	Radius of curvature (cm)
250	160	85	76	75

by experiment observations. Moreover, the separation between the threshold of in-plane buckling and out-of-plane buckling is obtained.

## 5.3 Experimental work (Part 1)

### 5.3.1 AFP machine

A commercial thermoset AFP machine (Automated Dynamic Inc) located at Concordia Center for Composite (CONCOM) was used to deposit the prepreg tow on the aluminum substrate Fig. 5.1. This 6-axis articulated robot has the capability to deposit up to four prepreg tows on the tool per each course, and the tows can be cut in arbitrary lengths over the 3 inches and restarted at any time during the lay-up process. To apply compaction pressure to the incoming tapes, the AFP machine is equipped with a perforated polyurethane roller with outer diameter of 38 mm (identical to dimensions of standard roller), hardness of 60 durometer and a height deviations from the mean line of  $0.244 \mu m$ , and for heating a nitrogen hot gas torch is used. For this experiment. The material used in the current study is a 6.35mm wide CYCOM 977-2 unidirectional carbon fiber thermoset prepreg tape supplied by Bombardier inc., Canada. The prepreg fiber content is 60% by volume with a thickness of 0.17mm.

### 5.3.2 Observation of defects during the AFP process

In this research, Several AFP trials including different steering radii and process variables were performed to identify suitable parameters for obtaining appropriate experimental observations of in-plane and out-of-plane deformation and to minimize other undesirable defects at lay-ups. Accordingly, the AFP process parameters are reported in Table 5.1.

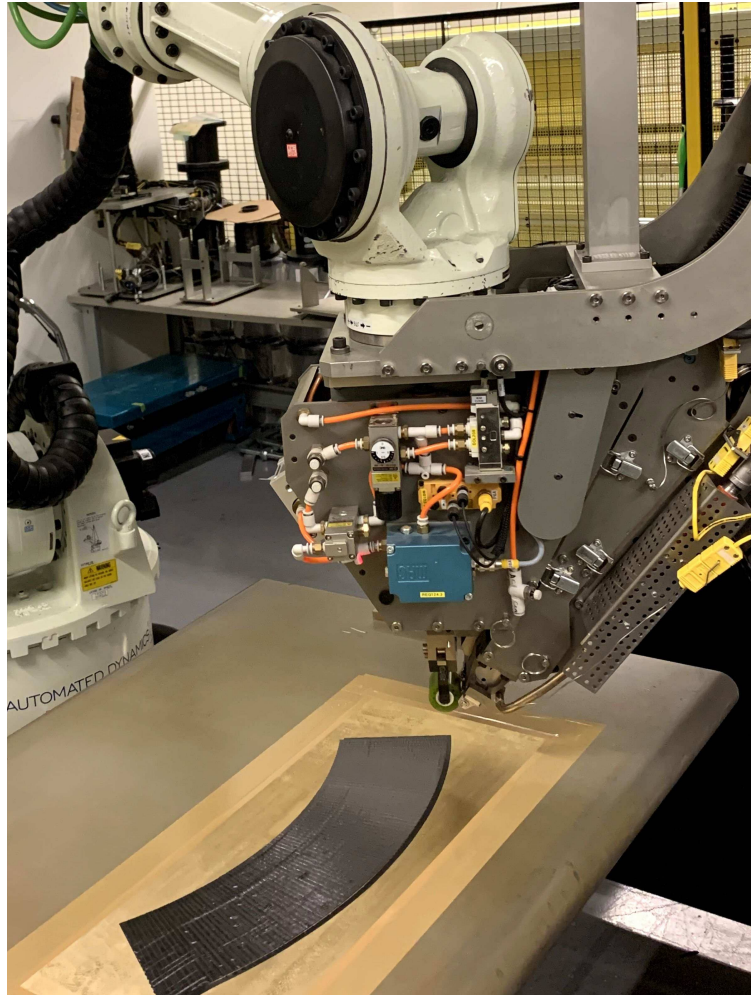


Figure 5.1: Automated Fiber Placement process.

The lay-up process with the conditions presented in Table 5.1 was run five times to make certain that the reproducibility and repeatability of the experimental observations. As it is mentioned, The mismatch length between the inner and outer edge of the towpreg in curvilinear paths leads to the planar and non-planar deformations at the towpreg. These deformations are usually in the region near to the inner edge due to the compression load created in these regions (see Fig. 5.3). Fig. 5.2 shows the planar and non-planar deformations during the AFP process.

The most important observations obtained from this experiment are outlined as follows: (1) Out-of-plane and in-plane deformations occur on the regions near to the compressive edge of the tow (inner edge). (2) In-plane deformations (waviness) can be seen in larger radii,

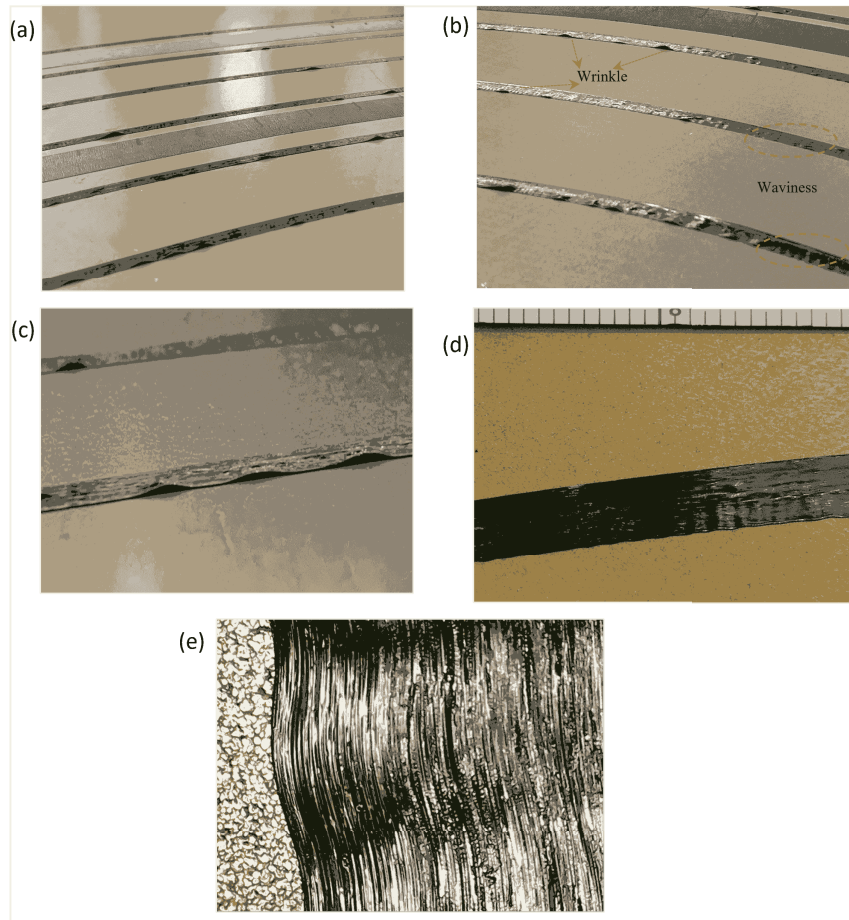


Figure 5.2: Steered tows: a) Steered tows on aluminum substrate b) Out-of-plane buckling (wrinkle) and in-plane buckling (waviness) at steered tow c) The top view Out-of-plane buckling d) The top view of In-plane buckling e) Microscopic photo of in-plane buckling.

but out-of-plane deformation starts to occur in smaller radii. (3) Out-of-plane deformations (wrinkles) are created as the first mode of buckling in the compressive side of the tow. (4) Wrinkles have the longest wavelength at the innermost edge of the tape, and as we move towards the outer edge in the width direction, the wavelength of these wrinkles decreases until it reaches zero at one point (see Fig. 5.2c). (5) The shape of the in-plane deformations is similar to the sinusoidal wave. As can be seen from Fig. 5.2d, since these deformations occur in plane, they can also create buckling in the form of higher modes. (6) The wavelength of waviness is related to the distance from the inner edge. To put it in other words, the more distance from the inner edge the less wavelength of waviness. (7) It can be seen from microscopic Fig. 5.2e that there is a slight out-of-plane deformation when in-plane waviness

occurs in tow.

## 5.4 Analytical procedure

As can be seen in experimental work and literature review, planar and non-planar deformations occur due to the mismatch of the tow length during the steering. This mismatch leads to a compressive load in the inner edge and a tensile load in the outer edge. With respect, to the geometry and experiment, we can consider that the load distribution is linearly varying in the width direction of the tow. Fig. 5.3 shows load distribution and fiber embedded in the matrix.

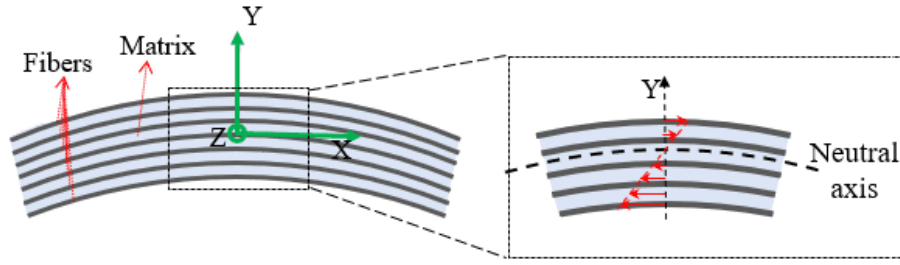


Figure 5.3: Steered tow and load distribution in width direction due to steering.

To analytically investigate waviness (fiber buckling in the  $y$ -direction) and wrinkle (fiber buckling in the  $z$ -direction), the fibers are considered as an elastic material with a circular cross-section, and the stickiness of the prepreg in  $y$  and  $z$  -directions are defined as a viscoelastic foundation. Since the stickiness of the prepreg in  $y$  and  $z$  -directions are different (the prepreg stickiness in the  $z$ -direction is measured by relaxation probe test because it occurs in a non-planar direction, and the stickiness of the prepreg property in the  $y$ -direction is measured by shear test because it occurs in planar direction) for each of them, one generalized Maxwell model (GMM) is employed to describe the relaxation modulus of the viscoelastic foundations. A schematic of fiber embedded in the matrix is illustrated in Fig. 5.4, which consists of fiber, stickiness in  $y$  and  $z$  directions as a viscoelastic foundation, and in-plane loading.

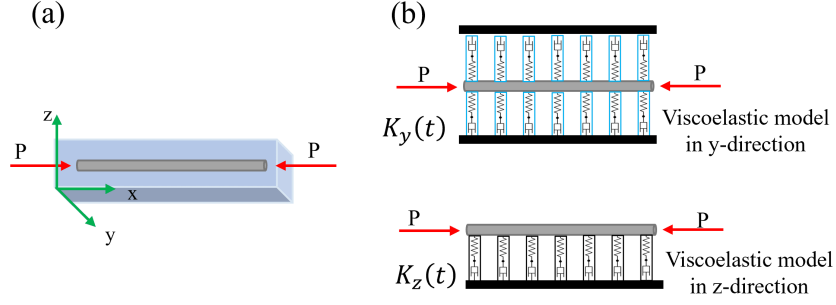


Figure 5.4: a) The model of fiber embedded in matrix b) The model of fiber buckling on a viscoelastic foundation.

### 5.4.1 Viscoelastic model of the stickiness of the prepreg

To describe constitutive equation for linear viscoelastic materials, a hereditary approach is employed according to Boltzmann's superposition principle. Based on this principle, If the arbitrary history of strain  $\varepsilon(t)$  is functionally assumed to be linear, the stress-strain relationship is formally expressed as the following form [Hajikarimi and Nejad \(2021\)](#):

$$\sigma(t) = \int_{-\infty}^t E(t-\xi) \frac{d\varepsilon(\xi)}{d\xi} d\xi = \int_{-\infty}^t E(t-\xi) d\varepsilon(\xi) \quad (51)$$

where  $\tau$  and  $E(t)$  are an integration variable and relaxation function of viscoelastic material, respectively. Generally, to interpret the relaxation modulus of viscoelastic materials such as prepreg stickiness, a physical model involving springs and dashpots can be utilized. One of the most used viscoelastic models is the generalized Maxwell model (GMM). This model is combined by several Maxwell elements connected in parallel as shown in Fig. 5.5a.

According to the differential form of viscoelasticity for each maxwell element,  $\frac{d\varepsilon}{dt} = \frac{1}{E_i} \frac{d\sigma}{dt} + \frac{\sigma}{\eta_i}$ , the relaxation modulus function of the generalized Maxwell can be written individually in analytical form of a series of exponential known as the Prony series:

$$E(t) = E_{\infty} + \sum_{i=1}^n E_i \exp\left(-\frac{t}{\tau_i}\right) \quad (52)$$

where  $E_{\infty}$  is equilibrium modulus  $E_i$  is stiffness of each spring,  $n$ ,  $t$ , and  $\tau_i$  are the number of Maxwell elements, time and relaxation time, respectively. The reason why we consider

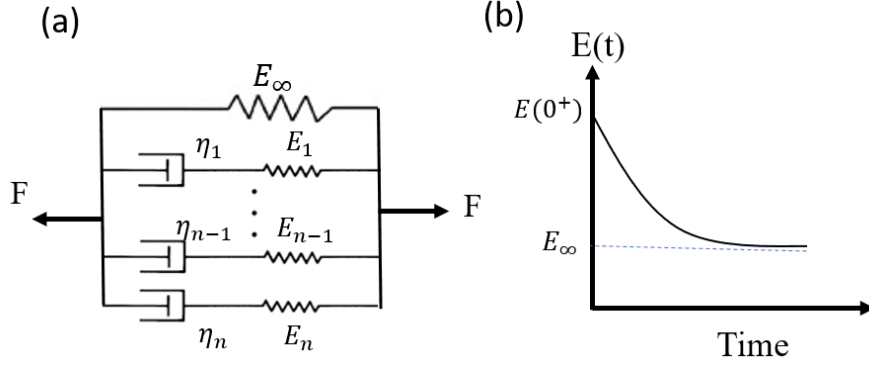


Figure 5.5: The generalized Maxwell model.

equilibrium modulus is that according to [Brinson, Brinson, et al. \(2008\)](#), the thermoset resins, unlike thermoplastics, do not tend to zero over time as will be shown in the section of Experimental (Part b) in this research. Fig.5.5b shows the relaxation modulus-time curve for the generalized Maxwell model. The relaxation modulus of time The generalized Maxwell coefficients can be determined using a curve fitting code on experiment data. In this paper, Finding the coefficients by curve fitting will be explained in the experimental work (part 2) section.

#### 5.4.2 The micro fiber-buckling model

The micro-mechanic equations for the planar and non-planar buckling of the fiber embedded in epoxy matrix can be determined respectively by equilibrium equation [s \(1973\)](#); [Timoshenko \(1970\)](#) as:

$$E_f I_f \frac{\partial^4 v(x,t)}{\partial x^4} + P_y \frac{\partial^2 v(x,t)}{\partial x^2} + \int_{-\infty}^t K_y(t-\xi) \frac{dv(x,\xi)}{d\xi} d\xi = 0 \quad (53a)$$

$$E_f I_f \frac{\partial^4 w(x,t)}{\partial x^4} + P_z \frac{\partial^2 w(x,t)}{\partial x^2} + \int_{-\infty}^t K_z(t-\xi) \frac{dw(x,\xi)}{d\xi} d\xi = 0 \quad (53b)$$

in which  $v(x,t)$   $w(x,t)$ ,  $P$ , and  $E_f I_f$  represent the deflection in  $y$ - direction,  $z$ -direction, in-plane loading ,and the effective bending stiffness of fiber respectively.  $K_{y,z}(t)$  are the relaxation coefficient of viscoelastic foundation (see Fig. 5.4 and Eq. (51)). The values

of  $K_{y,z}(t)$  are obtained in the section of Experimental work (part b). To solve Eq. (53), it is assumed that the both end of the fiber are free to rotate and as a consequence the displacement components exactly satisfying the boundary conditions can be set in the forms of:

$$\begin{aligned} v(x,t) &= \sum_{n=0}^{\infty} \phi_n(t) \sin(n\pi x/L_{f_y}) \\ w(x,t) &= \sum_{m=0}^{\infty} \phi_m(t) \sin(m\pi x/L_{f_z}) \end{aligned} \quad (54)$$

where  $\phi_{n,m}(t)$  are the transient functions according to the transient responses of the viscoelastic foundations,  $n$ , and  $m$  are the axial half-wave numbers in  $y$  and  $z$  directions, respectively. By direct substitution of  $v(x,t)$ , and  $w(x,t)$  into the Eq.(53) results in the critical buckling load for in-plane waviness in  $y$ -direction and out-of-plane wrinkle in  $z$ -direction. The dimensionless critical buckling load are found to be in the following form:

$$\mu_{n,z}^2 \left[ (E_f I_f) \mu_{n,y}^2 - P_y \right] \phi_n(t) + \int_{-\infty}^t K_y(t-\tau) \frac{d\phi_n(\xi)}{d\xi} d\xi = 0 \quad (55a)$$

$$\mu_{m,z}^2 \left[ (E_f I_f) \mu_{m,z}^2 - P_z \right] \phi_m(t) + \int_{-\infty}^t K_z(t-\tau) \frac{d\phi_m(\xi)}{d\xi} d\xi = 0 \quad (55b)$$

where  $\mu_{n,y} = n\pi/L_{f_y}$  and  $\mu_{m,z} = m\pi/L_{f_z}$ . In order to solve the buckling equation, applying the Laplace transform on Eq.(55) and rearranging it, we obtain:

$$\left( \mu_{n,y}^2 \left[ (E_f I_f) \mu_{n,y}^2 - P_y \right] + s \tilde{K}_y(s) \right) \tilde{\phi}_n(s) = 0 \quad (56a)$$

$$\left( \mu_{m,z}^2 \left[ (E_f I_f) \mu_{m,z}^2 - P_z \right] + s \tilde{K}_z(s) \right) \tilde{\phi}_m(s) = 0 \quad (56b)$$

where the notations  $\tilde{\phi}_{n,m}(s)$ ,  $\tilde{K}_{y,z}(s)$  denote the Laplace transforms of functions  $\phi_{n,m}(t)$ ,  $K_{y,z}(t)$ , and

$$\tilde{\phi}(s) = \int_0^{\infty} e^{-st} \phi(t) dt \quad (57a)$$

$$s\tilde{\phi}(s)\tilde{K}(s) = \int_0^{\infty} \int_{-\infty}^t e^{-st} K_z(t-\tau) \frac{d\phi_m(\xi)}{d\xi} d\xi dt \quad (57b)$$

Simplifying and applying inverse Laplace to Eq.(56), the transient buckling response for the  $n$ th mode is written in the form:

$$P_y = (E_f I_f) \mu_{n,y}^2 + \frac{K_y(t)}{\mu_{n,y}^2} \quad (58a)$$

$$P_z = (E_f I_f) \mu_{n,z}^2 + \frac{K_z(t)}{\mu_{n,z}^2} \quad (58b)$$

According to [Bakhshi and Hojjati \(2019\)](#); [Matveev et al. \(2016\)](#) the maximum compression load induced at the inner edge of the towpreg is related to the steering radius of the towpreg accordance with the following formula:

$$P_0 = \frac{E_1 h b}{\alpha R} \quad (59)$$

where  $P_0$  is the compressive load at inner edge of the tow,  $b$  is the width of the tow,  $h$  is the thickness of the tape and  $\alpha$  is a numerical factor related to neutral axis of the tape (See [Fig. 5.3](#)). Since the load along the width direction of the tape is assumed to be linearly varying, the load in each point along the width are found as:

$$P(y) = P_0 \left( 1 - \frac{\alpha}{b} (y + b/2) \right) \quad (60)$$

As a result, by direct substitution of Eq.(60) into Eq.(58), one obtains the critical radius for in-plane or non-planar buckling which can be time-dependent due to intrinsic viscoelasticity of the prepreg matrix. In the following sections, we experimentally characterize the

relaxation functions of viscoelastic foundations ( $K_y(t)$ ,  $K_z(t)$ ) in order to accomplish the numerical results.

## 5.5 Experimental work (Part 2)

### 5.5.1 *Identification of material characterization*

The fiber-buckling model developed in this article (Eqs. (58)) required the values of viscoelastic relaxation modulus of prepreg ( $K_y(t)$  and  $K_z(t)$ ) to obtain the model results. Since the prepreg tows show viscoelastic behavior, especially in the operating temperature of the AFP process, two appropriate test approaches are employed to characterize the relaxation modulus in the z and y directions. A tensile relaxation test is employed to measure the prepreg relaxation modulus in the z-direction (out-of-plane direction), and a shear relaxation test is used to measure the relaxation modulus in the y-direction (in-plane direction). The relaxation tests in this research were conducted using a MCR-502 Rheometer provided by Anton Paar as shown in Fig. 5.6.

#### **The relaxation modulus of prepreg stickiness in the z-direction ( $K_z(t)$ )**

To determine the relaxation modulus in the z-direction a relaxation probe test has been performed. During the test, the relaxation modulus values were recorded within the linear region. The reason for performing the test within the linear region is that the Maxwell model which is commonly used for modeling the viscoelastic foundation is based on linear viscoelasticity. It should be mentioned that the maximum relaxation modulus of the foundation (stickiness of matrix) in the z-direction occurs at the initial time ( $t=0$ ) due to the fact that there is no debonding and damage progress in the interface between prepreg tape and substrate. Thus, the relaxation probe test used is able to measure the maximum relaxation modulus of the prepreg matrix's stickiness. In this regard, to identify the buckling threshold of a steered prepreg tape, it is necessary to record the maximum relaxation modulus of the foundation. This is because if the force required for buckling exceeds the maximum force transmitted from the foundation, the prepreg (fibers) will buckle.

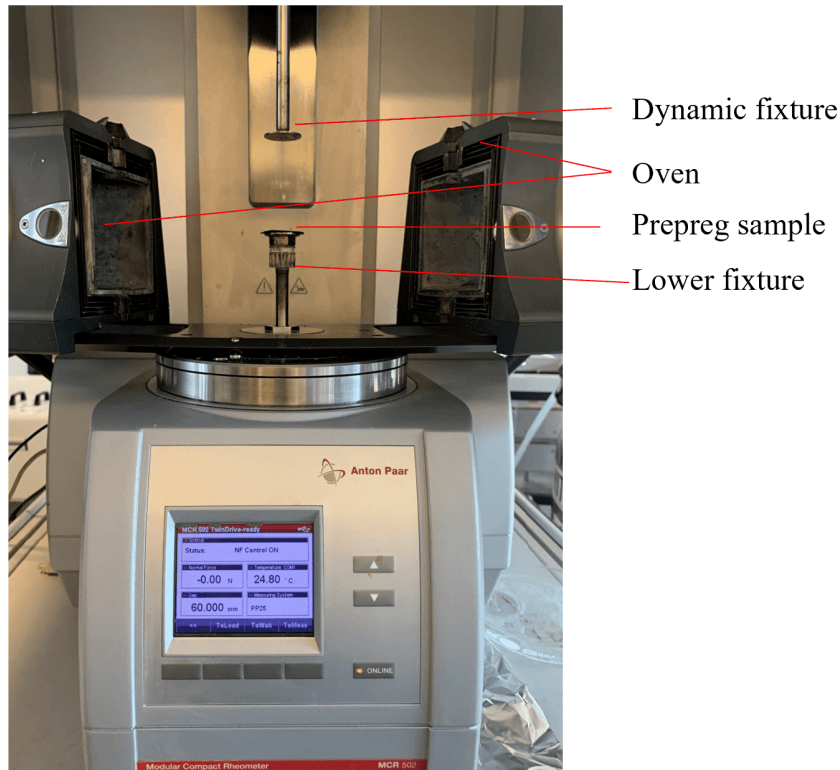


Figure 5.6: MCR-502 rheometer and prepreg sample placed on the lower fixture for relaxation test.

The relaxation probe test employed in this study to measure the relaxation modulus in the z-direction includes five successive steps: (1) the prepreg ply specimen is laid on a static aluminum fixture (lower fixture) with a diameter of 25 mm such that prevents the specimen from detaching and bending. (2) The upper probe (dynamic fixture) is pushed forward into contact with the prepreg stuck to the static fixture. (3) A downward displacement of 0.035 mm is applied to the prepreg in this step. The displacement of 0.035 mm corresponds to the thickness changes due to the pressure applied by the compaction roller during the AFP process. (4) To measure the relaxation modulus in the z-direction and stay in the linear region of viscoelasticity, a small upward displacement is applied to the upper fixture. The test results showed a value of tensile displacement of 0.02 mm (upward direction) is almost appropriate for this test to stay in the linear region. (5) The upper fixture is fixed in the new position and the values of the force are recorded for 250 seconds. Fig. 5.7 shows the

relaxation test steps in the z-direction.

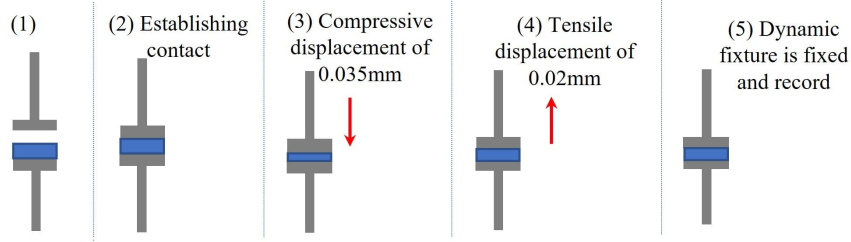


Figure 5.7: Illustration of a relaxation modulus test in the z-direction step by step performed with a rheometer.

To carry out the relaxation test, the prepreg sample was cut from the prepreg sheet with a dimension of 25 mm (the fixture diameter). The thickness of the samples was measured which is about 0.16 mm. The thickness of the samples was necessary to determine the gap between two fixtures. The temperature was controlled during the test by a convection device that surrounds the sample and both fixtures as shown in Fig. 6. According to the tack test results of [Budelmann et al. \(2020\)](#), the tack energy reaches its highest level around 40-45 °C. Since the repetition of the tests according to the work [Budelmann et al. \(2020\)](#) showed that the highest level of adhesion energy (tack energy) for our samples occurs at a temperature of 45°C, the tensile relaxation tests were performed in the temperature of 45 °C. A total of three tests were conducted in order to ensure the accuracy and repeatability of the test results. Fig. 5.8 shows the curves for the three tensile relaxation tests that were conducted repeatedly, along with the mean curve for these three tests.

As mentioned before, the determination of the generalized Maxwell model (GMM) parameters are usually inferred by curve fitting the model to the curve obtained from the tensile relaxation probe test. In this context, we find the generalized Maxwell model parameters by means of MATLAB. In Fig. 5.9, the blue curve shows the relaxation modulus-time curve for the prepreg in the z-direction obtained from the tensile relaxation test and the red curve in Fig. 5.9 shows the fitted curve for relaxation modulus. As can be seen, there is an excellent agreement between the fitted curve and the experimental data. As a result, the relaxation modulus function for prepreg in the z-direction for the process condition has the following

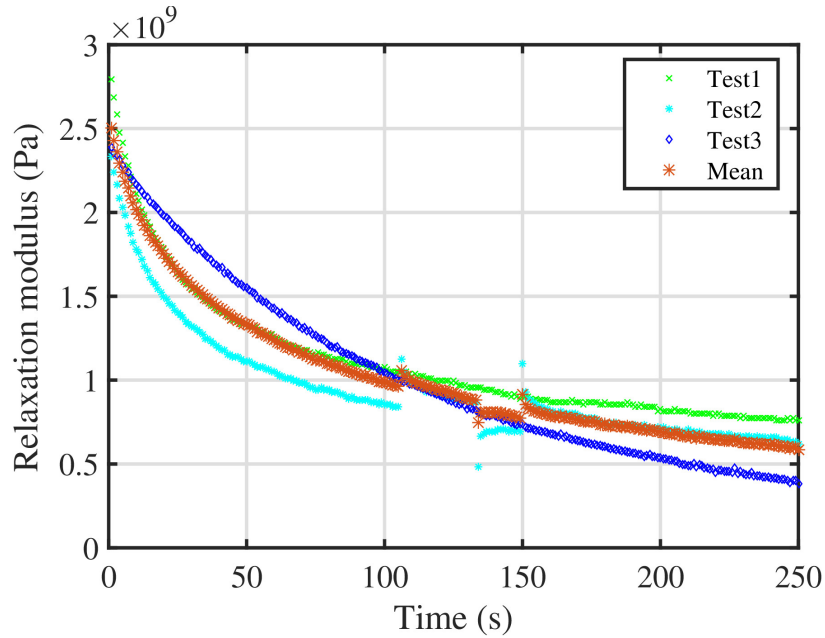


Figure 5.8: Three repeated tests and the mean value curve for the tensile relaxation test.

form:

$$K_z(t) = 1.62 \times 10^9 e^{(-0.023t)} + 8.3 \times 10^8 \quad (61)$$

### The relaxation modulus of prepreg in the y-direction ( $K_y(t)$ )

A rotational in-plane shear test is conducted using the rheometer equipment in order to measure the relaxation modulus of prepreg in the y-direction (in-plane direction). The rotational relaxation test for the prepreg is challenging due to the small thickness of the prepreg sample, making it difficult to apply shear displacement to the prepreg sample. To address the challenge, firstly, six layers of prepreg were cut and placed into the oven at a temperature of 45 °C (as mentioned in the previous section, the highest adhesion energy occurs at 45°C) for 30 seconds. The layers are then placed in a vacuum bag to ensure that the layers well stick and there is no slippage between them and also, to reach a sufficient thickness for the test. The prepared sample is cut in a circular shape with the diameter of the rheometer probe which is equal to 25 mm. Then the sample is placed on a static

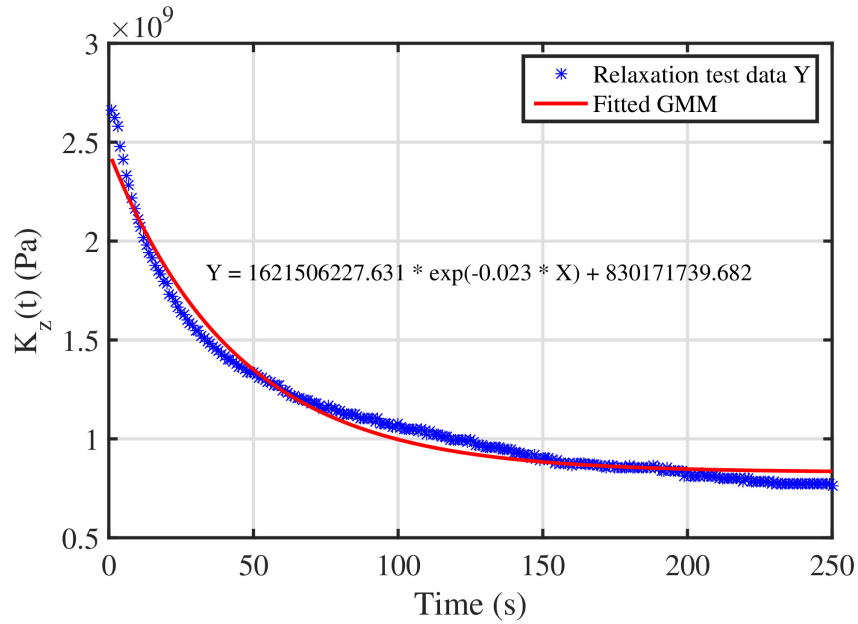


Figure 5.9: Fitting generalized Maxwell model on the relaxation modulus data in the out-of-plane direction.

fixture so as to prevent slipping, the dynamic fixture is adjusted to apply a small strain of 7 percent to the sample (the small strain is because we attempt to stay in the linear viscoelastic region). Finally, the dynamic fixture is fixed in the new position and the values of the force are recorded. A total of three tests were conducted in order to ensure the accuracy and repeatability of the test results. Fig. 5.10 displays the curves resulting from three repeated shear relaxation tests, along with the mean curve for these three relaxation tests. Fig. 5.11 shows the experimental data and the corresponding GMM fitted curve to the experimental data obtained from the relaxation test in the planar direction.

Therefore, the relaxation modulus in y-direction can be written in the following form:

$$K_y(t) = 42355.5 + 1.8 \times 10^6 e^{(-0.02t)} \quad (62)$$

## 5.6 Numerical results and discussion

In order to illustrate the general buckling behaviour of the fiber embedded in matrix, we solve buckling problem by replacing the experimental values of  $k_y(t)$  and  $k_z(t)$  from Eqs.(61)

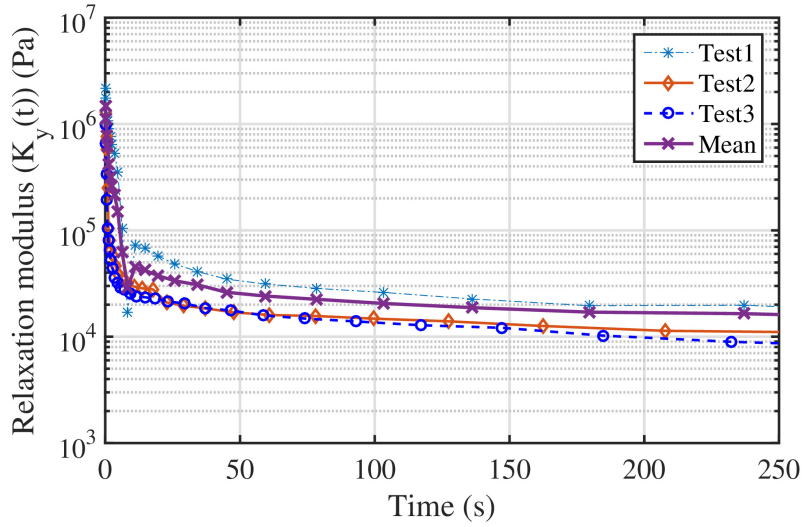


Figure 5.10: Three repeated tests and the mean value curve for the shear relaxation test.

and (62) into Eq.(58). Mechanical material properties which are used in calculations are as follows:

$$\begin{aligned}
 E_f &= 275 \text{ GPa}, d_f = 10 \mu\text{m}, E_1 = 31 \text{ GPa}, b = 6.35 \text{ mm}, \\
 h &= 0.17 \text{ mm}, I_f = 1/64\pi d^4
 \end{aligned}
 \tag{63}$$

### 5.6.1 Transient response of fiber buckling in y and z directions

Given the GMM presented for viscoelastic properties of prepreg stickiness both in z and y directions, buckling responses are classified into several types: fiber-buckling can occur immediately after placing the tape by compaction roller. This buckling load is attributed to the value of relaxation function in the first moment ( $K_{y,z}(0^+)$ ) which is called the upper critical buckling load (See Fig. 5.5b). In addition, fiber can buckle after the relaxation happens in prepreg modulus which can be ascribed to the value to which the relaxation function tends over time ( $K_{y,z}(\infty)$ ). The relaxed buckling load is referred to the lower critical buckling load. Fig. 5.12 shows upper and lower critical buckling loads and critical radii for the wrinkle formation:

The most interesting results from Fig. 5.12 are found as follows:

For out-of-plane buckling (Fig. 5.12a and 5.12b):

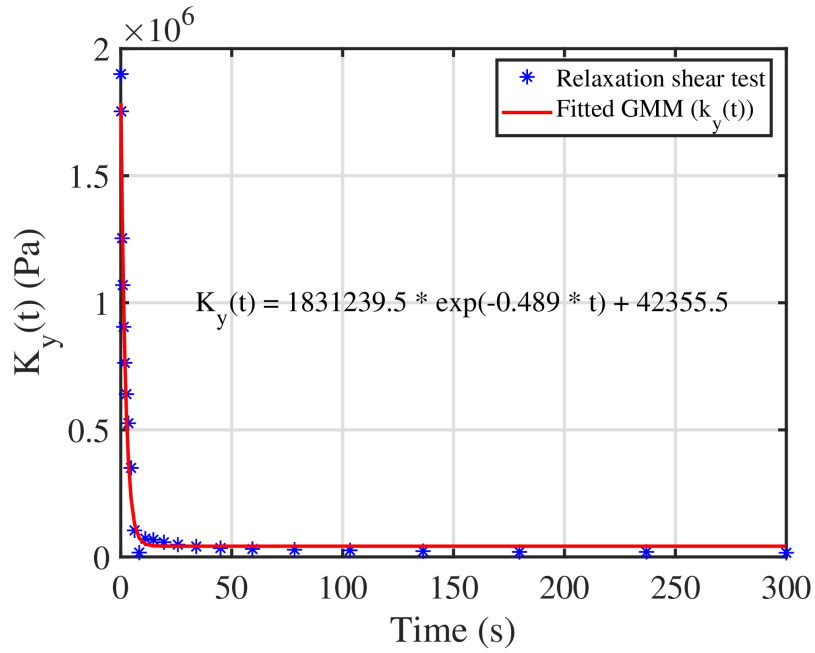


Figure 5.11: Fitting generalized Maxwell model on the relaxation modulus data in in-plane direction.

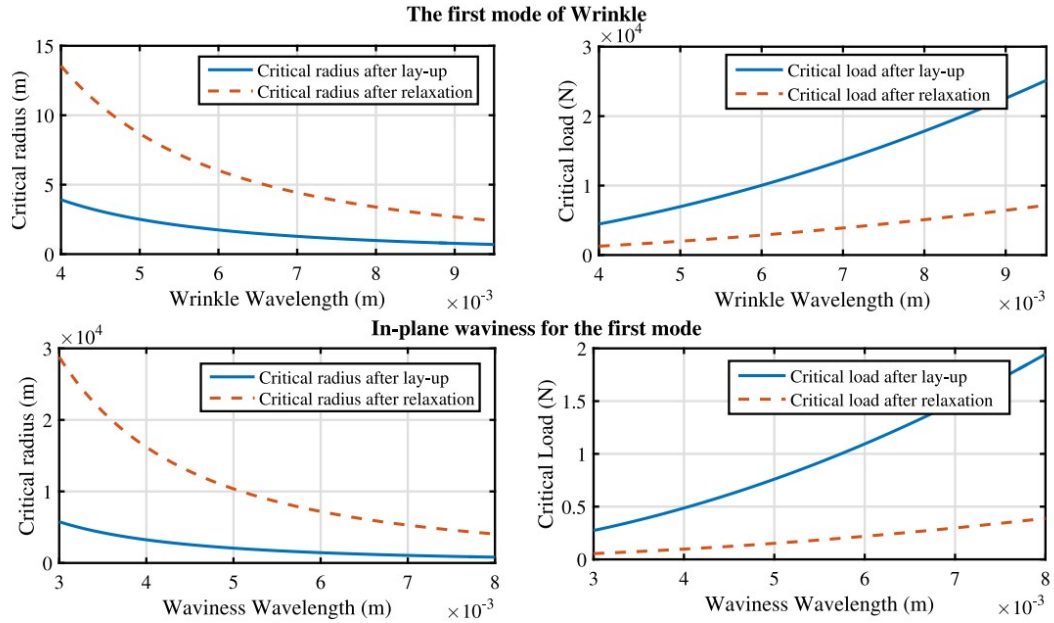


Figure 5.12: Upper and lower critical buckling load and radius for out-of-plane buckling and in-plane buckling.

- (1) The significant point to mention is that on the one hand, due to the geometry, non-planar deformations (wrinkles) occurs in the first buckling mode ( $m = 1$ ) corresponding to the lowest load for short beams and rods.
- (2) Since the highest value of the viscoelastic foundation is right after placing the tow, the buckling load is the highest at the initial moment, and due to the viscoelasticity of prepreg stickiness, the buckling load decreases with increasing time.
- (3) Unlike buckling load for a dry fiber without elastic foundation, taking the viscoelastic foundation into account causes the fiber-buckling load increases with an rise in wavelength. This can be due to the fact that increasing the wavelength leads to an increase in the force applied to the fiber through the viscoelastic foundation.
- (4) According to the above-mentioned as the second point, this model can properly describe the shape of the wrinkle in tow (see Fig.5.2). In other words, the experimental observations shows that the wavelength of the wrinkles decreases almost polynomially along the width to reach to zero, and the mathematical results indicate the same decreasing trend.

For in-plane buckling (Fig.5.12c and 5.12d):

- (1) The changes of the first mode of in-plane buckling versus wavelength is similar to that of out-of-plane buckling.
- (2) A big difference between the values of planar and non-planar buckling loads is due to the lower value of viscoelastic relaxation in y direction (planar direction). The smaller value of relaxation modulus leads to the fact that the waviness occurs at very large values of the radius. (comparing Fig. 5.12a and 5.12c)

Besides, the model results presented in Fig. 5.12 show that the wrinkles start to form in the tape at much smaller radii compared to the waviness formation in the prepreg tow. This aligns with the experimental observations outlined in Section 2, which show that wrinkles appear on a steered tape after a critical radius.

As mentioned before and observed in the AFP trials, the in-plane buckling may occur at tow in different buckling mode due to the lack of restriction in y-direction. Accordingly, Fig. 5.13 shows different buckling modes for in-plane waviness. It can be seen from Fig. 5.13 that the high values of the relaxation function of prepreg stickiness (larger than  $E_f I_f$ , see Eq.(58)) results in a decrease in the buckling load for the higher values of mode shapes.

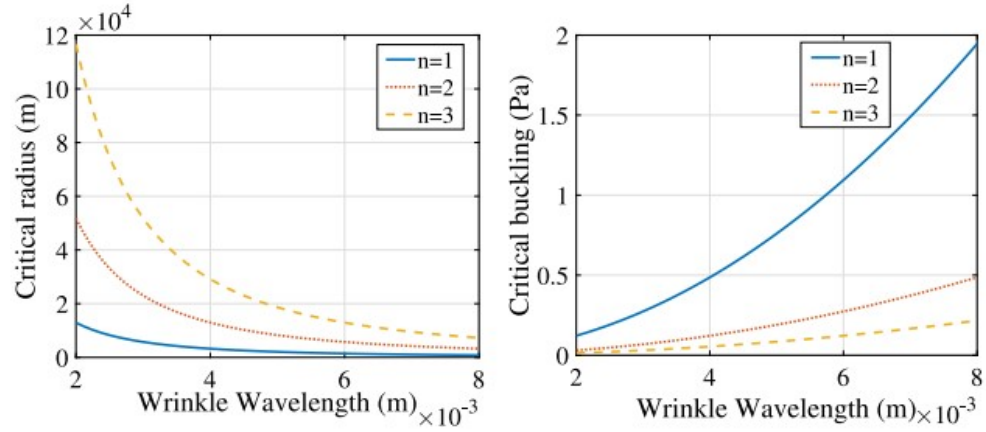


Figure 5.13: Critical buckling load and radius for the three different mode shapes of in-plane buckling (waviness).

### 5.6.2 Prediction of wavelength changes in-width direction in a steered tow

The previous models summarized in literature review considered the out-of-plane buckling as a buckling of a plate. Therefore, these model could not to predict the wavelength changes at a steered tow in width direction as shown in Fig. 5.14. In this research, a new model for in-plane and out-of-plane deformations is developed as fiber buckling instead of plate buckling. This model is perfectly capable of capturing the wavelength changes of out-of-buckling. To validate the proposed approach, the wavelength changes of the wrinkle are measured for a steered tow with radius of 75 *cm* in width direction. The shape of the wrinkle in width direction, the wavelength changes, and neutral axis position are shown in Fig. 5.14. In this regard, the experimental and proposed model results for wavelength changes

Table 5.2: wavelength changes of wrinkles in the width direction.

y-Coordinate (mm)	Analytical wavelength (mm)	Experiment wavelength (mm)
0	9.15	9
1	8	8.1
1.5	7.4	7.2
2	6.7	6
2.5	6	5.1
3	5.4	4.4
3.5	4.6	3.7

of wrinkle are presented in Table 5.2. It can be seen that the proposed model attains acceptable and approximately similar results with experimental data. It should be mentioned that the value of the  $\alpha$  corresponding to neutral axis is considered to be  $\alpha = 1.2$ . This value is obtained by finding the neutral axis from experimental observation (the neutral axis is the first fiber in the tow that does not buckle).

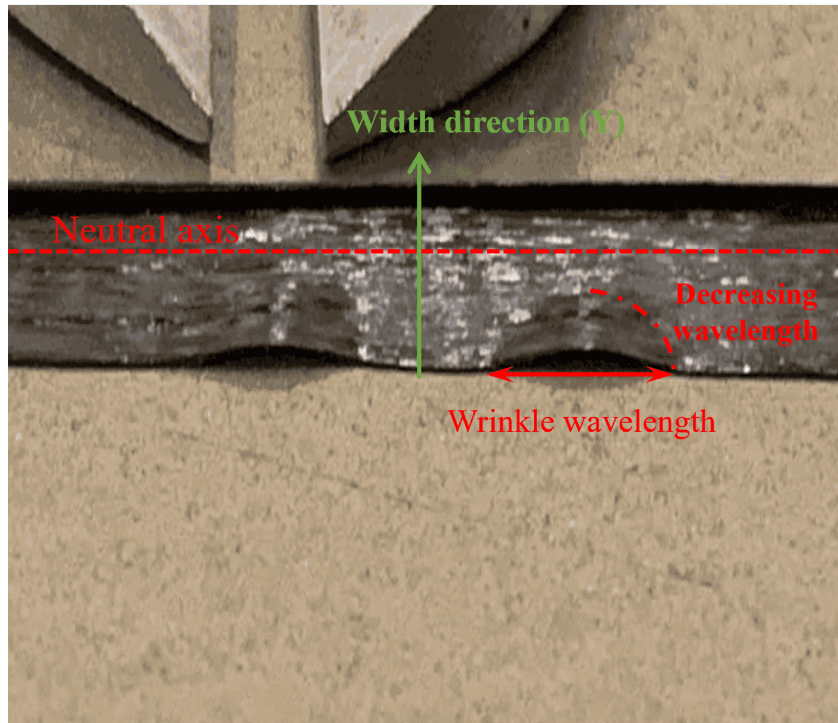


Figure 5.14: Top view of wrinkle shape with neutral axis position and wavelength changes.

A slight difference between experimental and micro-mechanical model results can be traced back to the inaccurate mechanical properties of prepreg, the stickiness of prepreg, and

initial imperfections at the tape. For example, there is no standard or experimental method to measure the relaxation of the steered prepreg stickiness. Also, the values presented for the elastic modulus of a unidirectional prepreg are different.

### 5.6.3 The effect of relaxation modulus of the prepreg and length of the fiber on critical load

The critical load is plotted as a function of the length of the fiber and the relaxation modulus. This yields the surface plot depicted in Fig. 5.15. The resulting surface illustrates that the critical buckling load rises with increasing the length of the fiber and relaxation modulus. The reason why the buckling load increases with an increase in the length of the fiber is that as the length of the fiber increases, the force exerted to the fiber by the viscoelastic foundation (the stickiness of the resin matrix) becomes stronger which in turn leads to an increase in the buckling load.

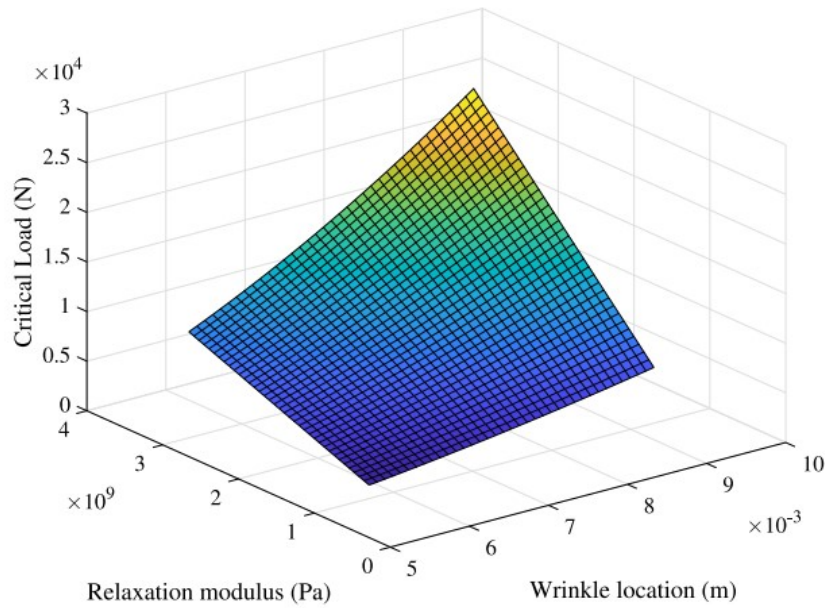


Figure 5.15: The values of critical load over the length of the fiber before buckling and relaxation modulus.

#### 5.6.4 The effect of mixed mode in in-plane waviness

As aforementioned in the literature review, a rod on an elastic foundation may buckle into a helical form when two different buckling modes of a rod occur simultaneously [Su et al. \(2014\)](#). It was seen from the microscopic observation presented in Fig. 5.2e in experiment section (Part 1) that a slight out-of-plane buckling occur when the fiber buckle into the plane (in the y-direction). This means that the buckling load of the  $n$ th mode is equal to that of the  $(n+1)$ th mode. In this regard, we determine for what the values of relaxation modulus two successive buckling loads are equal ( $\Delta P_{cr} = 0$  or  $P_{cr_{n+1}} - P_{cr_n} = 0$ ), to put it simply, mixed mode occurs at tow. These specific values of relaxation modulus are resulted from Eq.(64) as follows:

$$\begin{aligned}
 \Delta P_{cr} = 0 &\Rightarrow P_{cr_{n+1}} - P_{cr_n} = 0 \\
 &\xrightarrow{\text{From Eq.(58)}} \left( \frac{E_f I_f \pi^2 (n+1)^2}{L_{fy}^2} + \frac{L_{fy}^2 K_y(t)}{\pi^2 (n+1)^2} \right) - \\
 &\left( \frac{E_f I_f \pi^2 (n)^2}{L_{fy}^2} + \frac{L_{fy}^2 K_y(t)}{\pi^2 (n)^2} \right) = 0 \\
 &\Rightarrow K_y(t) = \frac{E_f I_f \pi^4}{L_{fy}^4} (n+1)^2 (n)^2
 \end{aligned} \tag{64}$$

Fig. 5.16 shows the dependency of the difference between two successive buckling load  $\Delta \bar{p}$  as a function of  $\bar{k}_y(t)$ . where  $\Delta \bar{p}_{cr} = \frac{\Delta P_{cr} L_{fy}^2}{\pi^2 E_f I_f P_{cr_n}}$ , and  $\bar{k}_y(t) = \frac{K_y(t) L_{fy}^4}{\pi^4 E_f I_f}$ .

The intersections of the curves with the x-axis indicate the values of relaxation functions in which two different buckling mode shapes of  $n$ th and  $(n+1)$ th occur simultaneously. This phenomenon leads to an interaction between two mode shapes which in turn creates a slight deformation in the out-of-plane direction. It is worth mentioning that  $\Delta \bar{p}_{cr}$  dramatically decreases as  $\bar{k}_y(t)$  increases in value. As a result, with respect to the high value of the relaxation modulus of prepreg stickiness in the y-direction, it is expected that there will be a small amount of out-of-plane deformation in the fiber that buckles in plane (y-direction) as observed in Fig. 5.2e.

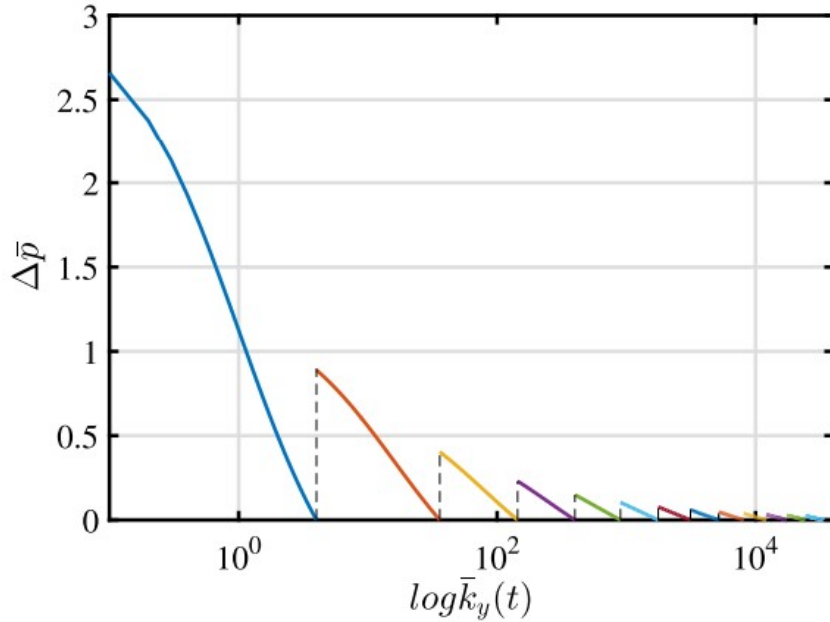


Figure 5.16: Normalized two successive buckling loads versus the relaxation modulus for in-plane buckling (waviness).

## 5.7 Conclusion

Through a combination of experiments and theoretical study, the buckling behavior of the uncured thermoset prepreg during the steering process has been investigated. First of all, we experimentally studied deformations of a steered prepreg to gain a deeper understanding concerning the out-of-plane and in-plane deformations. The experimental observations showed that fibers pre-impregnated with the uncured thermoset resin can buckle into both planar and non-planar configurations at a steered prepreg. It was also observed that although the concept of planar and non-planar deformations is similar in a steered tape, the possibility of planar buckling is higher than non-planar buckling in a tape. In addition, observations showed that the probability of non-planar buckling increases with a decrease in the steering radius. Besides, the additional inspection (microscopic pictures) showed that a slight wrinkling was observed when in-plane waviness occurs in the tow (Fig. 2e).

A new micro-mechanic approach has been employed to account for the experimental observations mentioned in the previous paragraphs and to model in-plane and out-of-plane

deformation behaviors of the fibers at a steered tow. Therefore, in the presented method, we have considered fiber as an elastic material and Since the uncured prepreg behaves as a viscoelastic material, the the adherence of uncured matrix of prepreg is modeled as a viscoelastic foundation to account for the viscoelastic effects on the buckling response of the tow. The viscoelastic properties of the uncured matrix in out-of-plane and in-plane directions have been measured using a probe relaxation test and a rotational relaxation test using a rheometer machine. Since the adherence of the matrix is different in out-of-plane and in-plane directions, two generalized Maxwell models with different parameters have been adopted for each direction using curve fitting. By experimentally measuring the viscoelastic relaxations and inserting them into the fiber-buckling equation, the deformation behavior of the fiber in non-planar and planar directions has been obtained. Our analytical results are completely able to predict the critical buckling load and radius for in-plane and out-of-plane configurations. Moreover, the model results of the wavelength changes of the non-planar wrinkle in the width direction are in a excellent agreement with experimental observations. In addition, the proposed model is capable of separating between the buckling threshold of planar and non-planar deformations at tow. Besides, using the presented approach in this research, we specified the values of prepreg modulus that two critical buckling loads could occur simultaneously and describe why there is a slight wrinkling when planar buckling occurs during the steering.

As for future work, we intend to develop the test methods for characterizing the viscoelastic properties of the prepreg matrix. In addition, future work focuses on the effect of process parameters including temperature, pressure, and curvature radius on prepreg stickiness as a main factor in preventing the formation of defects. For the theoretical part, the proposed approach will be extended by taking the other parameters into account, and the experiment and model results also will be compared with the finite element models.

## Chapter 6

# The effect of automated fiber placement process parameters on interlaminar shear strength of uncured prepreg bonded samples

This work has been submitted in:

Kheradpisheh, Meisam, Yas, Amir Hafez and Mehdi Hojjati. "The effect of automated fiber placement process parameters on interlaminar shear strength of uncured prepreg bonded samples." *Journal of Composites Science* (Published).

### 6.1 Abstract

The effects of automated fiber placement (AFP) parameters on the inter-laminar bonding between the uncured thermoset prepreg tapes were investigated using a systematic series of experiments and FE analysis. The goal was to optimize inter-laminar bonding during the AFP lay-up process and provide a model for the interlayer bonding of uncured prepreg

tapes during this process. The shear strength of the interfacial bonding plays a pivotal role in the formation of planar and non-planar deformations during the automated fiber placement (AFP) process. The quality of this bonding has a significant effect on the quality of the manufactured parts. Besides, the bonding strength is interconnected with various AFP process parameters including compaction roller, feed rate, temperature, and dwell time. Hence, a systematic series of experimental studies are conducted to investigate how changes in process parameters affect the shear strength of single lap joint (SLJ) specimens produced under various process conditions. To fabricate the single-lap joint samples under different conditions, an in-house setup was developed to simulate the AFP process allowing us to control compaction force, feed rate, temperature, and dwell time during the process. The experimental results of the single lap joints indicate that the shear strength of the bonded prepreg tows is significantly influenced by the interaction among the process parameters rather than by their individual, isolated effects. Moreover, the responses of prepreg SLJs are simulated using the FE method. Through the comparison of numerical and experimental results, it will be clearly shown that the developed FE framework can act as a reliable approach for modeling the bonding layer between prepreg tapes.

## 6.2 Introduction

The automated fiber placement (AFP) process is an advanced manufacturing technology that is widely used in industries such as automotive, and aerospace, thanks to the high productivity, cost-effectiveness, precise fiber placement, and low wastage. Besides, carbon fiber thermoset prepreg tapes are used as a raw material in the thermoset AFP process proves to be a viable substitute for the traditional materials by offering a high stiffness and strength, corrosion resistance, and chemical resistivity.

In the AFP process for creating a composite part, the initial step involves placing the multiple adjusted prepreg tows to create a course. Then, these courses are positioned in a predetermined sequence to form a ply. The progressive layering of plies, with each ply placed next to and on top of each other, leading to the formation of laminate. This manufacturing

process is performed using the robotic head of the AFP machine that precisely controls the placement of the prepreg materials on the substrate. The head of the machine is mounted on a six degrees of freedom system which provides accurate movement in various directions. This machine's head is equipped with a guidance system that directs the prepreg tow by providing proper tension from the spool to the tip of the head where both the compaction roller and the heat source are positioned. In this stage, the pressure and heat are applied to the prepreg tapes to adhere them onto the substrate. The quality of the product manufactured by the AFP robot is notably influenced by their adhesion to the substrate, the adhesion between the prepreg tape and substrate is also known as prepreg tack. Insufficient adhesion or prepreg tack may lead to the formation of defects such as gap, overlap, in-plane, and out-of-plane buckling during the AFP process [Budelmann et al. \(2019, 2020\)](#); [Fereidouni and Hoa \(2024\)](#). To determine the effect of prepreg tack on defect formation, several studies have developed analytical models that investigate the adhesion between the prepreg and the substrate. In these models, the prepreg is treated as a plate supported by an elastic foundation, which represents the prepreg tack. The elastic foundation is modeled using normal and shear springs, as depicted in [Figure 6.1](#). By deriving the equilibrium equations, these models show that in-plane and out-of-plane defects are related to the shear and normal stiffness of the elastic foundation, and higher values of  $K$  and  $G$  prevent defect formation during the lay-up process. Since such defects persist after curing and diminish the quality of the final part, minimizing and eliminating them is essential for enhancing part quality (for more details see [Beakou et al. \(2011\)](#); [Belhaj and Hojjati \(2018\)](#); [Kheradpisheh and Hojjati \(2023\)](#)). Besides, a source of gaps and overlaps in the automated manufacturing of composites is the misalignment between adjacent tows caused by placement head positioning errors. The combination of computer errors with the increase in the width of the prepreg can increase the generation of overlap and gaps in the manufacturing process. This occurs because AFP software accounts for a specific tape width during lay-up and any deviation—whether an increase or decrease—from that specified width can lead to the formation of gaps and overlaps.

The quality of the prepreg's stickiness to the substrate can be attributed to the material's

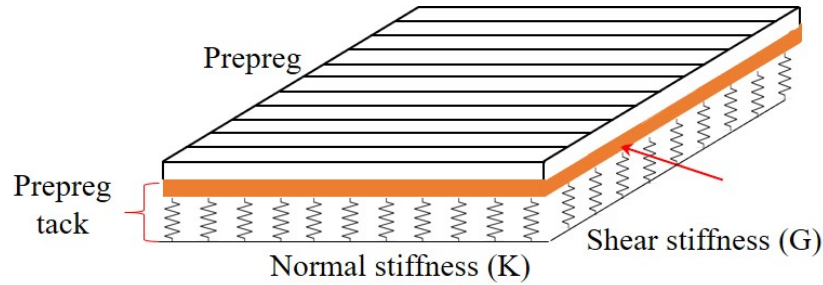


Figure 6.1: A schematic of prepreg tape model as a composite plate on Pasternak foundation.

aging which is investigated in [Dubois, Le Cam, and Beakou \(2010\)](#); [Ji et al. \(2002\)](#); [A. Smith et al. \(2020\)](#); [A. W. Smith and Hubert \(2023\)](#). The work in [Dubois et al. \(2010\)](#) studied the normal stickiness of prepreg tape under different aging conditions. Investigating the impact of humidity, time, and temperature on prepreg tack in the normal direction was carried out through a probe test. In [Ji et al. \(2002\)](#), the quality of the prepregs was investigated under different environmental conditions. Various experimental methods, including differential scanning calorimetry (DSC), thermal analysis (TA), and infrared spectroscopy (IR) were employed to evaluate the performance of prepreg material during the storage time. Smith et al. [A. Smith et al. \(2020\)](#); [A. W. Smith and Hubert \(2023\)](#) examined the evaluation of the prepreg tack over a span of up to 375 days of environmental aging. The authors in [Grunenfelder and Nutt \(2012\)](#) studied the effect of room-temperature aging on the glass transition temperature and degree of cure using the DSC test. The results show that aging reduces the performance of the prepreg materials.

In addition to aging, the stickiness of the prepreg tapes can still be influenced by various AFP process parameters, including pressure, dwell time, temperature, and feeding rate [Belhaj et al. \(2021\)](#). As mentioned earlier, the inadequate stickiness of prepreg to the substrate may lead to the occurrence of defects at prepreg tape during the lay-up process. For example, insufficient tackiness in the steering process, which is the placing of tow in a curvilinear path, forms in-plane and out-of-plane buckling defects in the inner edge of the tape. As previously mentioned, the insufficient adhesion of the prepreg to the substrate can result in the occurrence of defects in the prepreg tape during the lay-up process. For instance,

insufficient tackiness in the steering process, where the tow is placed in a curvilinear path, can lead to in-plane and out-of-plane deformations in the inner edge of the tape [Belhaj and Hojjati \(2018\)](#); [Kheradpisheh and Hojjati \(2021\)](#); [Matveev et al. \(2016\)](#). Therefore, investigating the impact of the process parameters on the stickiness of the prepreg is significant in enhancing its adhesion and minimizing the formation of defects. In this context, the authors [R. Crossley et al. \(2012\)](#); [R. J. Crossley et al. \(2013\)](#) designed a novel peel test apparatus to quantify the prepreg tack in the normal direction (90 degrees). This test setup facilitated the simulation of the AFP process, allowing them to record peel resistance and study the effect of feed rate and pressure on the peel resistance of the prepreg materials. [Budelman et al. \(2019\)](#) employed rheometer equipment to measure the stickiness of the prepreg in the normal direction using the probe tack test. The temperature was adjusted using a convection oven, while the pressure, dwell time (compaction period), and debonding rate were controlled through the dynamic probe fixture of the rheometer. They showed that around 40 °C is the optimal temperature for achieving the highest tack energy. Furthermore, their results indicated that an increase in the debonding rate led to a rise in the maximum tack stress. In [Belhaj et al. \(2021\)](#) the effect of process parameters, including temperature, pressure, and feed rate, on prepreg tack was assessed through peel-off tests. They utilized the Taguchi method to optimize and streamline the experimental design, reducing the number of required trials.

In addition to examining the influence of process parameters on stickiness in the normal direction, it is crucial to investigate their effects on stickiness in the shear direction. This consideration is essential due to the rolling of the roller and the steering process of the prepreg, generating an in-plane force at the prepreg tape and inducing movement on the substrate in the shear direction [Belhaj and Hojjati \(2018\)](#); [Y. Wang et al. \(2020\)](#). The effect of the shear modulus on the formation of wrinkle defects in the AFP process was demonstrated through a mathematical approach in [Belhaj and Hojjati \(2018\)](#). In their buckling model developed for wrinkle formation, they accounted for the impact of the shear layer by incorporating it into the elastic foundation. The in-plane shear response of uncured prepreps was investigated in the work presented by [Y. Wang et al. \(2020\)](#) using a

10° off-axis tensile test, then, a viscoelastic model was presented for modeling the calculated in-plane shear modulus in [Y. Wang et al. \(2021\)](#). The authors in [Mohan, Alshahrani, and Hojjati \(2016\)](#) carried out an experimental study to find the inter-laminar shear behavior of the uncured prepreg tapes by means of  $\pm 45^\circ$  tensile test. In addition, the impact of the temperature, the number of layers, and the tensile rate on inter-laminar shear behavior were presented. Inter-laminar friction properties of uncured thermoset prepregs and dry prepregs through a novel tensile friction test were studied in [Erland, Dodwell, and Butler \(2015\)](#); [Rashidi, Montazerian, Yesilcimen, and Milani \(2020\)](#). The work in [Venkatesan et al. \(2023\)](#) investigated the effect of AFP process parameters on the mechanical properties of thermoplastic prepregs. The research employed four-point bending and single-lap joint tests to assess these mechanical properties under different process conditions.

Previous research on prepreg tack (adhesion between prepreg and substrate) has largely concentrated on their normal separation. However, the analytical models suggest that inter-layer shear properties are critical for minimizing defects in thermoset AFP manufacturing (see [Figure 6.1](#)). Therefore, optimizing AFP process parameters to enhance the bonding of prepreg tape is crucial for achieving high-quality manufactured structures. This study aims to extensively investigate the inter-layer shear behavior of uncured thermoset prepreg tapes under various process parameters including temperature, compaction roller, lay-up speed, and contact time. For this purpose, single-lap joint (SLJ) prepreg samples were fabricated and tested under these varying conditions to assess shear strength and determine the optimal processing conditions. In this context, a cohesive zone model-based FE analysis was developed to simulate SLJ sample responses, providing stress distributions and bonding layer behavior under various conditions. Moreover, microscopic and geometric analyses were also performed to provide a deeper understanding of shear behavior in bonded uncured prepreg tapes.

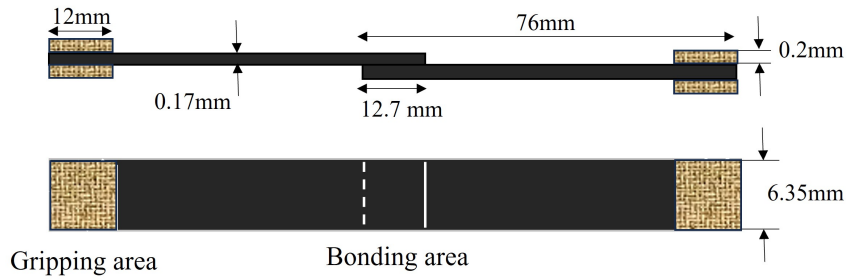


Figure 6.2: Schematic of single-lap joint unidirectional prepreg specimen with dimensions

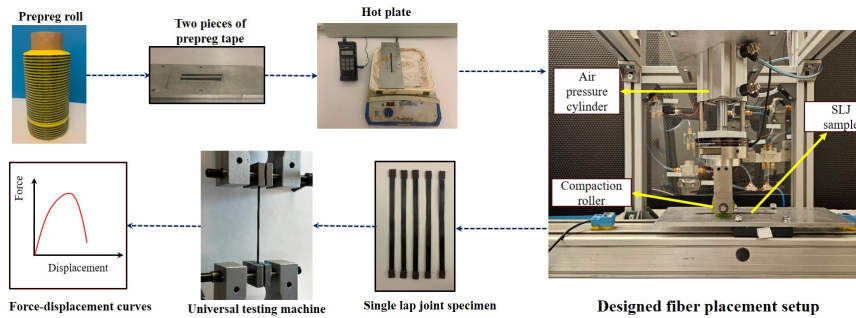


Figure 6.3: The manufacturing procedure of the Single lap joint specimen

## 6.3 Materials and manufacturing procedure

The material used for the fabrication of the single lap joint samples was an uncured thermoset unidirectional carbon fiber/epoxy prepreg tape (CYCOM 977-2) supplied by Bombardier Inc. in Canada. The thermoset prepreg tapes have a 6.35mm width and 0.17mm thickness and contain 60 % fiber content by volume.

### 6.3.1 Sample preparation

In the current work, due to the absence of an ASTM standard specifically designed for measuring the shear strength of prepreg tapes, ASTM D5868 was utilized for the preparation of the SLJ samples, with some adjustments made to the specimen dimensions. The schematic shown in Figure 6.2 provides a visual representation of the configuration of the specimens. Since the matrix of the uncured prepreg creates a bond between the two pieces of prepreg, there is no need for additional adhesive (see Figure 6.2).

The creation procedure of single lap joint samples begins with the cutting of two pieces

of prepreg from a prepreg roll that has been kept at room temperature for a duration of two hours. These uncured prepreg pieces are then positioned on an aluminum substrate, ensuring a 12.7 mm (0.5 Inch) overlap. Then, a hot plate is used to control the temperature of the SLJ samples. In the next step, a designed automated fiber placement (AFP) setup is utilized which is capable of changing pressure and feed rate values during the sample preparation. As shown in Figure 6.3, the AFP setup utilizes an air cylinder connected to a load cell to precisely control the force applied to the compaction roller. The compaction roller is held by an air jack attached to a steel bracket providing stability and facilitating vertical motion. For the horizontal movement, the system is equipped with a ball screw linear guide, which allows the aluminum plate to move at variable speeds beneath the compaction roller. After applying pressure at different velocities, the tabs are attached to the samples in the gripping area and subsequently, a universal testing machine is employed to conduct quasi-static single-lap shear tests for assessing the shear strength of individual specimens. During these tests, the SLJ samples were subjected to a constant displacement rate of 1.5 mm/min. To guarantee accuracy and reproducibility in the test outcomes, four tests were conducted for every sample. Figure 6.3 shows the whole manufacturing procedure of single-lap joint bonded with prepreg adherents.

Since this research investigates the effects of four process parameters: temperature, pressure, feed rate, and dwell time on the inter-laminar shear strength of the uncured prepreg tape, with regard to the experiment's limitations, we systematically considered different levels for each parameter to explore their effects:

(i) For the pressure parameters: Two common compaction rollers were employed: (1) a polyurethane roller (PUR) with 60 durometer hardness and (2) a stainless-steel roller (SSR). Each roller was subjected to two distinct loads: 225 N and 289 N, representative of typical loads during the thermoset AFP process. This resulted in four different pressure levels, calculated by dividing the applied load by the contact area created by the roller under the applied load. As a result, the PUR roller generated pressures of 0.8 MPa and 0.83 MPa, while the SSR roller produced pressures of 4.2 MPa and 5.5 MPa. Figure 6.4 shows the rollers and their contact area traced on pressure film and the values of pressure.

Table 6.1: [Process parameters' levels for fabrication of single-lap joint samples](#)

Parameters	Type of roller	Levels	
Pressure	PUR	0.8 MPa and 0.83 MPa	
	SSR	4.2 MPa and 5.5 MPa	
Feed rate	For both roller	15, 35, 55 and 80 mm/s	
Dwell time	PUR with pressure of	0.8 MPa	0.53, 23, 14, 0.1 second
		0.83 MPa	0.67, 28, 18, 0.15 second
	SSR with pressure of	4.2 MPa	0.1, 0.04, 0.02, 0.018 second
		5.5 MPa	0.1, 0.04, 0.02, 0.018 second
Temperature	For both roller	25 and 45 degree Celsius	

(ii) For the Temperature Parameter: Due to measurement limitations and the low operational temperature, two levels were considered for the temperature: (1) room temperature, approximately 25 degrees Celsius, and (2) a higher temperature [of around](#) 45 degrees Celsius, which corresponds to the point where the adhesive bonding between prepreg and substrate is maximized [Budelmann et al. \(2019\)](#).

(iii) For the feeding rate: Three different speeds including 15mm/s, 35mm/s, and 55mm/s were selected for the feeding rate parameter.

(iv) For the dwell time (compaction period): As mentioned in the last paragraph of the introduction section, we define dwell time as the amount of time during which each point of tape is beneath the roller. Thus, it is a function of both contact area and pressure and can be calculated by dividing the length of the contact area in the direction of movement by the feeding rate, [as expressed in the following equation](#):

$$Dwell\ time = \frac{Contact\ length}{Feed\ rate} \quad (65)$$

[For a better understanding of the experimental conditions, the process parameters, compaction roller types, and levels of each parameter are summarized in Table 6.1](#)

## 6.4 Experimental results and discussion

In this section, the force-displacement curves are plotted for specimens manufactured under various process conditions. Moreover, the influence of process parameters on the

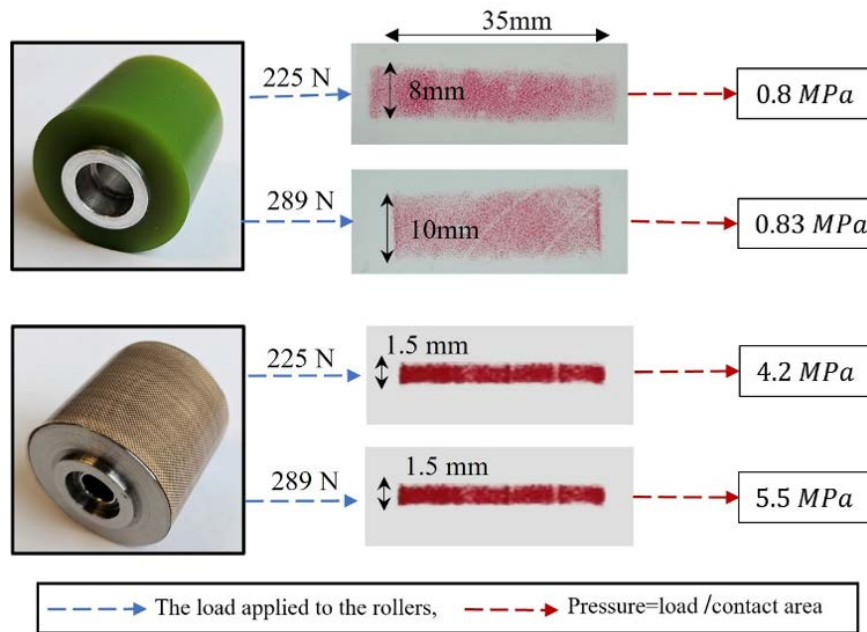


Figure 6.4: Two different compaction rollers and the values of four different levels of pressure were used in the preparation of SLJ samples.

shear strength of the single lap joint samples is examined.

#### 6.4.1 Pressure effect

The load-displacement curves for SLJ samples created under the four different levels of pressure are shown in Figure 6.5. The most significant observations from Figure 6.5 can be outlined as: The elastic regions which are identified as the sections of the load-displacement curve with the steepest slope at the initial stage, indicate similar characteristics in all samples. The viscoelastic behavior of the interfacial bonding in the bonded prepreg tapes and the occurrence of cracks in the bonded area due to tension leads to a gradual decline in the slope of the force-displacement curve over time until it reaches the failure point. Because of the pressure sensitivity inherent in uncured thermoset prepreg, it is observed that an increase in load from 225 N to 289 N leads to a 33% and 86% increase in the failure load or PUR and SSR, respectively. Notably, the results indicate that at the lower force (225 N), although the pressure applied by PUR is less than that of SSR, the larger contact area for PUR results in a higher dwell time. This extended dwell time contributes to

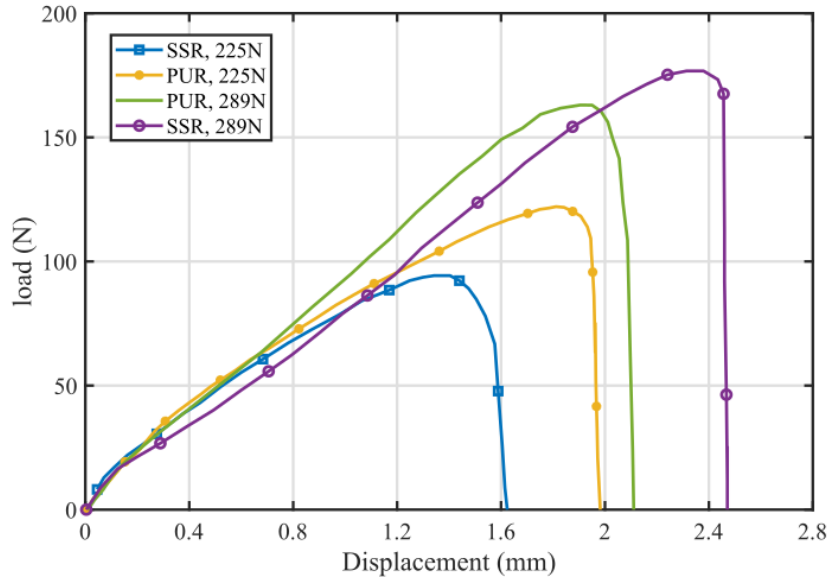


Figure 6.5: Comparison of load-displacement curves for uncured prepreg tapes bonded (SLJ) samples under different loads.

creating a stronger bond between the two prepreg tapes. However, at higher force (289 N), the greater pressure applied by SSR compensates for the difference in dwell time, leading to a significantly stronger bond between the two prepreg pieces.

#### 6.4.2 Feed rate and dwell time effects

As mentioned, SLJ samples were produced at different lay-up speeds of 15 mm/s, 35 mm/s, and 50 mm/s. The resulting force-displacement curves are shown in Figure 6.6, demonstrating that PUR samples exhibit higher failure loads and strains to failure compared to SSR. For SSR, among the lay-up speeds of 15 mm/s, 35 mm/s, 50 mm/s, and 80 mm/s, the minimum failure load corresponds to the 80 mm/s speed. This is likely due to the high speed preventing the bonding from forming effectively. However, between 15 mm/s, 35 mm/s, and 50 mm/s, the minimum failure load occurs at 15 mm/s. This can be attributed to the reduced feed rate potentially leading to uneven fiber distribution or alignment, along with an increase in width and a decrease in thickness as the resin is pushed towards the sides. The influence of feed rate is more significant in SSR samples than in PUR ones. Increasing the feed rate from 15 mm/s to 35 mm/s and 50 mm/s in SSR leads to a 13%

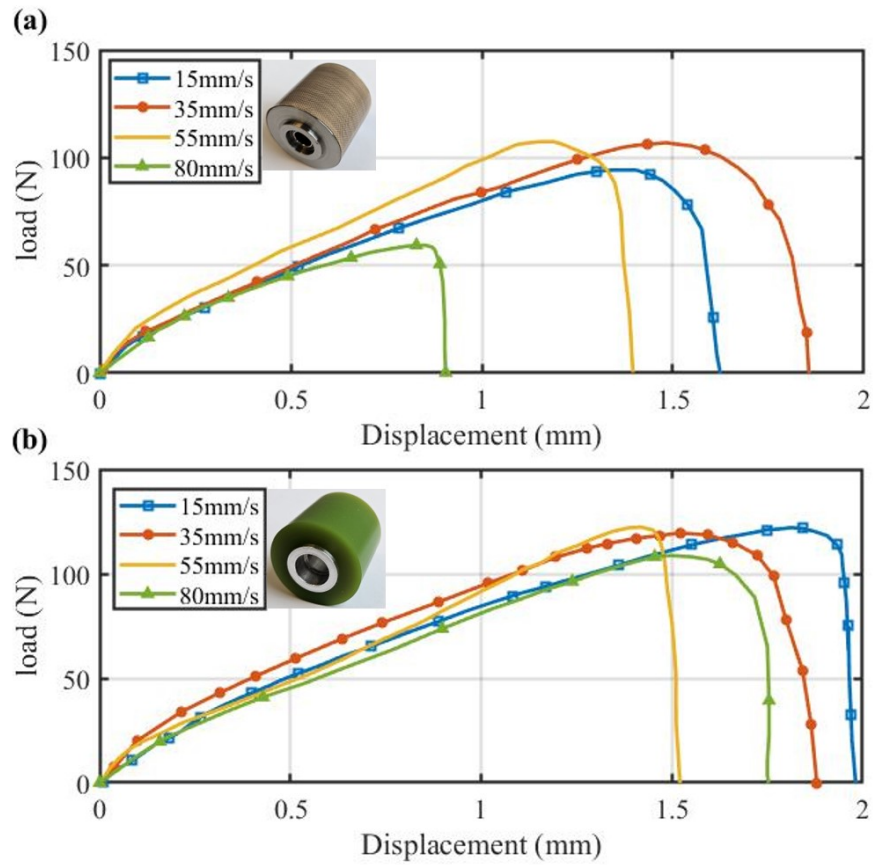


Figure 6.6: Comparison of load-displacement curves for SLJ specimens fabricated at 25°C and 225N under three different feed rates and compacted by: (a) SSR and (b) PUR.

and 13.5% increase in failure load, respectively. However, similar speed increments in PUR samples result in nearly identical failure loads. This can be explained by the difference in dwell time, where PUR benefits from a longer dwell time compared to SSR, allowing the tape sufficient time to bond effectively.

The longer dwell time for PUR is directly related to its larger contact length. As shown in Figure 3, the contact length for SSR is only 1.5 mm, while the contact length for PUR is about 8 mm. This extended contact length in PUR provides better dwell time, even at higher speeds, which results in improved bonding. As a result, changes in bonding strength with varying speeds are less pronounced for PUR than for SSR.

### 6.4.3 Temperature effect

The SLJ specimens were fabricated at two different temperature levels: (i) at room temperature, approximately 25 degrees Celsius, and (ii) at an elevated temperature of around 45 degrees Celsius. It is noteworthy that in the process of creating these single lap joint samples, the prepreg pieces underwent initial heating. Subsequently, the compaction roller was applied at various feed rates to ensure the bonding of all samples at the elevated temperature of 45 degrees Celsius. Figure 6.7 shows the load-displacement curves of SLJ samples at different temperature levels. These results illustrate that an increase in temperature from 25 to 45 degrees Celsius leads to a rise in shear strength in the bonded prepreg samples. This enhancement is ascribed to increasing resin diffusion at the bonded region. Indeed, the increased temperature reduces the resin viscosity which results in a rise in resin diffusion at the interface, thereby leading to the increased shear strength observed in the SLJ samples. Certainly! It's essential to note that there's an optimal temperature level, for temperatures below this threshold lead to high viscosity, preventing diffusion of resin in the inter-laminar layer, while temperatures above it can cause excessive flow or even curing of the resin in the bonding area during the lay-up process (before autoclave process) that both scenarios can have a negative impact the part's quality. Besides, it can be observed that as the temperature increases, the failure load results for the two compaction rollers tend to become closer. Indeed, with the increasing temperature, the influence of pressure on modifying the failure load diminishes.

To gain a deeper insight into how pressure, temperature, and feed rate affect shear strength, we have represented the failure loads of SLJ samples shown in previous graphs as a bar chart in Figure 6.8. For ease of comparison, all failure loads have been normalized by dividing them by the maximum failure load, which corresponds to the sample created under the conditions of a temperature of 45 and a pressure of 289N by SSR. Generally, it can be concluded that elevating both pressure and temperature to 289 N and 45 °C, respectively, has a beneficial impact on enhancing inter-laminar strength, while simultaneously reducing the influence of dwell time on inter-laminar strength.

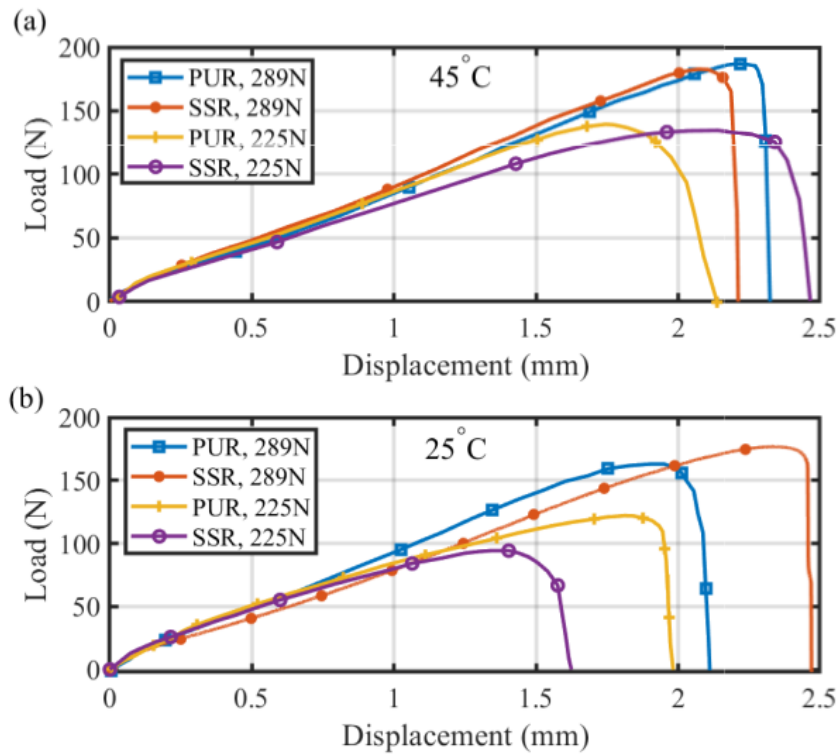


Figure 6.7: Comparison of load-displacement curves for SLJ specimens fabricated with the feed rate of 14 mm/s under different levels of pressures and temperatures: (a) 45 °C and (b) 25 °C.

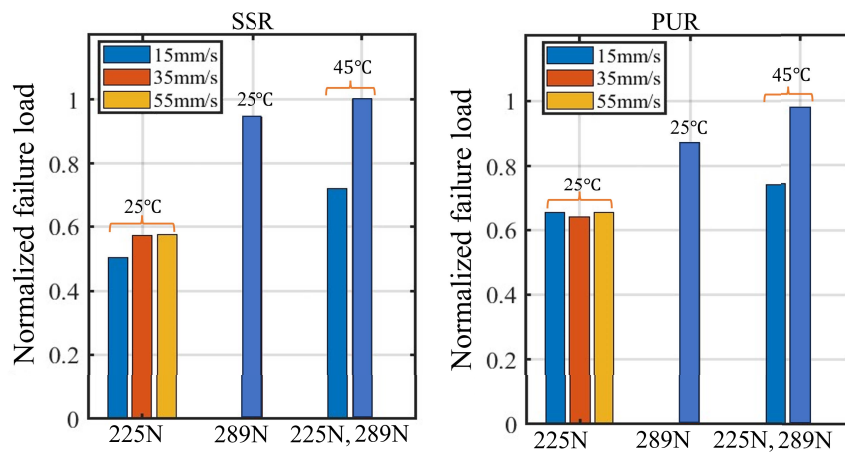


Figure 6.8: Comparison of experimentally obtained failure load of uncured prepreg SLJ samples created under different process conditions.

Table 6.2: Effect of process parameters on the geometry of the prepreg tape and SLJ overlap section.

Process conditions			Measurements						
Type of roller	Temperature and load	Feed-rate	Width (mm)	Standard deviation	Thickness (mm)	Standard deviation	Thickness of overlap (mm)	Standard deviation	
PUR	T=25C L=225N	15mm/s	6.64	0.023	0.166	0.0013	0.322	0.0012	
		35mm/s	6.55	0.023	0.167	0.0016	0.323	0.0013	
		55mm/s	6.48	0.024	0.170	0.0018	0.334	0.0016	
	T=25C L=289N	15mm/s	6.82	0.021	0.16	0.0012	0.321	0.0012	
		T=45C L=225N	15mm/s	6.78	0.02	0.162	0.001	0.322	0.001
			15mm/s	6.87	0.033	0.153	0.0012	0.304	0.0014
SSR	T=25C L=225N	35mm/s	6.85	0.04	0.153	0.0012	0.303	0.0012	
		55mm/s	6.81	0.052	0.156	0.0013	0.31	0.0011	
		T=25C L=289N	15mm/s	6.97	0.021	0.151	0.0012	0.30	0.0013
	T=45C L=225N	15mm/s	6.95	0.02	0.151	0.001	0.301	0.0012	

## 6.5 Geometric and microscopic analysis

The results are presented in Table. 6.2 provides a summary of the measurements conducted on the width and thickness of SLJ samples produced under various conditions. The measurements reveal that as the load and temperature rise, the width increases while the thickness decreases. Notably, this change is more significant for SSR than the PUR. Moreover, It's important to note that excessively increasing the width may result in defects like gaps and overlaps during the process.

The photomicrographs are captured from the samples after the test using optical microscopy to illustrate catastrophic failures and bonding areas in SLJ samples created under varying conditions. The pictures are taken from three different regions of each sample: 1) in an unbounded area, 2) with half the frame showing the bonding area and the other half depicting anon-bonding area, and 3) exclusively from the bonding region. Figure 6.9 shows the micrographs taken from SLJ samples fabricated by PUR under four different conditions: (i) Temperature of 25°C, speed of 35 mm/s, and pressure of 225 N, (ii) Temperature of 25°C, speed of 15 mm/s, and pressure of 225 N, (iii) Temperature of 45°C, speed of 15 mm/s, and pressure of 225 N, (iv) Temperature of 25°C, speed of 15 mm/s, and pressure of 289 N. The analysis of these micro-graphs reveals several significant findings: The visuals indicate a mixed failure mode, involving both [interfacial resin failure \(analogous to](#)

adhesive failure in systems with a distinct adhesive layer) and matrix separation (analogous to cohesive failure in such systems) in the SLJ samples. The areas corresponding to interfacial resin failure and matrix separation are indicated in Fig. 6.9 by yellow dashed lines and blue square-dotted lines, respectively. Notably, as the feed-rate decreases from 35 mm/s to 15 mm/s in samples produced with PUR, there is a noticeable enhancement in bonding. This is evidenced by a reduction in the [interfacial resin failure](#) region and a more pronounced occurrence of [matrix separation](#), indicating an improved bonding quality. To further investigate the bonding quality, photomicrographs of the cross-sections of the same samples presented in Figure 6.9 were captured before conducting the tensile tests. Figure 6.10 displays these images, providing a detailed view of the bonding interface between the two uncured prepreg tapes. As shown in Figure 6.10, samples produced under conditions (i) and (ii) exhibit significant resin-rich regions at the bonding area, suggesting weak bonding between the prepreg tapes. Conversely, in specimens (iii) and (iv), the increased pressure and temperature resulted in a reduction of resin-rich areas, indicating an improved bonding quality between the prepreg tapes.

## 6.6 Numerical simulation and results

### 6.6.1 Description of the FE model

The ABAQUS/Explicit software was considered for this research to model the mechanical behavior of the SLJ samples subjected to the quasi-static tensile loading. One of the common methodologies for simulating the interface layer is the cohesive zone model (CZM). This model is characterized based on a traction-separation law, which defines the correlation between the stress (traction) applied across the interface and the corresponding displacement [Campilho, Banea, Neto, and Da Silva \(2012\)](#); [B. Liu et al. \(2020\)](#). In this context, there is extensive literature on modeling the mode I and II fracture of composite laminates through different approaches of the cohesive zone model [Li, Thouless, Waas, Schroeder, and Zavattieri \(2005\)](#); [Machado, Fischlschweiger, and Major \(2015\)](#); [Rafiee and Sotoudeh \(2021\)](#); ?. The stickiness of uncured prepreg tapes to the substrate was modeled during the

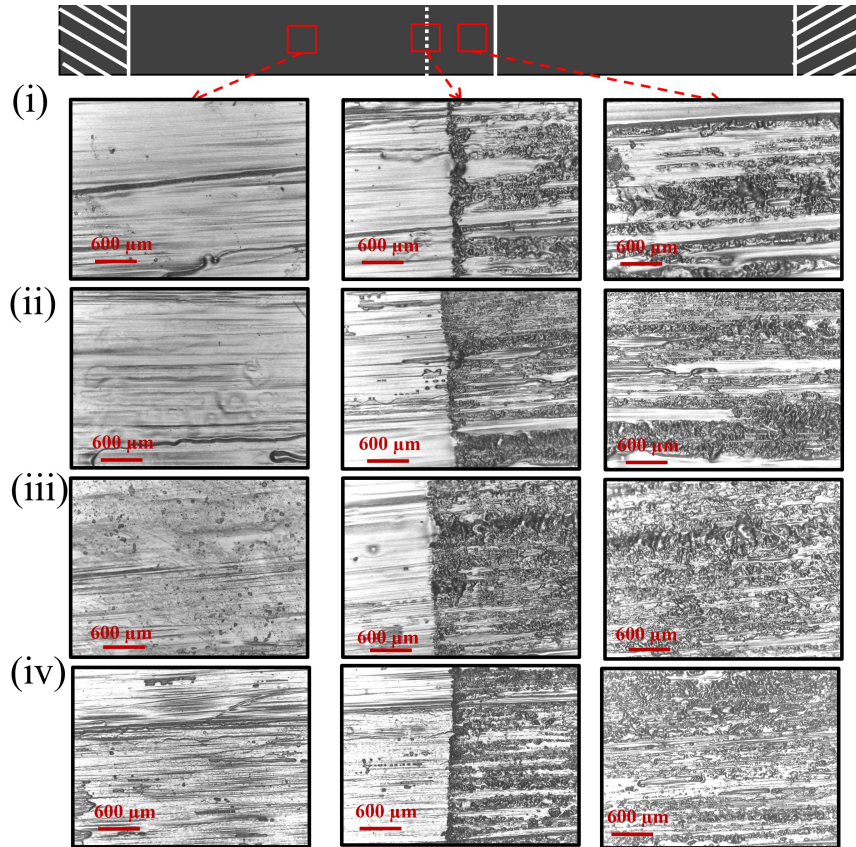


Figure 6.9: Captured Micrographs of SLJ Samples Created with PUR under Varied Conditions: (i) 35 mm/s Feed Rate and 25°C and 225 N, (ii) 15 mm/s Feed Rate and 25°C and 225 N, (iii) 15 mm/s Feed Rate and 45°C and 225 N, (iv) 15 mm/s Feed Rate and 25°C and 289 N.

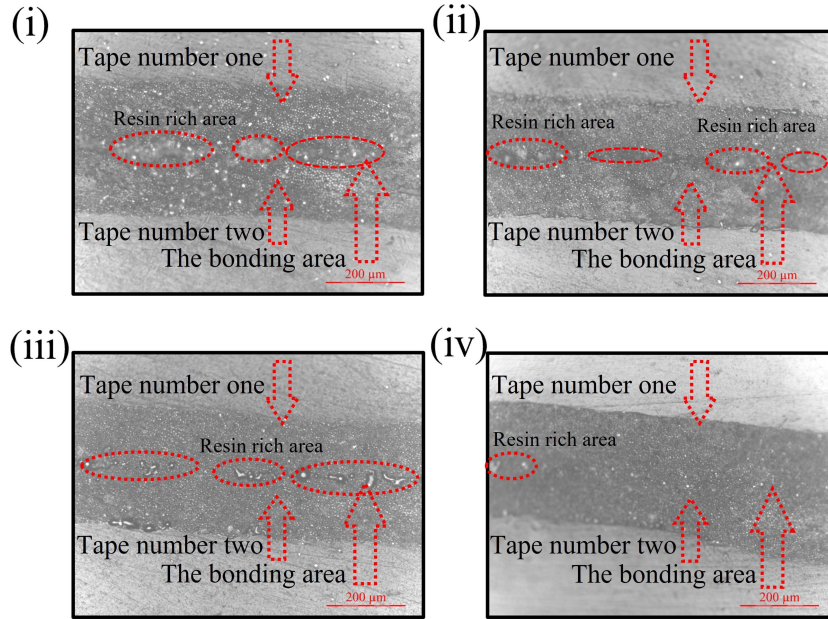


Figure 6.10: Captured Micrographs of the cross-section of SLJ specimens in the bonding area before the tensile test fabricated with PUR under Varied Conditions: (i) 35 mm/s Feed Rate and 25°C and 225 N, (ii) 15 mm/s Feed Rate and 25°C and 225 N, (iii) 15 mm/s Feed Rate and 45°C and 225 N, (iv) 15 mm/s Feed Rate and 25°C and 289 N.

steering process by employing the cohesive zone model in [Rajan et al. \(2020\)](#). Therefore, in this research, a cohesive zone model is developed for the simulation of the SLJ behavior of the prepreg tapes bonded.

In this approach, the force-displacement curves obtained from the SLJ tests are first used to generate the traction-separation (T-S) curves. These T-S curves are then utilized to define the properties of the cohesive element. According to the force-displacement curves shown in the experimental results section, it is evident that the T-S curves exhibit a non-linear softening part due to the damage propagation in the bonded interface. The relationship between traction and separation can be defined in the form of:

$$T_t = K_t \delta_t \quad (66)$$

where  $T_t$  and  $\delta_t$  represent the traction and relative displacement in the shear direction,

respectively.  $K_t$  is the stiffness parameter of the interface layer is expressed as:

$$K_t = \begin{cases} K_0 & \text{if } \delta \leq \delta_0 \\ K_0(1 - D_t) & \text{if } \delta_0 < \delta < \delta_f \\ 0 & \text{if } \delta \geq \delta_f \end{cases} \quad (67)$$

where  $\delta$ ,  $\delta_0$ , and  $\delta_f$  are the separation (displacement) in the shear direction, the amount of separation as far as the elastic region exists (before the softening region), and the separation corresponding to complete damage.  $K_0$  is the stiffness of the elastic region and the parameter  $D_t$  is a damage parameter, representing the ratio of the actual stress obtained from the test to the stress that would occur if there were no damage in the interface layer. This parameter can be determined using the following formula:

$$D_t = 1 - \frac{T_t}{K_0 \delta} \quad (68)$$

Based on Equation 68 and 67, when  $D_t = 0$  it indicates that no damage has occurred, and when  $D_t = 1$ , it denotes that failure has occurred. Therefore, to accurately define the cohesive element properties for the bonding between the prepreg tapes into the Abaqus software, two parameters are needed: elastic parameters and damage evolution parameters. Elastic parameters are derived from the linear elastic region of the traction-separation curve, while damage evolution parameters are extracted from the softening region of the T-S curve and input into Abaqus in the tabular form as a function of displacement (separation). In our simulation, prepreg tapes as adherents of the SLJ samples are modeled using the mechanical properties presented in Table 6.3 and they are meshed using solid elements, specifically the 8-node (C3D8R) elements. The interface layer at the bonding area is also meshed using an 8-node three-dimensional cohesive element (COH3D8). The shape and final meshed model of the SLJ sample are depicted in Figure 6.11.

Table 6.3: Mechanical properties of prepreg tape as an adherend for the SLJ simulation Belhaj and Hojjati (2018).

$E_1$ (GPa)	$E_2$ (MPa)	$E_3$ (MPa)	$G_{12}$ (MPa)	$\nu_{12}$
120	0.046	0.046	3.025	0.2

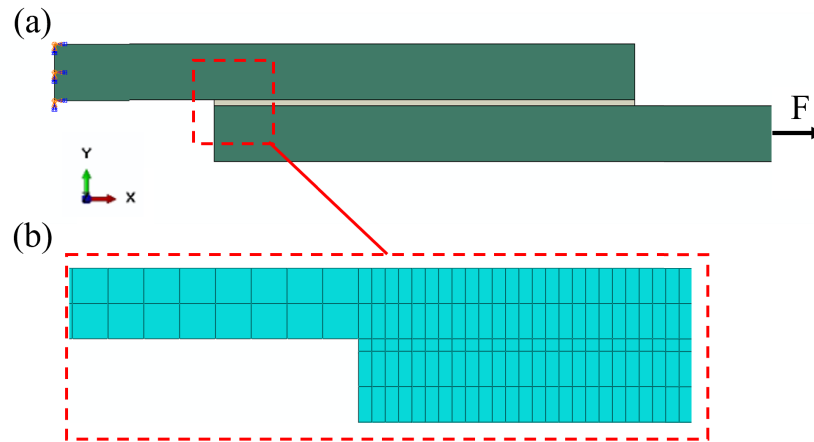


Figure 6.11: FE model of the single lap joint: (a) configuration, and boundary conditions, (b) mesh details.

### 6.6.2 Simulation results

To assess the simulation model developed in this study, the characteristics of the SLJ samples generated under specific process conditions were input into the Abaqus software. In order to verify the accuracy of the model, Figure 6.12a presents the force-displacement curves, both numerical and experimental, for three specific tests within the experimental set. Test A reveals results for a sample produced at 289N, 14mm/s, and 25°C using PUR. Test B displays results for a sample manufactured at 225N, 14mm/s, and 45°C using PUR. Lastly, Test C shows the results for a sample created at 225N, 14mm/s, and 25°C using SSR. The outcomes from the simulation reveal an excellent agreement between the model and experimental findings. One valuable factor in understanding inter-laminar shear behavior is the energy dissipated by damage. The FE simulation can capture this energy, as depicted in Figure 6.12b. Initially, when there is no damage in the specimen (elastic region), the energy dissipated by damage remains zero. As displacement increases the energy dissipated shows a gradual increase, and after surpassing the maximum force the damage energy dissipated in the specimen sharply rises. This increase shows damage propagation in the interface layer of SLJ samples.

Having validated the integrity of the developed model, the simulation can be employed in enhancing our comprehension of the shear behavior of SLJ samples. The shear stress

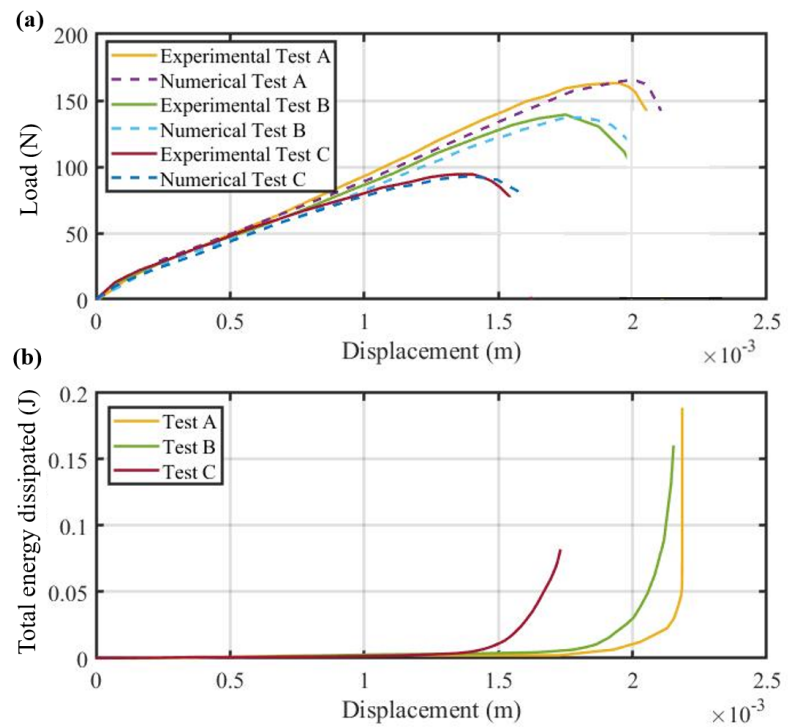


Figure 6.12: Verification and total energy dissipated by damage based on the FE model: (a) Comparison between the experimental and numerical load-displacement results. (b) Total energy dissipated by damage in each specimen.

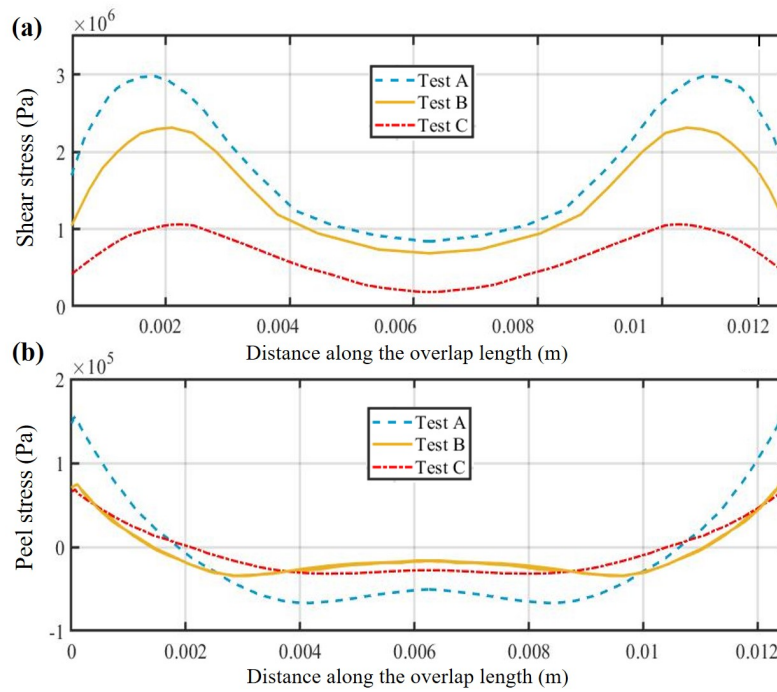


Figure 6.13: Adhesive shear and peel stress distribution for uncured prepreg SLJ samples: (a) Adhesive shear distribution, (b) Peel stress distribution at the overlap area.

distribution in the sample is shown in Figure 6.13, where it becomes evident that the highest shear stress values are concentrated at the regions near corners of the overlap, and by moving towards the center of the overlap, these stress values gradually decrease. Moreover, due to the load eccentricity in SLJ, there will be a bending moment and normal (peel) stress at the sample with the highest levels occurring at the corners (see Figure 6.13b). This indicates why the initiation of inter-laminar damage primarily originates from these corner areas.

In this context, Figure 6.14a shows the stress concentration in the corner of the prepreg SLJ samples prior to the onset of damage. Figure 6.14b shows the damage initiation in SLJ samples, where it is observed that cohesive elements near the corner have been eliminated due to exceeding their capacity, while cohesive elements near the center of the overlap continue to withstand the force applied to the SLJ sample.

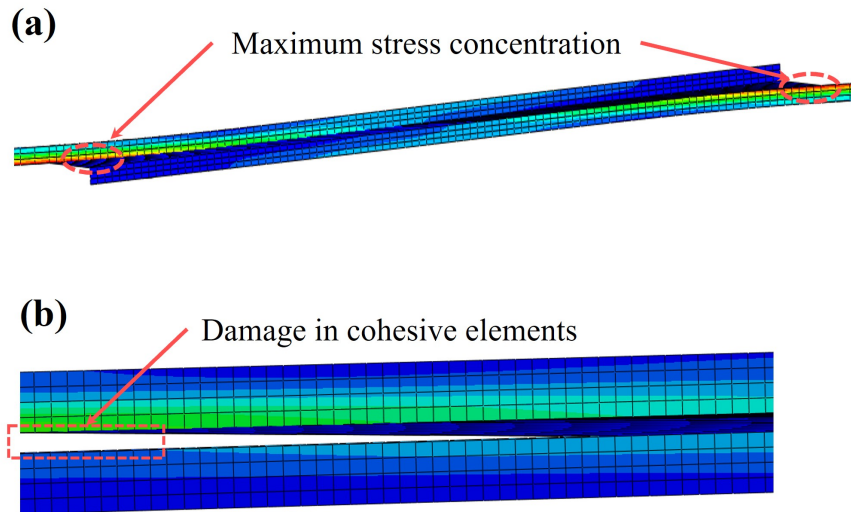


Figure 6.14: The results of the SLJ FE model: (a) Stress concentration in SLJ samples before failure, (b) Damage initiation in cohesive elements.

## 6.7 Conclusion

In this work, a comprehensive series of experimental and numerical investigations were conducted to deepen our understanding of the inter-laminar shear behavior of the uncured prepreg during the AFP process. To assess the shear response of the uncured prepreg, we utilize the single-lap bonded joint samples made of uncured prepreg tapes. These specimens were created, considering different levels of AFP process parameters including temperature, pressure, dwell time, and feed rate. This study, incorporating experimental and numerical approaches, pursues two main goals: predicting optimal parameters for automated fiber placement (AFP) to maximize inter-laminar shear strength during the AFP process and developing a shear strength model for uncured prepreg bonding to find the distribution of the stresses in the interfacial bonding along the overlap length.

The most important findings by analyzing the experimental data are summarized as:

- Generally, increasing the temperature from 25 °C to 45 °C and raising the load applied

on the rollers from 225 to 289 leads to an improvement in inter-laminar shear strength by enhancing the bond between the two prepreg tapes within the overlap range. In this context, increasing the load has a more pronounced impact on enhancing the shear strength of samples produced using SSR compared to PUR. Meanwhile, elevating the temperature exerts a more significant influence on improving the shear strength of samples fabricated by PUR.

- A significant observation derived from the shear strength results of samples produced by two rollers under a lower load of 225 N is that, despite the SSR applying greater pressure to the samples compared to the PUR, the shear strength of samples created by the PUR surpasses that of the SSR. This is attributed to the extended dwell time or compaction period of the PUR. However, upon increasing the load on the rollers to 289, the pressure applied by the SSR significantly exceeds that of the PUR (See Figure 6.4). This heightened pressure diminishes the impact of the compaction period, resulting in well-formed bonding in the samples produced by the SSR, even with a shorter compaction period.
- While there are overall conclusions regarding the effect of parameters on shear strength, the experiment results imply that the prediction of the shear strength of SLJ samples is not exclusively reliant on individual parameters. Rather, it is connected to the combination of various process parameters. Indeed, it is not straightforward to determine that changes in each parameter lead to specific outcomes. Instead, it is urgent to consider all parameters together for deriving meaningful conclusions regarding the shear strength of the samples.

Furthermore, micrograph images of the PUR indicate a mixed failure mode in SLJ samples produced from prepreg tapes. In addition, it was observed that in the process of creating SLJ samples with the PUR, improving bonding quality is achieved by reducing the feed rate and increasing the temperature and pressure from 25 °C to 45 °C and from 225 N to 289 N, respectively. Remarkably, the temperature and pressure increase has a more pronounced effect on bonding quality compared to the feed rate, likely because higher

temperatures reduce the viscosity of the resin, leading to a more extensive resin diffusion at the bonded area. Finally, a FEM model was developed which is demonstrating excellent agreement with experimental findings. Consequently, the FEM model proved valuable for assessing the complex stress distribution within the adhesive layer and adherents under various Automated Fiber Placement (AFP) process conditions. Additionally, it provided insights into the damage behavior occurring in the interface layer of bonded prepreg tapes.

## Chapter 7

# A Novel Compaction Roller with Variable Pressure Distribution and Contact Time for Automated Fiber Placement: Experimental and Numerical Analysis

This work has been accepted in:

Kheradpisheh, Meisam, and Mehdi Hojjati. "A Novel Compaction Roller with Variable Pressure Distribution and Contact Time for Automated Fiber Placement: Experimental and Numerical Analysis." *Composites Part A: Applied Science and Manufacturing* (Published).

## 7.1 Abstract

Automated fiber placement (AFP) technology has gained significant traction due to its adaptability in processing large composite parts with complex geometry. However, a key challenge remains in reducing defects during the layup process to enhance the quality of AFP-manufactured components. This study aims to reduce defect formation in the AFP by introducing a new approach that involves altering the pressure distribution and contact length exerted by the compaction roller during the AFP process. To demonstrate the effectiveness of this approach, the research focuses on out-of-plane defects, commonly known as wrinkle and tape folding deformations, which occur during fiber steering. To address this issue, a new designed compaction roller has been designed and manufactured to provide variable pressure distributions and contact length based on the geometry of the part, unlike traditional rollers. This new roller features a concave shape that adjusts pressure application and contact duration along its length, applying higher pressure for extended periods at the towpreg edges. Finite element (FE) analysis was employed to simulate the roller deformation and pressure distribution, helping to determine the dimensions, particularly the concave radius. A three-part PLA mold was manufactured using the dimensions obtained from the simulations, and polyurethane rollers were produced through casting into the molds. AFP trials were conducted to compare the performance of the new roller against standard compaction rollers. The results demonstrated a 24 percent reduction in wrinkle length with the new roller, highlighting its effectiveness in improving the AFP process.

## 7.2 Introduction

The increasing adoption of carbon fiber composite materials in aerospace and automotive industries has driven the demand for advanced automated manufacturing techniques. Recently, automated fiber placement (AFP) has made remarkable progress in manufacturing complex, large-scale composite structures with rapid material deposition, reduced waste, and improved reliability, making it superior to traditional manufacturing methods [Fereidouni and Hoa \(2024\)](#); [X. Wang et al. \(2024\)](#); [Zacherl, Fontes, and Shadmehri \(2024\)](#).

In the AFP process, a composite laminate is manufactured by additively laying up uncured prepreg tape next to and on top of each other. The AFP technology uses a robotic head to precisely place the uncured prepreg materials onto the substrate [H. Ma, Bandaru, and Weaver \(2024\)](#); [R. Wehbe, Tatting, et al. \(2020\)](#). This robotic head is equipped with a compaction roller and a heating source, which applies pressure and heat to adhere the prepreg tapes onto the substrate as shown in [Fig.7.1](#).

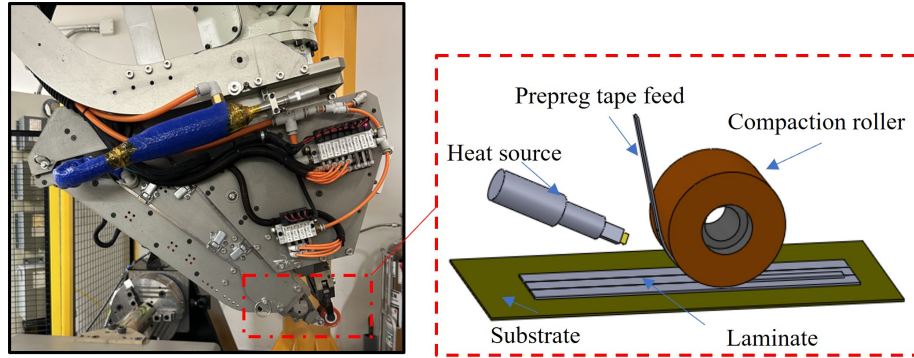


Figure 7.1: AFP head and a schematic diagram detailing the components of the AFP head.

Although AFP technology offers significant advantages, it still faces challenges due to various defects that occur during the lay-up process. These defects can reduce the structural performance of parts produced by AFP [Böckl, Wedel, Misik, and Drechsler \(2023\)](#); [Dirk et al. \(2012\)](#); [Oromiehie et al. \(2019\)](#). For instance, the work presented in [Croft et al. \(2011\)](#) showed that defects in the manufactured laminate using AFP have an impact on ultimate strength up to 13%. In the work [Zenker, Bruckner, and Drechsler \(2019\)](#) is also demonstrated that the common AFP defects can reduce the compressive strength of the final parts to 12%. Therefore, reducing or eliminating the defects has become a key focus for both researchers and industry professionals, as they aim to improve the reliability and performance of composite structures produced using AFP.

One of the most critical defects that occur during AFP is out-of-plane deformations, commonly referred to as wrinkle defects [Rajan et al. \(2019\)](#). These wrinkles occur when the fiber tape is laid on curved paths. [Bakhshi and Hojjati \(2018\)](#). As the tape follows a curved trajectory, the mismatch between the inner and outer edges of the tape creates an in-plane

load along the path direction, leading to buckling or wrinkling. This defect is particularly problematic because it persists even after the part undergoes autoclave processing, affecting the final part's quality. Given the inevitability of steering in manufacturing large-part structures, considerable literature has emerged focusing on the experimental and analytical investigation of defects at the steering process. Rajan et al. [Rajan et al. \(2019\)](#) conducted a comprehensive experimental study focusing on how defects form when the prepreg tape is placed along a curving path, a process known as the steering process. Their findings revealed that decreasing the curvature of the path leads to an increase in the number of wrinkles, attributed to the rising in-plane load within the prepreg tape. The work in [Bakhshi and Hojjati \(2018\)](#) presented an extensive series of AFP experiments to investigate the defect formation in the steering process. They carried out trial and error experiments to find suitable process parameters to reduce defects during the AFP manufacturing process. The authors of [Fischer et al. \(2015\)](#) conducted experimental investigations on structures with complex geometry in the AFP process, and proposed a path placement method to enhance the mechanical properties of steered tapes during manufacturing.

In order to gain a deeper understanding of the defect formation in the steering process, theoretical modeling has been pursued in conjunction with the experimental investigations. Beakou et al. [Beakou et al. \(2011\)](#) experimentally showed the formation of wrinkle defects in steered tape and presented an analytical buckling model for the prediction of these defects during the AFP process. In their buckling model, they considered the prepreg tape as a plate and the stickiness of the prepreg to the substrate was modeled as an elastic foundation using a series of normal springs. The work in [Matveev et al. \(2016\)](#) improved the analytical model for the wrinkle defect formation at a steered prepreg tape. They mathematically predicted a critical radius for the steering process, where no defects form in the tape when the radius is greater than this critical value. Furthermore, their study emphasized the significant role of tackiness between the prepreg and substrate, modeled as an elastic foundation, on defect formation. Moreover, the effect of shear parameters on wrinkle formation was presented by [Belhaj and Hojjati \(2018\)](#). They included shear parameters to the analytical model for the wrinkle formation to improve the prediction of

defect occurrence. Additionally, the effect of shear was considered in a FE model presented by [Rajan et al. \(2020\)](#), where they employed a cohesive zone model capable of accounting for both normal and shear parameters to describe the behavior of the prepreg's tackiness to the substrate during wrinkle formation. Given that the tackiness of the prepreg tape to the substrate exhibits viscoelastic properties, the influence of viscoelasticity parameters on defect formation was further explored in [Bakhshi and Hojjati \(2019\)](#); [Kheradpisheh and Hojjati \(2023\)](#). By replacing the elastic foundation model with a viscoelastic one, these studies considered the time-dependent behavior of wrinkle defects.

The analytical and experimental studies have shown that the stickiness of the prepreg tape to the substrate, known as prepreg tack, has a significant effect on the occurrence of defects during the AFP process. Prepreg tack is influenced by various process parameters, including pressure, temperature, feed rate, and contact time, as well as environmental conditions such as aging and humidity. Therefore, understanding the relationship between prepreg tack and these factors is essential for improving the AFP process and decreasing defects [Belhaj et al. \(2021\)](#); [Budelmann et al. \(2019, 2020\)](#); [Wohl et al. \(2017\)](#). The authors of [Heller et al. \(2018\)](#) showed that material aging worsened steering behavior in the AFP process. Their results showed that aging caused a decline in steering performance, leading to defects like fiber waviness and buckling. The work in [Belhaj et al. \(2021\)](#) studied the effects of AFP process parameters on the prepreg tack using a peel-off test. They measured the adhesion between the prepreg and substrate under the different values of AFP process parameters. Budelman et al. [Budelmann et al. \(2019, 2021\)](#) utilized a rheometer to evaluate the stickiness of the prepreg in the normal direction through a probe tack test. Their experimental results demonstrated how prepreg tack varies with changes in pressure and temperature. To measure prepreg tack under conditions more representative of the AFP process, the works in [R. Crossley et al. \(2012\)](#); [R. J. Crossley et al. \(2013\)](#) developed an innovative peel test apparatus to measure the prepreg tack in the normal direction (90 degrees). This setup simulated the AFP process, allowing for the recording of peel resistance and the analysis of how pressure and feed rate affect the peel resistance of prepreg tape. The authors of [Venkatesan et al. \(2023\)](#) investigated the impact of process parameters on the

shear and thermal properties of carbon fiber-reinforced thermoplastic (CFRTP) composites fabricated using AFP. They improved these parameters to enhance interlaminar shear strength. The tackiness of the prepreg to various substrate materials under different process parameters was investigated in [Endruweit et al. \(2018\)](#). Regarding the impact of pressure on prepreg tack especially in thermoset prepreg tapes, some studies have focused on pressure distribution and compaction roller during the AFP process. The works in [Etchegaray Bello et al. \(2022\)](#); [Vogl et al. \(2024\)](#) studied the impact of compaction and curing states on the mechanical properties and void content of AFP-manufactured laminates through various mechanical tests and micro CT analysis. The authors of [Bakhshi and Hojjati \(2020\)](#) analyzed the pressure distribution of compaction rollers with different stiffness properties. This study indicated that rollers with higher stiffness produce laminates of higher quality. The work in [Lu et al. \(2023\)](#) developed and verified a FE model to analyze the compaction pressure applied by rollers in Automated Dry Fibre Placement, investigating how roller material, tool curvature, and substrate thickness affect pressure distribution and prepreg tack. The authors in [He et al. \(2022\)](#) modeled and experimentally validated how segmented compaction rollers affect pressure distribution in AFP on the complex surface. They investigated how these rollers enhance pressure uniformity and prepreg tack, leading to improving the quality of the manufactured parts. The work in [Ammar and Shirinzadeh \(2021\)](#) studied the role of different compaction rollers on the quality of laminates manufactured on a flat substrate using an image processing method for evaluation of the defects. Their results revealed that parts produced with a steel roller exhibited higher quality compared to those made with polyurethane and perforated rollers. However, it is important to note that while rollers with higher stiffness perform well in flat lay-ups, they are not suitable for complex geometries. Their lack of flexibility prevents them from adequately covering all surfaces.

Based on the literature review, a strong bond between the prepreg tape and substrate is paramount in reducing the defect. While previous studies have investigated various factors influencing this bond, to the authors' knowledge, no study has previously focused on altering the pressure distribution and contact length beneath the compaction roller to improve this bonding based on the geometry of the part being manufactured. The

aim of this paper is to introduce a novel design that fills this gap by adjusting pressure distribution and contact length to improve prepreg tack and diminishing defects. To achieve this goal, we first identify the root causes of defects in steered prepreg tape. Based on these reasons, we developed a novel compaction roller design. We then employed a finite element analysis to simulate the new compaction roller in order to improve its design according to an iterative approach. Based on the data from the FE simulations, the new compaction roller is subsequently produced using a casting method. Finally, we conduct AFP experimental trials to demonstrate the effectiveness of the new roller in reducing defects.

### 7.3 Out-of-plane defects in AFP process

To develop effective solutions for industrial problems, a thorough understanding of the problem is crucial. This requires careful systematic experimentation and observation to gather comprehensive data. Therefore, a series of experiments have been performed using an AFP machine which its specifications are provided in detail in the section of the experimental verification in this work (Section 7.5.2). According to the experiment observations, when a prepreg tape is laid along a curved path, it experiences both compression and tension forces across its width due to the mismatch length. The compressive load at the inner edge of a steered tape leads to wrinkle formation (out-of-plane buckling at the inner edge), and the tensile load at the outer edge results in tape-folding defects (out-of-plane buckling at the outer edge). Fig. 7.2 shows a schematic of the steered prepreg tape, the load distribution caused by the length mismatch, and the resulting defect formations.

As observed in Fig. 7.2, weak bonding between the prepreg tape and the substrate increases the occurrence of out-of-plane defects at the inner and outer edges of the tape due to the compressive and tensile load. However, this question may be raised that according to the published articles, the probability of occurrence of tape-folding is lower than wrinkle formation, and we commonly observe the wrinkle formation at the steered tape. This is probably one of the reasons for the lack of dedicated studies on tape-folding. In this study, we mention this point, why as much as increasing adhesion on the inner edge is important to

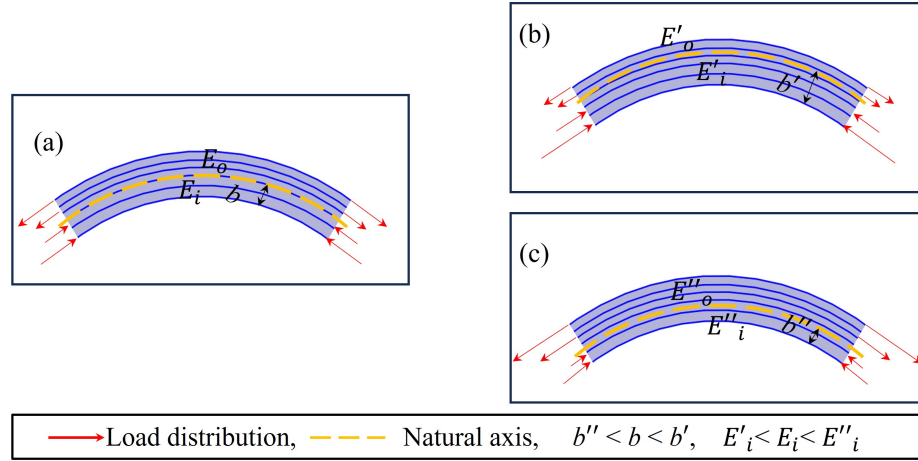


Figure 7.2: The effect of natural axis position on load distribution.  $E_i$  represent the stiffness for the area between the natural axis and inner edge (a) a steered tape under the linearly distributed load (b) a steered tape with some defects at the inner edge (c) a steered tape without any defects at the inner edge.

prevent wrinkles, it is also important on the outer edge. Indeed, we indicate that reducing the wrinkle defects at the inner edge can lead to increasing the occurrence of tape-folding, emphasizing the need for enhancing adhesion at the outer edge as well. Since the process of steering the tape is similar to the bending in mechanical concepts, the load applied to the steered tape can be assumed to be a linearly distributed load (see Fig. 7.2a). Therefore, the magnitude of the load distribution on the inner and outer edges is related to the position of the neutral axis. To show how reducing the wrinkles leads to the occurrence of tape-folding, we consider the neutral axis of the tape is located at a distance of  $b$  from the inner edge as shown in Fig 7.2a. and consider a stiffness value of  $E_i$  in length direction for the area between the inner edge and the neutral axis and a stiffness value of  $E_o$  in the length direction for the area between the neutral axis and the outer edge. Now, suppose some defects occur along the inner edge. In this case, the value of  $E_i$  decreases to  $E'_i$  due to the defect formation, causing the neutral axis to shift toward the outer edge. This shift affects the load distribution and reduces the maximum tensile load at the outer edge, as illustrated in Fig. 7.2b. In contrast, if we remove and reduce the wrinkle defects at the inner edge, in this case, the value of  $E_i$  reaches the maximum value ( $E''_i$ ), bringing the neutral axis closer to the inner edge. In this scenario, the tensile load at the outer edge increases, as shown in

Fig. 7.2c, and this rise can result in the tape-folding defect at the outer edge. As a result, if we aim to remove and reduce defects in a steered tape, it is essential to ensure proper prepreg tack at both the inner and outer edges.

## 7.4 Design and manufacturing procedure of new roller

In the previous sections, we demonstrated that to reduce the deformation of defects in the AFP process, particularly during the steering process, it is essential to enhance the tackiness of the prepreg. The effectiveness of increasing prepreg tape adhesion during the AFP process depends on parameters like temperature, pressure, and contact time. Based on the literature, the temperature corresponding to the maximum prepreg tack can be identified using a probe tack test. For instance, the study by Budelmann et al. [Budelmann et al. \(2019\)](#) revealed that a temperature range between 40°C and 45°C provides high tack in epoxy resin-impregnated prepreg. Therefore, by adjusting the AFP's temperature settings to ensure the prepreg tape reaches this desired temperature range during the lay-up, the temperature requirement can be achieved during the manufacturing process.

As a result, to achieve the highest adhesion between the prepreg and substrate, the pressure and contact time parameters must also be improved. The contact time is determined by the width of the contact area under the roller divided by the layup speed. This relationship means that contact time is also tied to pressure, as changes in pressure will affect the width of the contact area. Based on published works [Belhaj et al. \(2021\)](#); [Budelmann et al. \(2021\)](#), we know that increasing the parameters of pressure and contact time under the roller leads to an increase in adhesion between the prepreg and substrate. In this context, there are two common types of compaction rollers in AFP process: polyurethane rollers and stainless-steel rollers. The stainless-steel roller lacks flexibility, making it impossible to increase the contact time at a constant lay-up speed, as the contact time remains the same and a small value under any load. Moreover, solely increasing the pressure to maximize prepreg tack can cause other defects, such as resin being pushed to the sides of the tape and excessive widening of the tape, which leads to overlap and gap defects. Additionally,

due to its lack of flexibility, the flat stainless-steel roller cannot cover any curves or deformations in the mold, making it suitable only for straight lay-ups. On the other hand, the polyurethane roller also has some issues. If we use a polyurethane roller with low stiffness, increasing the load only increases the contact area, and the pressure under the roller does not change significantly due to its flexibility. Conversely, if we use a roller with high stiffness, we encounter the same problem as with the stainless-steel roller. Therefore, while it is well-established that increasing pressure and contact time can enhance prepreg tack, the limitations of current roller technology hinder our ability to enhance these parameters without causing other defects in the lay-up process. To address these problems, we have proposed a new idea: altering the pressure distribution under the roller to improve prepreg tack based on the specific geometry involved. This means designing a compaction roller to apply more pressure and contact time in areas where defects are likely to occur, ensuring better adhesion in those critical regions. To show the effectiveness of this idea, our case study in this research is diminishing the wrinkle formation at steered tapes. As discussed earlier, enhancing adhesion between the prepreg and substrate near the inner and outer edges is crucial to reducing defects. To clarify, since the maximum in-plane loads are applied to the most inner and outer edges of a steered tape, these areas require the highest level of adhesion. Therefore, we come up with a new idea of creating a concave roller to change pressure distribution uniformly under the compaction roller and create a sufficient bonding all over the tape related to the geometry during the AFP lay-up. Fig. 7.3 shows the schematic of the proposed roller with known and unknown dimensions.

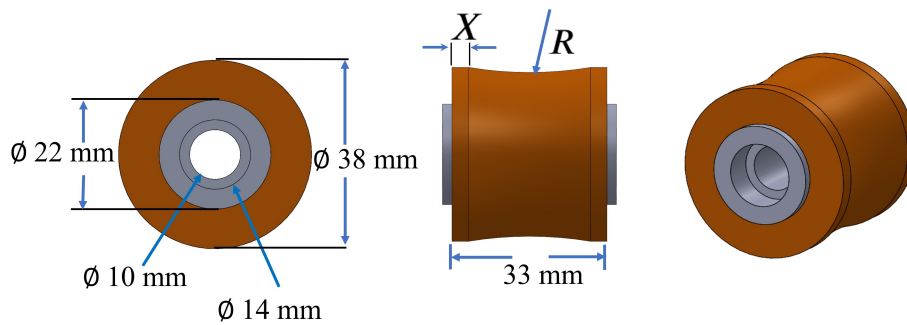


Figure 7.3: Schematic of the new concave compaction roller, illustrating the roller parameters:  $X$ , the horizontal distance from the roller's edge, and  $R$ , the concave radius.

As demonstrated in Fig. 7.3, the new compaction roller features a concave curve. This design applies higher pressure and contact time at the inner and outer edges, gradually decreasing these values uniformly towards the center of the roller. The next step is to determine the unknown parameters of this roller to ensure sufficient adhesion between the prepreg and the substrate in all regions of the steered tape. As can be seen from Fig. 7.3, there are two unknown dimensions: 1- the horizontal distance from the roller's edge ( $X$ ), 2- the radius of the concave section ( $R$ ). It is evident that these parameters play an important role in shaping the pressure distribution and contact length under the compaction roller. To improve adhesion, these parameters should be selected to produce a pressure distribution and contact length under the roller that increases adhesion near the edges (where maximum steering loads occur) while maintaining sufficient adhesion in the middle (where minimum steering loads are applied). The subsequent section provides detailed information on the design process and resulting pressure distribution and contact length under the concave roller.

#### 7.4.1 Finite element analysis for identifying unknown parameters

As previously mentioned, to reduce the defects in steered tape, the pressure distribution and contact length under the concave roller must be improved to create high adhesion at the edges of steered tape and relatively good adhesion in the middle. Based on AFP and tack experiments reported in the literature on the same material used in this study [Bakhshi and Hojjati \(2018\)](#); [Belhaj et al. \(2021\)](#), a high adhesion is achieved at a pressure of 1.2 MPa and a contact length of around 15 mm. Additionally, good adhesion is observed at a minimum pressure of 0.5 MPa with a contact length of 8 mm. Therefore, the  $X$  and  $R$  parameters must be chosen to ensure the pressure distribution and the contact length under the concave roller meet these conditions. This can be expressed mathematically as follows:

$$\begin{aligned}
 &\text{Find } X, R, \\
 &\text{such that } 0.5 \text{ MPa} \leq P_r(X, R) \leq 1.2 \text{ MPa}, \\
 &8 \text{ mm} \leq L_r(X, R) \leq 15 \text{ mm}.
 \end{aligned} \tag{69}$$

where  $P_r$  and  $L_r$  represent the pressure distribution and the contact length functions under the concave roller, respectively. It is evident that the minimum and maximum values in Equation 69 for the  $P_r$  and  $L_r$  are specific to the prepreg material used in this study, and these values may vary for different materials or under different conditions. To determine the values of  $X$  and  $R$  that satisfy the conditions in Equation 69, an FE model is developed. The pressure distribution and contact length under the roller are simulated in Abaqus software for various  $X$  and  $R$  values. Based on these results through iterative design, the values for  $X$  and  $R$  were selected to meet the requirements of Equation 69.

### **Description of 3D FE model**

A three-dimensional finite element model of the concave roller is created in Abaqus/Explicit. The roller's inner cylindrical shaft is modeled as a rigid body, and the substrate is simulated as an elastic material with properties akin to steel, while the compaction roller (typically composed of polyurethane or silicon) is simulated as a polyurethane with a stiffness of 2 MPa. This stiffness value is similar to the polyurethane material selected for the production of the new roller (section 7.4.2). To replicate the actual AFP process, a reference point is considered for the roller and tied to the inner surface of the roller for load application. In the simulation, a load of 220N is applied to this reference point. The roller and substrate components are meshed with 10-node quadratic tetrahedron (C3D10) elements. This element type was chosen because the low stiffness of the compaction roller caused significant deformations when using brick elements, such as the C3D8R. These deformations were severe enough to cause the model to fail, making the C3D10 elements a more suitable choice for maintaining model stability and accuracy. The assembly drawing and mesh detail are shown in Fig. 7.4.

### **Determination of $X$ and $R$ parameters based on simulation results**

As formulated in Equation 69, the objective of the concave roller design is to determine  $X$  and  $R$  parameters through an iterative process to achieve a desirable pressure distribution

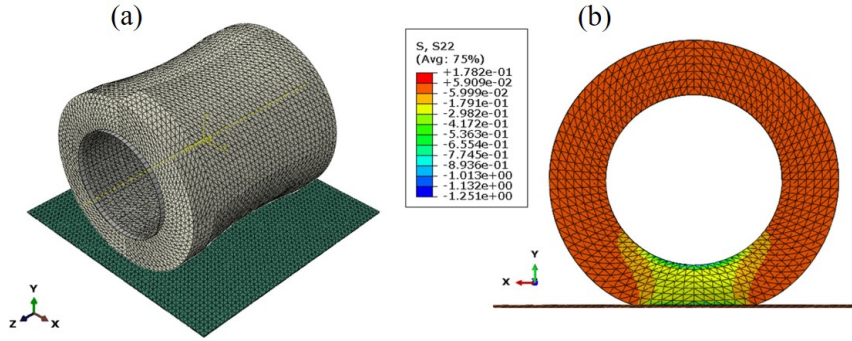


Figure 7.4: Finite element model of the concave roller (a) mesh details, (b) the simulation results.

and contact length. To achieve this goal, the pressure distribution and contact length of the concave roller on the substrate were obtained using the described Abaqus model for various values of these parameters. Fig. 7.5 illustrates some of these pressure distributions.

As shown in Fig. 7.5, for a fixed  $X$ , increasing  $R$  results in a decrease in the maximum pressure at the edges of the roller and an increase in the minimum pressure at the center of the roller. Additionally, for a fixed  $R$ , as  $X$  increases, the contact area near the edges increases, leading to a decrease in the maximum pressure and an increase in both the pressure and contact length at the center of the roller. To enhance understanding and facilitate comparison of the simulation results, the pressure values along the midline of each roller (along line AB in Fig. 7.5) and the contact length (along line CD in Fig. 7.5) from one end to the other end of the roller are presented in Fig. 7.6. Furthermore, this figure also includes the pressure and contact length data for the flat roller for better analysis. The most significant observation from Fig. 7.6(a-c) can be outlined as: for a constant  $X$ , the smallest value of  $R$  results in the highest pressure at the edges and the lowest pressure at the center. As the  $R$  value increases, the pressure difference between the edges and the middle of the concave roller decreases. For a fixed  $R$ , as the value of  $X$  decreases, the pressure increases, especially at the edges. This is attributed to the reduced contact area, which leads to higher pressure. Conversely, as  $X$  increases, the pressure distribution becomes more uniform for each radius. In Fig. 7.6(e-g), for a fixed  $R$ , increasing  $X$  decreases the contact length at the roller's ends while increasing it at the center. This causes the contact length ratio between

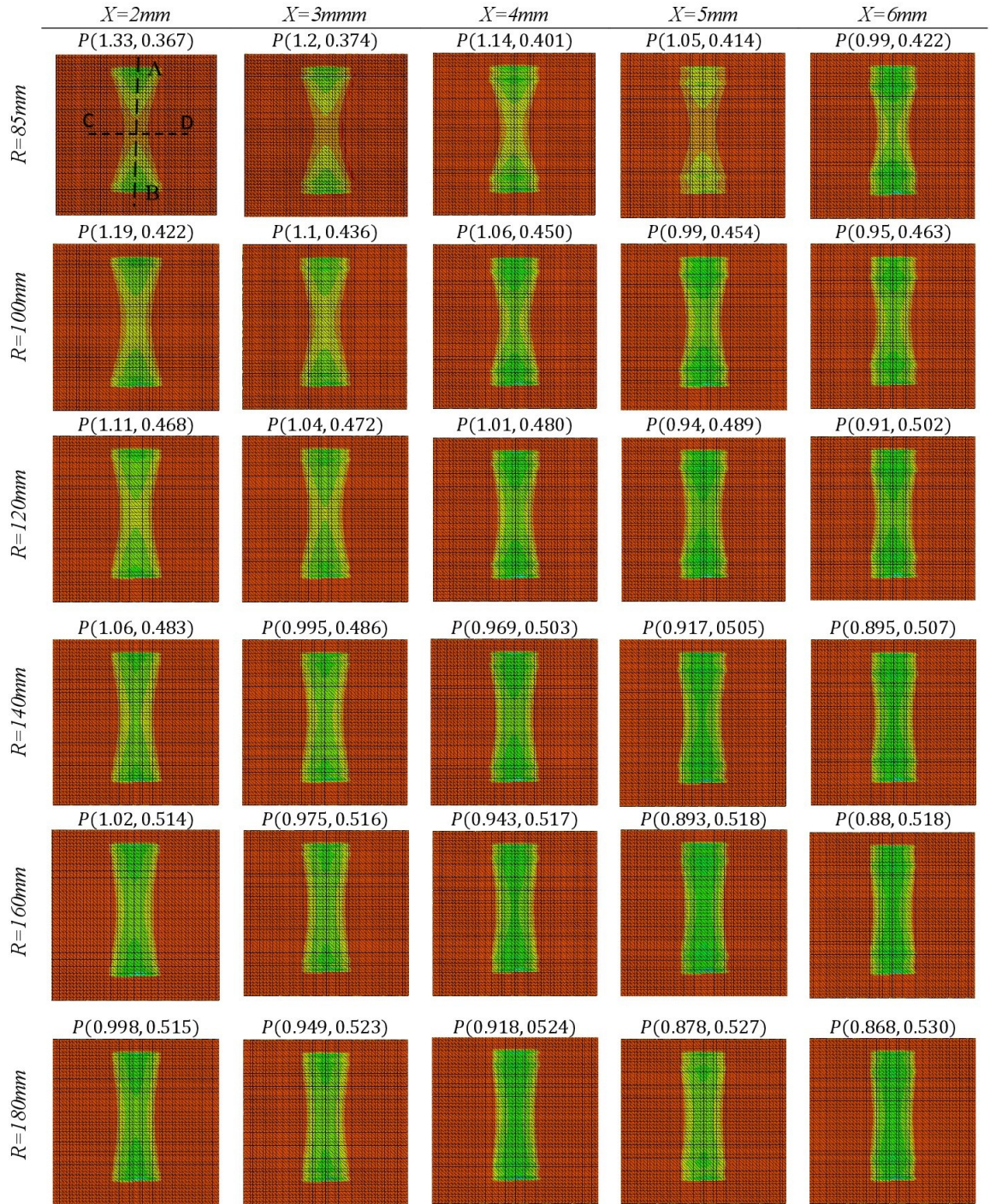


Figure 7.5: The simulation results for the concave roller with the different values of  $X$  and  $R$ ,  $P(\text{Max}, \text{Min})$  shows the maximum and minimum pressure for each roller in MPa.

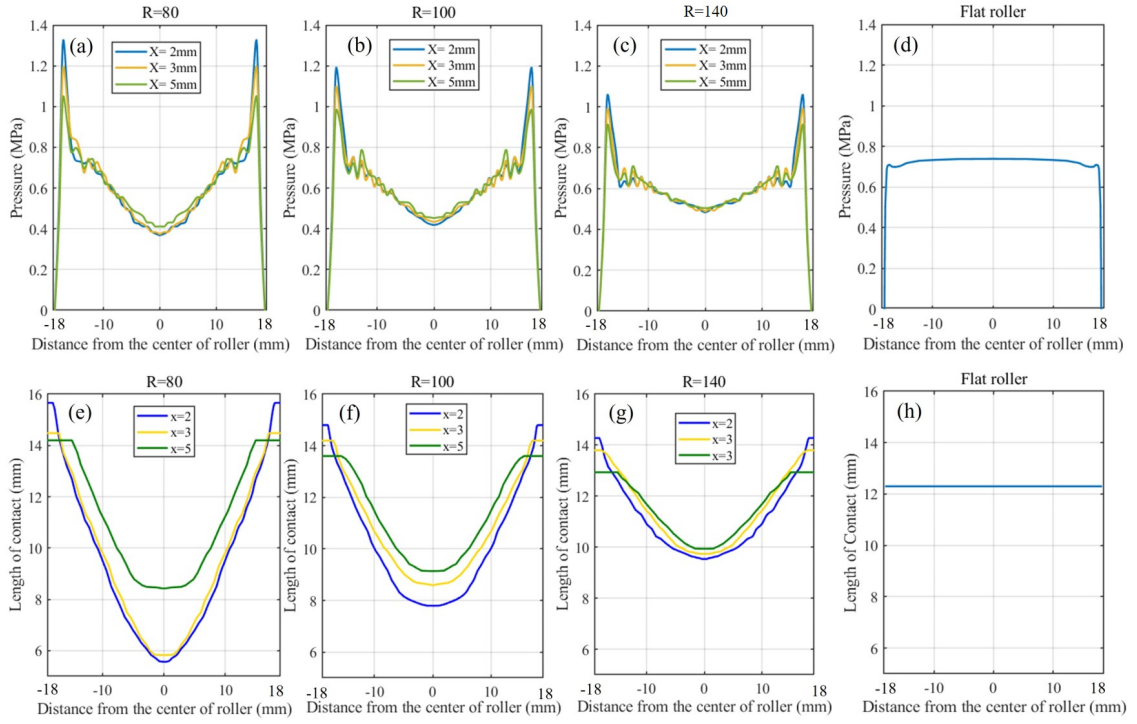


Figure 7.6: (a)-(c) Pressure distribution along the midline of the concave compaction rollers for various values of  $R$  and  $X$ . (d) Pressure distribution along the midline of the flat compaction roller. (e)-(g) Contact length spanning from one end of the concave roller to the other for various values of  $R$  and  $X$ . (h) Contact length spanning from one end to the other of the flat roller.

the ends and the center of the roller to approach one. Additionally, for a fixed  $X$ , increasing  $R$  results in a reduction of the contact length at the roller's ends, causing the contact length ratio between the corners and the center to approach one. However, in the case of (d) and (h), which represent the flat roller, the contact length and pressure are consistent along the roller.

Now, based on the simulation results, the  $X$  and  $R$  parameters should be selected to produce the desired pressure distribution and contact length defined in Equation 69. According to the FE data, the values that fulfill the requirements in Equation 69 are  $X = 3\text{mm}$ , and  $R = 100\text{mm}$ . It is apparent that the values are chosen based on the conditions outlined in Equation 69, which are specific to the material used in this study. These values may differ for other materials. The design process for the concave compaction roller is depicted in the framework shown in Fig. 7.7.

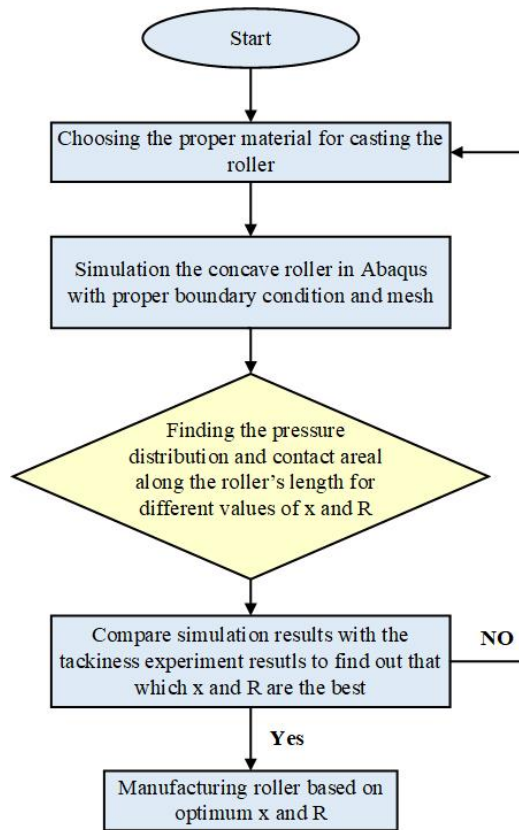


Figure 7.7: A flowchart illustrating the various stages in the design of the compaction roller.

Table 7.1: PLA filament properties and 3D printer setting parameters.

Polylactic acid (PLA) filament						
Diameter		Tolerance		Specific Gravity		
1.75 mm		+/- 0.03		1.24 g/cm <sup>3</sup>		
Printing setting						
Nozzel Temperature	Bed Temperature	Speed	Infill percentage	Infill patter	Resolution	
210 C	60 C	90 mm/s	80%	Lines	0.2 mm	

#### 7.4.2 Manufacturing of the new compaction roller

In this stage, a three-part mold is fabricated using a 3D printer with the material of polylactic acid (PLA) filament to be used for casting the new designed roller. The details of the PLA specifications and the 3D printer settings are illustrated in Table 7.1.

After 3D printing of the three-part mold with the dimensions derived from the FE simulations, A stainless steel tube, with an outer diameter of 22 mm, an inner diameter of 14 mm, and a length of 38 mm, is utilized as the inner shaft of the compaction roller.

Table 7.2: Freeman 2040 polyurethane elastomer physical properties.

mix ratio by weight	viscosity mixed (cps)	Gel time (minutes)	Demold time (hours)	Hardness (Shore A)	Specific Gravity (g/cc)
1:1	800	15	16	50	1.03

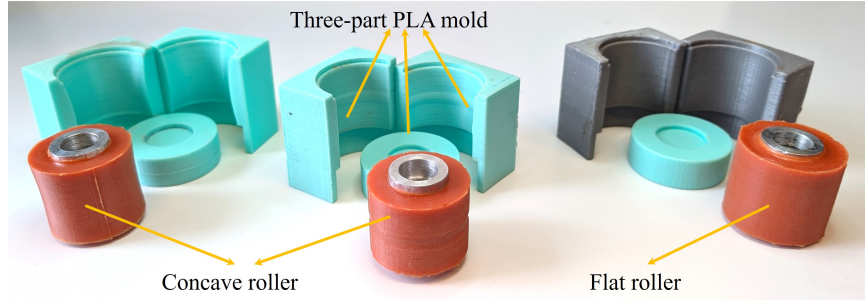


Figure 7.8: Details of three-part mold and new compaction roller.

Each side of the shaft has a 14 mm diameter hole drilled to a depth of 7.8 mm to house the bearings for mounting the rollers on the AFP head. The bottom plate of the mold has a circular recess to hold the inner shaft. Additionally, a polyurethane material known as Freeman 2040, provided by the Freeman Manufacturing & Supply Company, is used for casting in the mold. The specifications of the Freeman 2040 polyurethane elastomer material are displayed in Table 7.2. Finally, the three-part mold is assembled and clamped with four C-clamps, and the polyurethane elastomer is cast into the mold. The mold and the new compaction roller are illustrated in Fig. 7.8.

## 7.5 Results and discussion

### 7.5.1 Verification of the pressure distribution of the manufactured compaction rollers

In order to analyze the pressure distribution and contact area under the rollers, a two-layer ultralow pressure-sensitive film supplied by FUJIFILM Corporation is utilized. The pressure film typically consists of a base layer coated with the micro-encapsulated layer of color-forming materials (A-film), and another layer has a coating of color-developing material (C-film). The film is placed between the surfaces where pressure measurement is

needed. As the surfaces come into contact and apply pressure, the microcapsules in the film break and release the color-forming material which reacts with the color-developing material to produce the red color. The intensity of the red color shows the amount of pressure applied to that part of the film. The thickness of the layers is 0.2mm and the tests are performed at a temperature of around 20 °C.

To determine the pressure distribution of the rollers, the pressure films were placed on an aluminum substrate, and a load of 224 N was applied to the roller. The resulting color distribution on the pressure films was then obtained. Finally, an image segmentation technique was employed using MATLAB software to convert the pressure film images into ones that better illustrate the pressure distribution. Fig. 7.9 displays pressure film images, their corresponding processed images, and the FE simulation results, allowing for a side-by-side comparison.

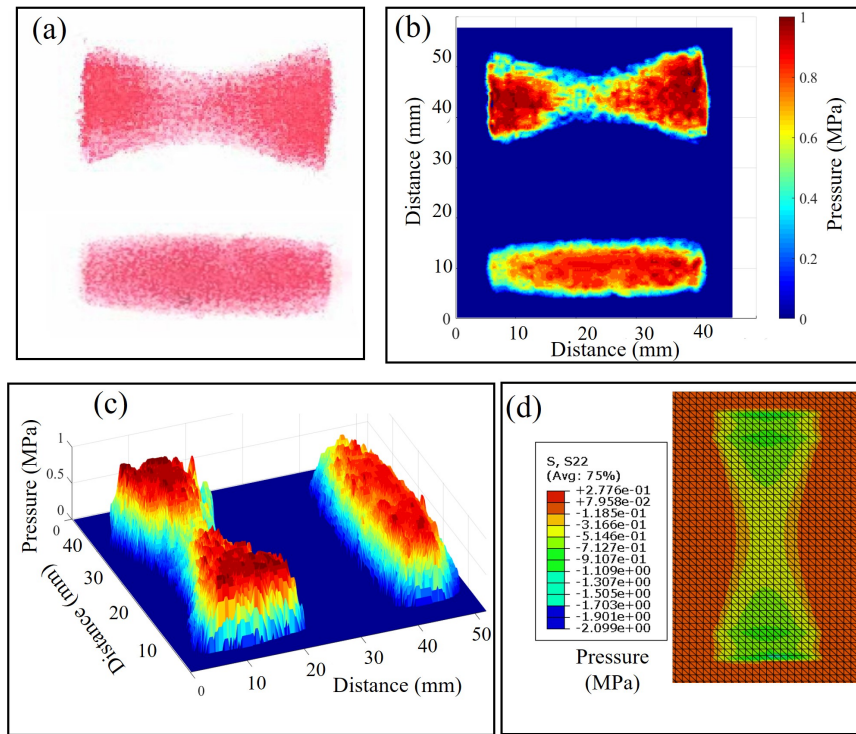


Figure 7.9: Comparison of pressure distribution results for concave and flat rollers: (a) Sensitive-pressure film measurements for both roller types, (b-c) Segmented processed images of the sensitive-pressure film data, (d) FE simulation of concave roller.

As observed from the images, the concave rollers have a different pressure distribution

compared to the flat compaction roller. The concave rollers exhibit higher contact pressure and contact length near the edges, with the pressure and contact length gradually decreasing towards the center of the roller. This observed pattern and the associated pressure values align closely with the finite element (FE) simulation results shown in Fig. 7.9d. The slight differences between the pressure values from the simulation and those measured by the pressure-sensitive film are likely due to the limitations of the film, which can only measure pressure within a certain range. Therefore, any pressures outside this range, whether higher or lower, may not be accurately recorded by the film.

### 7.5.2 AFP Experimental validation of new compaction roller Performance

A series of experiments have been performed using the AFP robot to assess the performance of the presented compaction roller. In this regard, a commercial thermoset AFP robot made by the Automated Dynamic Inc. machine was utilized to apply the prepreg tow onto the aluminum substrate. To provide heat during lay-up, a nitrogen hot gas torch is employed by the robot. Both standard flat and designed rollers are utilized to apply the necessary pressure throughout the lay-up process. Due to some limitations of the AFP robot used in this research, we were able to run the AFP by placing only one tape over the substrate in each experiment. Therefore, the new designed roller is considered to have a concave curve with a radius of 80 mm and a  $X$  equal to 14 mm and the length of the concave equal to 5.5 mm (see Fig. 7.3c) which is smaller than the width of the prepreg (6.35mm) to be able to apply a concentrated pressure to the area near the edges. The material used in the experiment is a 6.35 mm wide CYCOM 977-2 unidirectional carbon fiber thermoset prepreg tape supplied by Bombardier Inc., Canada, with a fiber content of 60% by volume and a thickness of 0.17 mm. To investigate the performance of the roller on out-of-buckling defects, several AFP trials were conducted to determine the suitable parameters for achieving accurate experimental observations of defects and to remove the occurrence of other undesirable defects during the lay-up process. These process parameters are illustrated in Table 7.3

To ensure the reproducibility and repeatability of the experimental results, the lay-up

Table 7.3: AFP process parameters utilized to assess the performance of the new roller during the steering process.

Compaction force	Nitrogen gas Temperature	Head cooling	Ambient Temperature	Flow rate of nitrogen	Feed rate	Radius of curvature
222.4 N (50 lb)	200 °C	20 °C	25 °C	75 (L/min)	76 (mm/s)	75, 90 and 100 cm

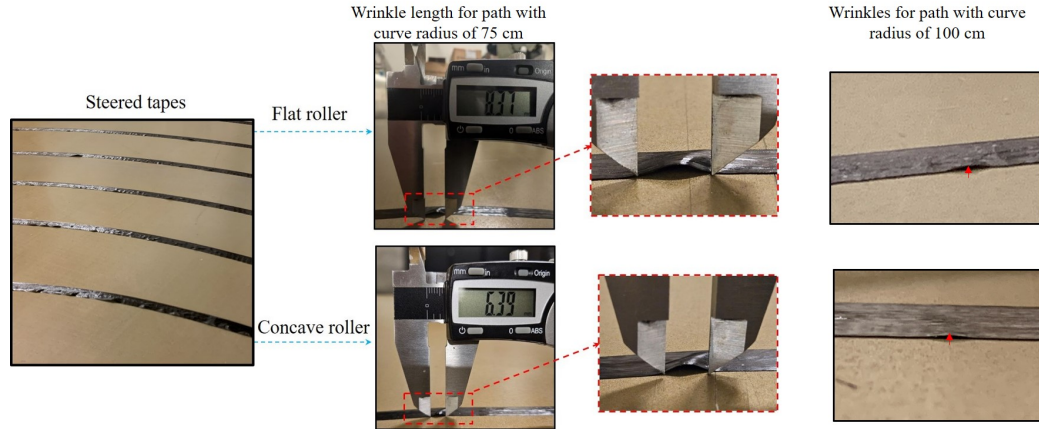


Figure 7.10: Comparison wrinkle length at steered tow placed by: (a) Concave roller and (b) standard roller.

process using the AFP robot, with the parameters specified in Table 7.3, was performed five times. In these trials, we placed the tape along four paths with varying radii: 75 cm, 90 cm, and 100 cm. Figure 7.10 displays the defects observed during AFP trials for the 75 cm and 100 cm paths, comparing the performance of concave and standard compaction rollers. The figure highlights a clear difference in the wrinkles formed in the 75 cm radius path between the concave and flat rollers, showing a 24% reduction in wrinkle length when using the concave roller. For the larger radius (100 cm), there is also a noticeable difference in wrinkle height, with the concave roller producing smaller wrinkles compared to the flat roller. Wrinkles with smaller heights can be fully eliminated during the autoclave process. These improvements in wrinkle length and height contribute to better overall part quality.

To gain a better understanding, the pressure under the roller along the curve with 75mm is recorded by a sensitive pressure film. The pressure film and the segmented images are depicted in Fig.7.11. The pressure data reveals higher pressure values near the edges, accompanied by longer contact time, which results in stronger adhesion between the prepreg

and substrate. This stronger bond leads to a reduction in defect formation.

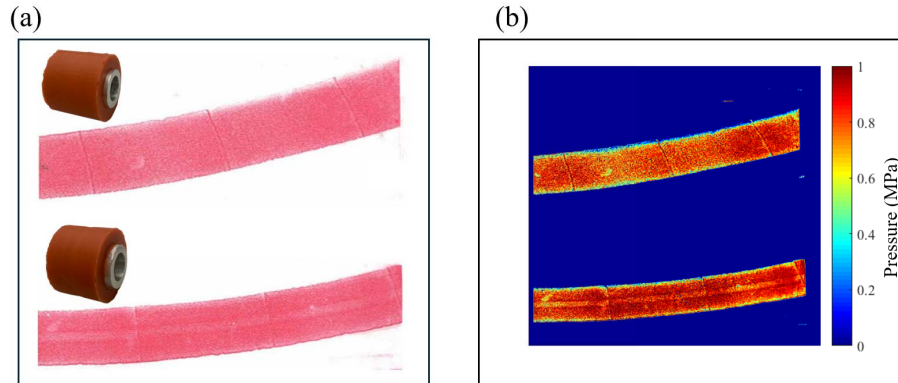


Figure 7.11: Pressure distribution under the flat and concave roller (a) sensitive-pressure film (b) segmented processed image.

## 7.6 Conclusion

This work proposes a novel approach to reduce defects in composite structures manufactured using AFP technology by altering the pressure distribution and contact length under the compaction roller based on the geometry. The effectiveness of this approach was demonstrated through a case study focusing on out-of-plane buckling, commonly referred to as wrinkle defects, in a steered tow. Wrinkle defects arise due to the mismatch in length that leads to compressive stresses along the inner edge of the steered tape. The key to reducing these defects lies in increasing the adhesion between the prepreg and the substrate, which is directly influenced by the contact time and pressure applied by the compaction roller. As detailed in the design and manufacturing procedure (Section 3), conventional compaction rollers are inadequate for increasing adhesion in critical areas. To address this limitation, we proposed a new concave roller that enhances adhesion near the edges during the lay-up process, thereby reducing wrinkle formation. Finite element modeling using Abaqus software was employed to determine values for the roller design that would achieve the desired performance presented in Equation 69. These values were then used to manufacture the roller by casting polyurethane material into a three-part PLA mold, following the dimensions obtained from the FE simulations. AFP experimental trials confirmed the

effectiveness of the newly designed roller, which successfully reduced defect length by 24%.

The findings of this research offer a promising foundation for future investigations into improving pressure distribution and contact length as a means of preventing a wider range of defects in composite manufacturing. By demonstrating the effectiveness of a geometry-based approach to compaction roller design, this study paves the way for exploring how pressure distribution and contact length can be modified to address other common defect issues.

## Chapter 8

# Conclusion and future work

This thesis presents a detailed investigation of steering-induced defects in prepreg tapes, contributing to the understanding and predictive capabilities of defect formation during the AFP process. The analytical models were presented for the prediction of two main defects during the steering, i.e. in-plane waviness and out-of-plane wrinkles. Based on the analytical and experimental works, a novel approach is proposed that focuses on altering the pressure distribution and contact length exerted by the compaction roller during the AFP process. To implement this approach, a new compaction roller has been designed and manufactured. This innovative roller efficiently adjusts the pressure distribution and contact length throughout the steering process, resulting in enhanced adhesion between the edges of the prepreg and the substrate, which consequently minimizes steering-induced defects.

Chapters 3,4 delves into the theoretical modeling of wrinkle formation during steering. In Chapter 3, the effect of initial imperfection on wrinkle formation was studied. This model employs the Koiter and the Pasternak foundation models for the description of initial imperfections and prepreg tack, respectively. This study highlighted the critical relationship between initial defects, buckling load, and steering radius, demonstrating that increased initial defects lead to reduced critical loads and radii. In Chapter 4, a general buckling model based on 3D elasticity theory was introduced to predict the out-of-plane deformation of the tape resting on a viscoelastic foundation. The model also accounts for interlaminar

imperfections in predicting the buckling load.

Chapter 5 investigates the buckling behavior of uncured thermoset prepreg through experimental and theoretical methods. The research revealed that steered prepreg can exhibit both planar and non-planar buckling. A novel micro-mechanic approach effectively models the viscoelastic behavior of the uncured matrix, leading to accurate predictions of critical buckling loads and wavelengths of non-planar wrinkles.

Chapter 6 offers a comprehensive analysis of inter-ply shear behavior in uncured prepreg through a combination of experimental and numerical investigations. The research identified optimal AFP process parameters, demonstrating how temperature, pressure, and dwell time interact to enhance inter-ply shear strength. The findings underscored the necessity of considering the interplay of multiple parameters rather than isolating individual effects, contributing valuable insights into the shear strength and bonding quality of prepreg materials.

Chapter 7 introduces a novel geometry-based method for improving adhesion and minimizing defects, especially wrinkles, in the AFP process. By strategically modifying the pressure distribution and contact length of the compaction roller, this study effectively reduced the length and height of wrinkles, resulting in enhanced final part quality.

## 8.1 Future work

The future work that remains to be done is summarized below:

The model developed in this thesis can predict wrinkle formation in steered tapes on a flat mold. A potential area for future enhancement is extending the model to account for steered tape on double-curved surfaces. This advancement would reduce trial-and-error efforts in minimizing defects during the manufacturing of such molds and improve the quality of parts with more complex geometries.

The model can be further refined by incorporating the tensile force applied by the machine during the manufacturing process, the precise position of the neutral axis, and improving the accuracy of determining prepreg tack properties. Current equipment used

for measuring tack properties does not fully replicate the actual conditions of the AFP process, leaving room for more precise characterization in future work.

The new approach presented in Chapter 7 offers a promising foundation for future investigations into the optimization of pressure distribution as a means of preventing a wider range of defects in composite manufacturing. By demonstrating the effectiveness of a geometry-based approach to compaction roller design, this study paves the way for exploring how pressure distribution and contact length can be modified to address other common defect issues.

# Appendix A

$$M = \begin{bmatrix} [0]_{3 \times 3} & [M_2]_{3 \times 3} \\ [M_3]_{3 \times 3} & [0]_{3 \times 3} \end{bmatrix}$$

$$M_2 = \begin{bmatrix} F & -\frac{\partial}{\partial x} & -\frac{\partial}{\partial y} \\ \frac{\partial}{\partial x} & \frac{1}{C_{55}} & 0 \\ \frac{\partial}{\partial y} & 0 & \frac{1}{C_{44}} \end{bmatrix}$$

$$M_3 = \begin{bmatrix} \frac{1}{C_{33}} & -(C_{13}/C_{33})\frac{\partial}{\partial x} & -(C_{13}/C_{33})\frac{\partial}{\partial y} \\ (C_{13}/C_{33})\frac{\partial}{\partial x} & F - \alpha_1\frac{\partial^2}{\partial x^2} - C_{66}\frac{\partial^2}{\partial y^2} & (\alpha_2 + C_{66})\frac{\partial^2}{\partial x\partial y} \\ (C_{23}/C_{33})\frac{\partial}{\partial y} & (\alpha_2 + C_{66})\frac{\partial^2}{\partial x\partial y} & F - C_{66}\frac{\partial^2}{\partial x^2} - \alpha_3\frac{\partial^2}{\partial y^2} \end{bmatrix}$$

where

$$F = \Omega = -(N_x \frac{\partial^2}{\partial x^2} + N_y \frac{\partial^2}{\partial y^2}), \alpha_1 = C_{11} - \frac{C_{13}^2}{C_{33}},$$

$$\alpha_2 = C_{12} - \frac{C_{13}C_{23}}{C_{33}}, \alpha_3 = C_{22} - \frac{C_{23}^2}{C_{33}}$$

# References

- Adams, D. O., & Hyer, M. W. (1996). Analysis of layer waviness in flat compression-loaded thermoplastic composite laminates.
- Adams, D. O., & Hyert, M. (1994). Effects of layer waviness on the compression fatigue performance of thermoplastic composite laminates. *International journal of fatigue*, *16*(6), 385–391.
- Alimirzaei, S., Najafabadi, M. A., & Khodaei, A. (2022). Characterization of the damage mechanism of glass/epoxy composite tubes under quasi-static axial loading using acoustic emission monitoring. *Applied Composite Materials*, *29*(5), 1911–1936.
- Ammar, M. M., & Shirinzadeh, B. (2021). The role of compaction roller in defining the layup quality and laminate porosity in robotic fiber placement. In *2021 24th international conference on mechatronics technology (icmt)* (pp. 1–6).
- Askarian, A., Permoon, M., & Shakouri, M. (2020). Vibration analysis of pipes conveying fluid resting on a fractional kelvin-voigt viscoelastic foundation with general boundary conditions. *International Journal of Mechanical Sciences*, *179*, 105702.
- Bagherizadeh, E., Kiani, Y., & Eslami, M. (2011). Mechanical buckling of functionally graded material cylindrical shells surrounded by pasternak elastic foundation. *Composite Structures*, *93*(11), 3063–3071.
- Bakhshi, N., & Hojjati, M. (2018). *An experimental and simulative study on the defects appeared during tow steering in automated fiber placement* (Vol. 113). Elsevier.
- Bakhshi, N., & Hojjati, M. (2019). Time-dependent wrinkle formation during tow steering in automated fiber placement. *Composites Part B: Engineering*, *165*, 586–593.

- Bakhshi, N., & Hojjati, M. (2020). Effect of compaction roller on layup quality and defects formation in automated fiber placement. *Journal of Reinforced Plastics and Composites*, 39(1-2), 3–20.
- Bakhtiari, M., & Kheradpisheh, M. (2020). Dynamics behavior and imperfection sensitivity of a fluid-filled multilayered fgm cylindrical structure. *International Journal of Mechanical Sciences*, 176, 105425.
- Beakou, A., Cano, M., Le Cam, J.-B., & Verney, V. (2011). Modelling slit tape buckling during automated prepreg manufacturing: A local approach. *Composite structures*, 93(10), 2628–2635.
- Belhaj, M., Dodangeh, A., & Hojjati, M. (2021). Experimental investigation of prepreg tackiness in automated fiber placement. *Composite Structures*, 262, 113602.
- Belhaj, M., & Hojjati, M. (2018). Wrinkle formation during steering in automated fiber placement: Modeling and experimental verification. *Journal of Reinforced Plastics and Composites*, 37(6), 396–409.
- Böckl, B., Wedel, A., Misik, A., & Drechsler, K. (2022). Effects of defects in automated fiber placement laminates and its correlation to automated optical inspection results. *Journal of Reinforced Plastics and Composites*, 07316844221093273.
- Böckl, B., Wedel, A., Misik, A., & Drechsler, K. (2023). Effects of defects in automated fiber placement laminates and its correlation to automated optical inspection results. *Journal of Reinforced Plastics and Composites*, 42(1-2), 3–16.
- Brasington, A., Sacco, C., Halbritter, J., Wehbe, R., & Harik, R. (2021). Automated fiber placement: A review of history, current technologies, and future paths forward. *Composites Part C: Open Access*, 6, 100182.
- Brinson, H. F., Brinson, L. C., et al. (2008). Polymer engineering science and viscoelasticity. *An introduction*, 99–157.
- Budelmann, D., Detampel, H., Schmidt, C., & Meiners, D. (2019). Interaction of process parameters and material properties with regard to prepreg tack in automated lay-up and draping processes. *Composites Part A: Applied Science and Manufacturing*, 117, 308–316.

- Budelmann, D., Schmidt, C., & Meiners, D. (2020). Prepreg tack: A review of mechanisms, measurement, and manufacturing implication. *Polymer composites*, *41*(9), 3440–3458.
- Budelmann, D., Schmidt, C., & Meiners, D. (2021). Adhesion-cohesion balance of prepreg tack in thermoset automated fiber placement. part 1: Adhesion and surface wetting. *Composites Part C: Open Access*, *6*, 100204.
- Campilho, R. D., Banea, M., Neto, J., & Da Silva, L. (2012). Modelling of single-lap joints using cohesive zone models: effect of the cohesive parameters on the output of the simulations. *The Journal of Adhesion*, *88*(4-6), 513–533.
- Chen, W., Cai, J., & Ye, G. (2003). Exact solutions of cross-ply laminates with bonding imperfections. *AIAA journal*, *41*(11), 2244–2250.
- Chen, W., Lee, K. Y., & Ding, H. (2005). On free vibration of non-homogeneous transversely isotropic magneto-electro-elastic plates. *Journal of Sound and Vibration*, *279*(1-2), 237–251.
- Cheng, Z.-q., Kennedy, D., & Williams, W. (1996). Effect of interfacial imperfection on buckling and bending behavior of composite laminates. *AIAA journal*, *34*(12), 2590–2595.
- Croft, K., Lessard, L., Pasini, D., Hojjati, M., Chen, J., & Yousefpour, A. (2011). Experimental study of the effect of automated fiber placement induced defects on performance of composite laminates. *Composites Part A: Applied Science and Manufacturing*, *42*(5), 484–491.
- Crossley, R., Schubel, P., & Warrior, N. (2012). The experimental determination of prepreg tack and dynamic stiffness. *Composites Part A: Applied Science and Manufacturing*, *43*(3), 423–434.
- Crossley, R. J., Schubel, P. J., & De Focatiis, D. S. (2013). Time–temperature equivalence in the tack and dynamic stiffness of polymer prepreg and its application to automated composites manufacturing. *Composites Part A: Applied science and manufacturing*, *52*, 126–133.

- Das, A., Choong, G. Y., Dillard, D. A., De Focatiis, D. S., & Bortner, M. J. (2022). Characterizing friction for fiber reinforced composites manufacturing: Method development and effect of process parameters. *Composites Part B: Engineering*, *236*, 109777.
- Dillard, D. A., Mukherjee, B., Karnal, P., Batra, R. C., & Frechette, J. (2018). A review of winkler's foundation and its profound influence on adhesion and soft matter applications. *Soft matter*, *14*(19), 3669–3683.
- Ding, H., Chen, W., & Zhang, L. (2006). *Elasticity of transversely isotropic materials* (Vol. 126). Springer Science & Business Media.
- Dirk, H.-J. L., Ward, C., & Potter, K. D. (2012). The engineering aspects of automated prepreg layup: History, present and future. *Composites Part B: Engineering*, *43*(3), 997–1009.
- Dubois, O., Le Cam, J.-B., & Beakou, A. (2010). Experimental analysis of prepreg tack. *Experimental Mechanics*, *50*(5), 599–606.
- Endruweit, A., Choong, G. Y., Ghose, S., Johnson, B. A., Younkin, D. R., Warrior, N. A., & De Focatiis, D. S. (2018). Characterisation of tack for uni-directional prepreg tape employing a continuous application-and-peel test method. *Composites Part A: Applied Science and Manufacturing*, *114*, 295–306.
- Erland, S., Dodwell, T., & Butler, R. (2015). Characterisation of inter-ply shear in uncured carbon fibre prepreg. *Composites Part A: Applied Science and Manufacturing*, *77*, 210–218.
- Esen, I. (2019). Dynamic response of a functionally graded timoshenko beam on two-parameter elastic foundations due to a variable velocity moving mass. *International journal of mechanical sciences*, *153*, 21–35.
- Etchegaray Bello, M., Engelhardt, R., Bublitz, D., & Drechsler, K. (2022). Lab-scale experimental analysis of the cyclic compaction-recovery characteristics of uncured thermoset prepreg. *Advanced Manufacturing: Polymer & Composites Science*, *8*(2), 56–67.
- Fereidouni, M., & Hoa, S. V. (2024). In-situ consolidation of thermoplastic composites by automated fiber placement: Characterization of defects. *Journal of Thermoplastic*

*Composite Materials*, 08927057241251837.

- Fischer, B., Horn, B., Bartelt, C., & Blößl, Y. (2015). Method for an automated optimization of fiber patch placement layout designs. *Int J Compos Mater*, 5(2), 37–46.
- Grunenfelder, L. K., & Nutt, S. R. (2012). Prepreg age monitoring via differential scanning calorimetry. *Journal of Reinforced Plastics and Composites*, 31(5), 295–302.
- Hadji, L., Avcar, M., & Zouatnia, N. (2022). Natural frequency analysis of imperfect fg sandwich plates resting on winkler-pasternak foundation. *Materials Today: Proceedings*, 53, 153–160.
- Hajikarimi, P., & Nejad, F. M. (2021). *Applications of viscoelasticity: Bituminous materials characterization and modeling*. Elsevier.
- Han, Q., Cheng, Y., Lu, Y., Li, T., & Lu, P. (2016). Nonlinear buckling analysis of shallow arches with elastic horizontal supports. *Thin-Walled Structures*, 109, 88–102.
- Harik, R., & Wuest, T. (2019). *Introduction to advanced manufacturing*. SAE International.
- He, Y., Jiang, J., Qu, W., & Ke, Y. (2022). Compaction pressure distribution and pressure uniformity of segmented rollers for automated fiber placement. *Journal of Reinforced Plastics and Composites*, 41(11-12), 427–443.
- Hebali, H., Chikh, A., Bousahla, A. A., Bourada, F., Tounsi, A., Benrahou, K. H., . . . Tounsi, A. (2022). Effect of the variable visco-pasternak foundations on the bending and dynamic behaviors of fg plates using integral hsd model. *Arch. Appl. Mech*, 83(2), 177–191.
- Heinecke, F., & Willberg, C. (2019). Manufacturing-induced imperfections in composite parts manufactured via automated fiber placement. *Journal of Composites Science*, 3(2), 56.
- Heller, K. (2022). *Influence of material property changes on thermoset automated fiber placement processing* (Unpublished doctoral dissertation). Technische Universität München.
- Heller, K., Böckl, B., Ebel, C., & Drechsler, K. (2018). Influence of prepreg aging and tack on lay-up effects/defects in thermoset automated fiber placement. In *18th european conference on composite materials, athens, greece*.

- Hörmann, P. M. (2015). *Thermoset automated fibre placement—on steering effects and their prediction* (Unpublished doctoral dissertation). Technische Universität München.
- Hu, H., Cao, D., Cao, Z., & Li, S. (2021). Experimental and numerical investigations of wrinkle effect on failure behavior of curved composite laminates. *Composite Structures*, *261*, 113541.
- Hu, Y., Han, G., Cheng, F., & Hu, X. (2023). Thickness effect on flexural strengths of laminar carbon fibre composites. *Thin-Walled Structures*, *186*, 110690.
- Huang, Z., Lü, C., & Chen, W. (2008). Benchmark solutions for functionally graded thick plates resting on winker–pasternak elastic foundations. *Composite Structures*, *85*(2), 95–104.
- Hyer, M. W., & White, S. R. (2009). *Stress analysis of fiber-reinforced composite materials*. DEStech Publications, Inc.
- Ji, K., Wei, C., Deng, W., Zhang, Y., Liu, Y., Mao, R., & Wang, X. (2002). Evaluation of glass fibre/epoxy prepreg quality during storage. *Polymers and Polymer Composites*, *10*(8), 599–606.
- Jiang, J., He, Y., & Ke, Y. (2019). Pressure distribution for automated fiber placement and design optimization of compaction rollers. *Journal of Reinforced Plastics and Composites*, *38*(18), 860–870.
- Jiang, J., He, Y., Wang, H., & Ke, Y. (2021). Modeling and experimental validation of compaction pressure distribution for automated fiber placement. *Composite Structures*, *256*, 113101.
- Jing, Z., & Duan, L. (2022). A three-dimensional sampling optimization method for buckling optimization of variable prestressed composite plates. *Thin-Walled Structures*, *181*, 110096.
- Juhász, Z., & Szekrényes, A. (2020). An analytical solution for buckling and vibration of delaminated composite spherical shells. *Thin-Walled Structures*, *148*, 106563.
- Kerr, A. D. (1964). Elastic and viscoelastic foundation models. *J. Appl. Mech.*
- Kerr, A. D. (1965). A study of a new foundation model. *Acta Mechanica*, *1*(2), 135–147.
- Kheradpisheh, M., & Hojjati, M. (2021). Wrinkle formation and initial defect sensitivity

- of steered tow in automated fiber placement. *Journal of Composites Science*, 5(11), 295.
- Kheradpisheh, M., & Hojjati, M. (2023). In-plane and out-of-plane deformations in automated fiber placement employing micromechanics method. *Composites Part A: Applied Science and Manufacturing*, 170, 107543.
- Kiani, Y., Bagherizadeh, E., & Eslami, M. (2012). Thermal and mechanical buckling of sandwich plates with fgm face sheets resting on the pasternak elastic foundation. *Proceedings of the Institution of Mechanical Engineers, Part C: Journal of Mechanical Engineering Science*, 226(1), 32–41.
- Kiasat, M., Zamani, H., & Aghdam, M. (2014). On the transient response of viscoelastic beams and plates on viscoelastic medium. *International Journal of Mechanical Sciences*, 83, 133–145.
- Kim, G. W., & Lee, K. Y. (2008). Influence of weak interfaces on buckling of orthotropic piezoelectric rectangular laminates. *Composite Structures*, 82(2), 290–294.
- Lan, M., Cartié, D., Davies, P., & Baley, C. (2015). Microstructure and tensile properties of carbon–epoxy laminates produced by automated fibre placement: Influence of a caul plate on the effects of gap and overlap embedded defects. *Composites Part A: Applied Science and Manufacturing*, 78, 124–134.
- Lan, M., Cartié, D., Davies, P., & Baley, C. (2016). Influence of embedded gap and overlap fiber placement defects on the microstructure and shear and compression properties of carbon–epoxy laminates. *Composites Part A: Applied Science and Manufacturing*, 82, 198–207.
- Le, V. A., Zobeiry, N., Erkmén, E., & Malek, S. (2021). Buckling behaviour of laminated viscoelastic composites under axial loads. *Mechanics of Materials*, 159, 103897.
- Li, S., Thouless, M., Waas, A., Schroeder, J., & Zavattieri, P. (2005). Use of mode-I cohesive-zone models to describe the fracture of an adhesively-bonded polymer-matrix composite. *Composites Science and Technology*, 65(2), 281–293.
- Lightfoot, J. S., Wisnom, M. R., & Potter, K. (2013). A new mechanism for the formation of ply wrinkles due to shear between plies. *Composites Part A: Applied Science and*

- Manufacturing*, 49, 139–147.
- Liu, B., Gao, N., Tang, B., Gao, Y., Jin, P., Lu, Z., & Fu, Z. (2020). Progressive damage behaviors of the stepped-lap composite joints under bending load. *Journal of Composite Materials*, 54(14), 1875–1887.
- Liu, D., Kitipornchai, S., Chen, W., & Yang, J. (2018). Three-dimensional buckling and free vibration analyses of initially stressed functionally graded graphene reinforced composite cylindrical shell. *Composite Structures*, 189, 560–569.
- Lopatin, A., & Morozov, E. (2009). Buckling of the ssff rectangular orthotropic plate under in-plane pure bending. *Composite structures*, 90(3), 287–294.
- Lü, C., Lim, C. W., & Chen, W. (2009). Exact solutions for free vibrations of functionally graded thick plates on elastic foundations. *Mechanics of Advanced Materials and Structures*, 16(8), 576–584.
- Lu, S., Evans, A., & Turner, T. (2023). Analysis of roller compaction pressure distribution in automated dry fibre placement. *Composite Structures*, 316, 117048.
- Ma, H., Bandaru, A. K., & Weaver, P. M. (2024). The effect of laser assisted tape placement processing conditions on microstructural evolution, residual stress and interlaminar shear strength of carbon fibre/peek laminates. *Composites Part B: Engineering*, 274, 111293.
- Ma, X., Butterworth, J., & Clifton, C. (2007). Compressive buckling analysis of plates in unilateral contact. *International journal of solids and structures*, 44(9), 2852–2862.
- Machado, M., Fischlschweiger, M., & Major, Z. (2015). Strength of single-lap-joint assemblies of continuous unidirectional carbon fibre-reinforced thermoplastic matrix tapes under tensile loading. *Journal of Composite Materials*, 49(16), 1977–1987.
- MAHAPATRA, S. (2023). Computationally efficient process modelling of automated fibre placement.
- Matveev, M. Y., Schubel, P. J., Long, A. C., & Jones, I. (2016). Understanding the buckling behaviour of steered tows in automated dry fibre placement (adfp). *Composites Part A: Applied Science and Manufacturing*, 90, 451–456.
- Mirzavand, B., & Eslami, M. (2006). Thermal buckling of imperfect functionally graded

- cylindrical shells based on the wan–donnell model. *Journal of Thermal Stresses*, 29(1), 37–55.
- Mizukami, K., Mizutani, Y., Todoroki, A., & Suzuki, Y. (2016). Detection of in-plane and out-of-plane fiber waviness in unidirectional carbon fiber reinforced composites using eddy current testing. *Composites Part B: Engineering*, 86, 84–94.
- Mohan, R. P., Alshahrani, H., & Hojjati, M. (2016). Investigation of intra-ply shear behavior of out-of-autoclave carbon/epoxy prepreg. *Journal of Composite Materials*, 50(30), 4251–4268.
- Mossavarali, A., Saheli, G. P., & Eslami, M. (2000). Thermoelastic buckling of isotropic and orthotropic plates with imperfections. *Journal of thermal stresses*, 23(9), 853–872.
- Mukhopadhyay, S., Jones, M. I., & Hallett, S. R. (2015a). Compressive failure of laminates containing an embedded wrinkle; experimental and numerical study. *Composites Part A: Applied Science and Manufacturing*, 73, 132–142.
- Mukhopadhyay, S., Jones, M. I., & Hallett, S. R. (2015b). Tensile failure of laminates containing an embedded wrinkle; numerical and experimental study. *Composites Part A: Applied Science and Manufacturing*, 77, 219–228.
- Muscolino, G., & Palmeri, A. (2007). Response of beams resting on viscoelastically damped foundation to moving oscillators. *International Journal of Solids and structures*, 44(5), 1317–1336.
- NAM, . (2021). *National association of manufacturers, facts about manufacturing*. Retrieved from <https://www.nam.org/facts-about-manufacturing/>
- Nazarimofrad, E., & Barkhordar, A. (2016). Buckling analysis of orthotropic rectangular plate resting on pasternak elastic foundation under biaxial in-plane loading. *Mechanics of Advanced Materials and Structures*, 23(10), 1144–1148.
- Nguyen, P. L., Vu, X. H., & Ferrier, E. (2019). Thermo-mechanical performance of carbon fiber reinforced polymer (cfrp), with and without fire protection material, under combined elevated temperature and mechanical loading conditions. *Composites Part B: Engineering*, 169, 164–173.

- Oromiehie, E., Prusty, B. G., Compston, P., & Rajan, G. (2019). Automated fibre placement based composite structures: Review on the defects, impacts and inspections techniques. *Composite Structures*, *224*, 110987.
- Pan, H., Yang, D., Qu, W., Li, J., & Ke, Y. (2022). Process-dependent wrinkle formation for steered tow during automated fiber placement: Modeling and experimental verification. *Thin-Walled Structures*, *180*, 109928.
- Pandey, R., & Sun, C. (1999). Mechanisms of wrinkle formation during the processing of composite laminates. *Composites science and technology*, *59*(3), 405–417.
- Peters, S. T. (2013). *Handbook of composites*. Springer Science & Business Media.
- Poursartip, A., Bakhshi, N., Tong, O., Chen, Z., Sarwar, M. S., & Madden, J. (2021). *Science-based automation of composites manufacturing* (Tech. Rep.). UNIVERSITY OF BRITISH COLUMBIA.
- Rafiee, R., & Sotoudeh, S. (2021). A cohesive zone model for predicting the initiation of mode ii delamination in composites under cyclic loading. *Journal of Reinforced Plastics and Composites*, *40*(5-6), 179–192.
- Rajan, S., Sutton, M. A., Sockalingam, S., McMakin, W., Gurdal, Z., & Kidane, A. (2020). Simulations and experiments for automated fiber placement of prepreg slit tape: Wrinkle formation and fundamental observations. *Composites Part B: Engineering*, *201*, 108287.
- Rajan, S., Sutton, M. A., Wehbe, R., Tatting, B., Gürdal, Z., Kidane, A., & Harik, R. (2019). Experimental investigation of prepreg slit tape wrinkling during automated fiber placement process using stereodic. *Composites Part B: Engineering*, *160*, 546–557.
- Rajasekaran, A., & Shadmehri, F. (2022). Steering of carbon fiber/peek tapes using hot gas torch-assisted automated fiber placement. *Journal of Thermoplastic Composite Materials*, 08927057211067962.
- Rashidi, A., Montazerian, H., Yesilcimen, K., & Milani, A. (2020). Experimental characterization of the inter-ply shear behavior of dry and prepreg woven fabrics: Significance of mixed lubrication mode during thermoset composites processing. *Composites Part*

- A: Applied Science and Manufacturing*, 129, 105725.
- Reddy, J., & Khdeir, A. (1989). Buckling and vibration of laminated composite plates using various plate theories. *AIAA journal*, 27(12), 1808–1817.
- Reddy, J. N. (2003). *Mechanics of laminated composite plates and shells: theory and analysis*. CRC press.
- Rousseau, G., Wehbe, R., Halbritter, J., & Harik, R. (2019). Automated fiber placement path planning: A state-of-the-art review. *Computer-Aided Design and Applications*, 16(2), 172–203.
- s. (1973). *Buckling of elastic fibers in a composite plate wehbe2020geometricalwith viscoelastic matrix*. The Ohio State University.
- Samsam Shariat, B., & Eslami, M. (2005). Effect of initial imperfections on thermal buckling of functionally graded plates. *Journal of thermal stresses*, 28(12), 1183–1198.
- Sayyad, A. S., & Ghugal, Y. M. (2017). Bending, buckling and free vibration of laminated composite and sandwich beams: A critical review of literature. *Composite Structures*, 171, 486–504.
- Shariat, B. S., Javaheri, R., & Eslami, M. (2005). Buckling of imperfect functionally graded plates under in-plane compressive loading. *Thin-walled structures*, 43(7), 1020–1036.
- Shen, H.-S., Xiang, Y., & Lin, F. (2017). Thermal buckling and postbuckling of functionally graded graphene-reinforced composite laminated plates resting on elastic foundations. *Thin-Walled Structures*, 118, 229–237.
- Smith, A., Endruweit, A., Choong, G., De Focatiis, D., & Hubert, P. (2020). Adaptation of material deposition parameters to account for out-time effects on prepreg tack. *Composites Part A: Applied Science and Manufacturing*, 133, 105835.
- Smith, A. W., & Hubert, P. (2023). Benchmarking of potential rapid inspection methods for quantitative tracking of thermoset prepreg state evolution with prolonged ambient ageing. *Composites Part B: Engineering*, 254, 110579.
- Su, T., Liu, J., Terwagne, D., Reis, P. M., & Bertoldi, K. (2014). Buckling of an elastic rod embedded on an elastomeric matrix: planar vs. non-planar configurations. *Soft Matter*, 10(33), 6294–6302.

- Tang, Y., Wang, W., Wang, H., Li, J., & Ke, Y. (2022). Influences of wrinkles induced by tows' offset in automated fiber placement on the bending properties of composites. *Composite Structures*, *297*, 115964.
- Thai, H.-T., & Choi, D.-H. (2011). A refined plate theory for functionally graded plates resting on elastic foundation. *Composites Science and Technology*, *71*(16), 1850–1858.
- Timoshenko, S. (1970). *Theory of elastic stability 2e*. Tata McGraw-Hill Education.
- Venkatesan, C., Zulkifli, F., & Silva, A. (2023). Effects of processing parameters of infrared-based automated fiber placement on mechanical performance of carbon fiber-reinforced thermoplastic composite. *Composite Structures*, *309*, 116725.
- Vogl, S., Knott, R., Sommacal, S., Compston, P., & Drechsler, K. (2024). Influence of compaction and curing in the automated fiber placement process on the mechanical performance of composite laminates. *Composite Structures*, *330*, 117826.
- Wang, X., Chen, C., Hu, S., Chen, Z., Jiang, W., Shen, G., . . . Zhou, H. (2024). In-situ infrared annealing for laser-assisted automated fiber placement to enhance interlaminar properties without sacrificing laydown efficiency. *Composites Part A: Applied Science and Manufacturing*, *183*, 108214.
- Wang, Y., Belnoue, J. P.-H., Ivanov, D. S., & Hallett, S. R. (2021). Hypo-viscoelastic modelling of in-plane shear in ud thermoset prepregs. *Composites Part A: Applied Science and Manufacturing*, *146*, 106400.
- Wang, Y., Chea, M. K., Belnoue, J. P.-H., Kratz, J., Ivanov, D. S., & Hallett, S. R. (2020). Experimental characterisation of the in-plane shear behaviour of ud thermoset prepregs under processing conditions. *Composites Part A: Applied Science and Manufacturing*, *133*, 105865.
- Wehbe, R., Sacco, C., Radwan, A. B., Albazzan, M., & Harik, R. (2020). Influence of process parameters in afp fiber steering on cylinders: Constant curvature paths. *Composites Part C: Open Access*, *2*, 100036.
- Wehbe, R., Tatting, B., Rajan, S., Harik, R., Sutton, M., & Gürdal, Z. (2020). Geometrical modeling of tow wrinkles in automated fiber placement. *Composite Structures*, *246*, 112394.

- Wehbe, R. Y., Harik, R., & Gurdal, Z. (2019). In-plane tow deformations due to steering in automated fiber placement. In *Aiaa scitech 2019 forum* (p. 1271).
- Wohl, C., Palmieri, F. L., Forghani, A., Hickmott, C., Bedayat, H., Coxon, B., . . . Grimsley, B. (2017). *Tack measurements of prepreg tape at variable temperature and humidity* (Tech. Rep.).
- Woigk, W., Hallett, S. R., Jones, M. I., Kultz, M., Hornig, A., & Gude, M. (2018). Experimental investigation of the effect of defects in automated fibre placement produced composite laminates. *Composite Structures*, *201*, 1004–1017.
- Ying, J., Lü, C., & Chen, W. (2008). Two-dimensional elasticity solutions for functionally graded beams resting on elastic foundations. *Composite Structures*, *84*(3), 209–219.
- Younesian, D., Hosseinkhani, A., Askari, H., & Esmailzadeh, E. (2019). Elastic and viscoelastic foundations: a review on linear and nonlinear vibration modeling and applications. *Nonlinear Dynamics*, *97*(1), 853–895.
- Zacherl, L., Fontes, A., & Shadmehri, F. (2024). Three-dimensional heat transfer analysis of hot gas torch (hgt)-assisted automated fiber placement (afp) for thermoplastic composites. *Composite Structures*, 118256.
- Zaitoun, M. W., Chikh, A., Tounsi, A., Al-Osta, M. A., Sharif, A., Al-Dulaijan, S. U., & Al-Zahrani, M. M. (2022). Influence of the visco-pasternak foundation parameters on the buckling behavior of a sandwich functional graded ceramic–metal plate in a hygrothermal environment. *Thin-Walled Structures*, *170*, 108549.
- Zenker, T., Bruckner, F., & Drechsler, K. (2019). Effects of defects on laminate quality and mechanical performance in thermoplastic automated fiber placement-based process chains. *Advanced Manufacturing: Polymer & Composites Science*, *5*(4), 184–205.
- Zenkour, A. M., & Alghanmi, R. A. (2022). A refined quasi-3d theory for the bending of functionally graded porous sandwich plates resting on elastic foundations. *Thin-Walled Structures*, *181*, 110047.
- Zenkour, A. M., & El-Shahrany, H. D. (2021). Hygrothermal forced vibration of a viscoelastic laminated plate with magnetostrictive actuators resting on viscoelastic foundations. *International Journal of Mechanics and Materials in Design*, *17*(2), 301–320.